CHALMERS

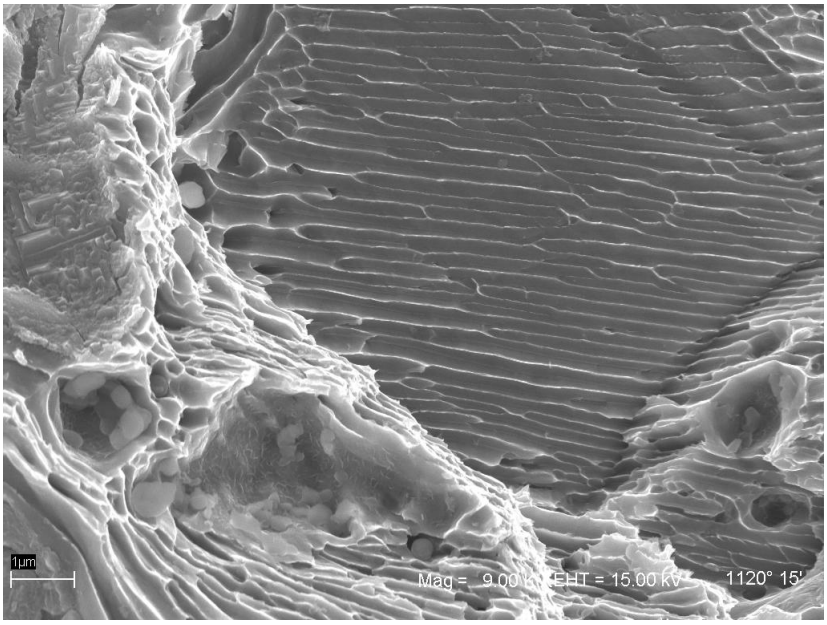

Inter-particle connections development during sintering of Cr-Mo-alloyed steel powder in N_2/H_2 atmosphere

MARÍA IRENE DE DIEGO CALDERÓN

Department of Materials and Manufacturing Technology
CHALMERS UNIVERSITY OF TECHNOLOGY
Gothenburg, Sweden, 2009
Master Thesis No.143/2009

Inter-particle connections development during sintering of Cr-Mo-alloyed steel powder in N_2/H_2 atmosphere

by

María Irene de Diego Calderón

Department of Materials and Manufacturing Technology
CHALMERS UNIVERSITY OF TECHNOLOGY
Göteborg, Sweden 2009

Master Thesis in Advanced Engineering Materials No.143/2009

Examensarbete No. 143/2009
Institutionen för material- och tillverkningsteknik
Chalmers Tekniska Högskola
Göteborg
ISSN 1652-8913

Performed at: Department of Materials and Manufacturing Technology
Chalmers University of Technology
SE-41296 Göteborg

Examiner: Professor Lars Nyborg
Department of Materials and Manufacturing Technology
Chalmers University of Technology
SE-41296 Göteborg

Supervisor: PhD Student, Dimitris Chasoglou
Department of Materials and Manufacturing Technology
Chalmers University of Technology
SE-41296 Göteborg

INTRODUCCIÓN

La pulvimetalurgia es una de las técnicas de procesamiento de materiales metálicos más antiguas: consiste en un proceso de fabricación para la producción de componentes metálicos, cerámicos o de materiales compuestos a partir de polvos. La fabricación de piezas fabricadas a partir de polvos férreos se ha incrementado en las últimas décadas, en especial en la fabricación de elementos para la industria del automóvil.

Las propiedades de un componente fabricado por PM pueden ser ajustadas o mejoradas mediante la adición de elementos de aleación: cromo y molibdeno han sido ampliamente utilizados en la metalurgia convencional como aleantes, pero la tendencia del cromo para formar óxidos de cromo muy estables y el decremento en compresibilidad que produce han limitado su uso en pulvimetalurgia. Sin embargo, los aceros aleados con bajo contenido en cromo cumplen todos los requerimientos necesarios para la mayoría de los componentes estructurales y para las necesidades del mercado, por lo que investigación y desarrollo de este tipo de aceros se está desarrollando en estos últimos años.

En este estudio, probetas de la misma composición (polvos pre-aleados fabricados mediante atomización en agua con bajo contenido en cromo y molibdeno) fueron sinterizadas en atmósfera de $90N_2/10H_2$ durante tres minutos y a diferentes temperaturas desde 700 hasta 1120ºC. Asimismo, dos probetas adicionales se sinterizaron a 1120ºC durante 15 y 30 minutos respectivamente. Las probetas fueron sometidas a ensayo de fractura para producir superficies de fractura, que fueron estudiadas mediante microscopía electrónica de barrido (SEM) y microscopía óptica.

El objetivo de esta investigación fue evaluar el efecto de la temperatura y tiempo de sinterización en la evolución de los cuellos entre partículas y de las inclusiones.

Se ha encontrado que el desarrollo de los cuellos entre partículas se ve incrementado con un aumento en la temperatura y el tiempo de sinterización y que la reducción de la capa superficial de óxido de hierro en las partículas es condición necesaria para la formación de contactos sólidos entre partículas. Además, se han encontrado diferentes mecanismos de fallo al aumentar la temperatura de sinterización. También ha podido comprobarse como la morfología y tamaño de las inclusiones cambia al aumentar la temperatura de sinterización y el tiempo, lo que puede suponer el punto de partida para investigaciones futuras.

Este proyecto ha sido realizado en el departamento de Materiales y Tecnología de Fabricación en Chalmers University of Technology (Göteborg, Suecia) entre los meses de Octubre de 2008 y Febrero de 2009 bajo la supervisión del Estudiante de Doctorado Dimitris Chasoglu. El examinador del proyecto en Chalmers University of Technology ha sido el Profesor Lars Nyborg y el tutor en la Universidad Carlos III el Catedrático del departamento de Ciencia de los Materiales e Ingeniería Metalúrgica, José Manuel Torralba.

El proyecto fue presentado en Chalmers University of Technology el 24 de Febrero de 2009, obteniendo la máxima calificación disponible de acuerdo al sistema de calificación sueco (grade 5) y al sistema de calificación ECTS (grade A).

María Irene de Diego Calderón

Göteborg, 28 de Febrero de 2009

ABSTRACT

Powder metallurgy is one of the oldest metal processing techniques; it is a manufacturing process that is based on the production of metal, ceramic or composite components from powders. Manufacturing of ferrous powder metallurgy precision parts has increased in the last decades, in particular for automotive applications.

The properties of a component manufacture by PM techniques may be tailored or improved by the addition of alloying elements; chromium and molybdenum are widely used in conventional metallurgy as alloying elements, but the tendency of chromium to form stable oxides and the decrease in compressibility it produces, have restricted its use in powder metallurgy. However, low chromium alloyed steels meet all the requirements for most structural components and for the market needs, so research and development of these steels is being carried out nowadays.

In this study, specimens of the same composition (pre-alloyed water atomized powder of low Cr-Mo content) were sintered in a $90N_2/10H_2$ atmosphere during 3 minutes and at different temperatures from 700°C to 1120°C. Two additional samples were sintered at 1120°C during 15 and 30 minutes each. Impact test was performed in all the specimens in order to produce fracture surfaces, which were studied using High Resolution Scanning Electron Microscopy (HRSEM) and EDX analysis. Microstructural investigation was carried out as well.

The objective of this investigation was to evaluate the effect of the sintering temperature and time on both the inter-particle necks development and the inclusions evolution.

It was found that Inter-particle necks development is enhanced with sintering temperature and time and that the reduction of the Fe-oxide layer on the powder particles is a pre-condition for the formation of solid metallic contacts. Furthermore, different failure mechanisms were found with increasing sintering temperature.

It was also found that the morphology and size of the inclusions change with increasing sintering temperature and time.

INDEX

1. THEORETICAL BACKGROUND 3
Powder Metallurgy 3
1.1.1. Powder Metallurgy history 3
1.1.2. Powder Metallurgy method 3
Powder Production 4
1.2.1 Atomization techniques 4
1.2.2 Commercial production methods for metal powders 6
1.2.3 Steel powders 6
Shaping and Compaction 7
1.3.1 Compaction 7
Sintering 8
1.4.1 Solid state sintering basics 8
1.4.2. Stages 10
1.4.3 Protective Atmospheres 12
1.4.4. Reactions occurring during sintering process 13
1.4.5. Oxides stability and removal in Cr-Mo-prealloyed steels 13
1.4.6.Thermodynamics calculations 15
1.4.7. Furnaces 18
Materials 19
2. EXPERIMENTAL PROCEDURE 23
3. RESULTS 25
A700-3 27
A800-3 30
A900-3 34
A1000-3 39
A1120-3 43
A1120- 15 47
A1120- 30 51
4. DISCUSSION 57
5. CONCLUSIONS 61
6. REFERENCES 63
7. ACKNOWLEDGEMENTS 65
Appendix I 67
A700-3 68
A800-3 69

A900-3 70
1000-3 71
A1120-3 72
A1120-15 73
A1120-30 74
Appendix II 75
A700-3 76
A800-3 77
A900-3 78
A1000-3 79
A1120-3 80
A1120-15 81
A1120-30 82

PREFACE

In this study, specimens of the same composition (pre-alloyed water atomized powder of low Cr-Mo content) were sintered in a $90N_2/10H_2$ atmosphere during 3 minutes and at different temperatures from 700°C to 1120°C. Two additional samples were sintered at 1120°C during 15 and 30 minutes each. Simple impact test was performed in all the specimens in order to produce fracture surfaces, which were studied using High Resolution Scanning Electron Microscopy (HRSEM) and EDX manalysis. Microstructural analysis was carried out as well.

The objective of this investigation was to evaluate the effect of the sintering temperature and time on both the inter-particle necks development and the inclusions evolution.

The examiner of this project was Professor Lars Nyborg, and it was performed under the supervision of PhD student Dimitris Chasoglou in the Department of Materials and Manufacturing Technology at Chalmers University of Thecnology from October 2009 to February 2009.

Göteborg, February 2009-02-28

María Irene de Diego Calderón

1. THEORETICAL BACKGROUND

1.1 Powder Metallurgy

Powder metallurgy is a manufacturing process that is based on the production of metal, ceramic or composite components from powders. It combines the features of shape making technology of final material and design properties during consolidation processes [2].

Some of the advantages of PM are:

- Efficient use of the base material and energy saving, which means cost efficiency
- Components with complex geometry can be manufactured
- Potential alloys that are different to produce by other methods can be produced

Nowadays, PM is used in applications where the cost of the product is the lowest compared with any other method, where the final product provides best properties comparing with any other technique or when it is the only possible technology that can be used.

1.1.1. Powder Metallurgy history

Powder metallurgy is one of the oldest metal processing techniques; about 3000 B.C, Egyptians used a “sponge iron” for making tools. Another important example where powder metallurgy was used in ancient history is Delhi Pillar (300 A.C.) [2].

After that, sintering of metals was entirely forgotten during the succeeding centuries. It was revived in Europe at the end of the 18th century, when various methods of platinum powder production were recorded [2, 5].

In the 1930´s the automotive industry developed the first commercial products, such as the oil pump by General Motors. Since that, this technique has evolved from simple shapes and materials mixes to more complex products [2, 5].

1.1.2. Powder Metallurgy method

The traditional Powder Metallurgy process follows the steps outlined are sketched in fig. 1. The powder particles are manufactured by a powder production method (e.g. water atomization); the powder ingredients components are selected in order to fulfill the process constraints and still meet the requirements of the final product. Then, the component powders are mixed, together with additives such as lubricants and graphite. During the mixing step, the selected powder particles and the additives are homogeneously mixed [2, 22].

Once the mix is ready, the blend is loaded into a die and compacted under pressure; the resulting product is called “green compact”. This green compact is sintered in a controlled atmosphere furnace. Optional manufacturing or finishing steps may be done after the sintering stage to obtain the final product [2, 22].

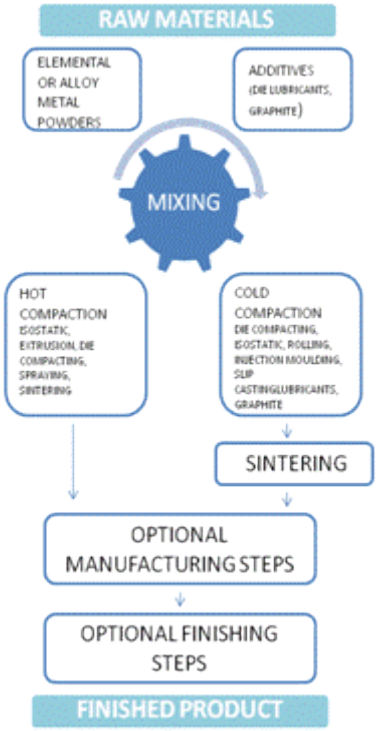

FIGURE1.TRADITIONAL POWDER METALLURGY STEPS (PLOTTED FROM [22])

1.2 Powder production

Knowing how a powder is made provides a good basis for estimating and understanding some of its characteristics. Almost all materials can be made into powders, but the method selected for fabricating powders depends on specific materials properties. The four main categories of fabrication techniques can be listed as follows [1]:

- Mechanical techniques
- Chemical reactions
- Electrolytic decomposition
- Liquid metal atomization

The formation of a powder involves the delivery of energy to the material to create new surface area. Important characteristics are the process efficiency, energy content, type of feedstock, and possible sources of contamination. The selection of one fabrication method over another depends on understanding the process, its economics, the resulting powder characteristics, and how those characteristics match with the intended application [1].

1.2.1 Atomization techniques

In recent years PM has turned to several advanced powder fabrication which fall under the general heading of atomization. Prior to the development of atomization, powder chemistry and shape characteristics could not be fully controlled. Now, atomization provides the majority of metal powders [1, 2].

Atomization involves the formation of powder from molten metal using a spray of droplets. Different kind of powders can be fabricated by such process. It is an attractive method because of the applicability to several alloys and easy process control. Atomization relies upon fusion based technology which provides control over melt purification and alloy chemistry [1, 2].

Nowadays, the most important types of atomization that are used are:

- Gas atomization
- Water atomization

For the purposes of this study, only water atomization will be mentioned.

Water atomization

Water atomization is the most common technique for producing elemental and alloy powders from metals which melt below approximately 1600ºC. An example of water atomizer geometry is shown in Figure2. High pressure water jets are directed against the melt stream, forcing disintegration and rapid solidification. The water can be directed by a single jet, multiple jets or an annular ring. Typical mass flow rates are about five (5kg of water for every kg of metal powder).

Because of rapid cooling, the powder shape is irregular and rough, and an oxide layer covers its surface. Shape control requires superheats far above the liquidus. Chemical segregation within an alloy particle tends to be quite limited since the particles solidify rapidly. Synthetic oils or other nonreactive liquids can be used instead of water to gain better control of particle shape and oxidation [1]. Water atomization is usually followed by an annealing process in order to remove at least in part the oxide layer developed during the atomization.

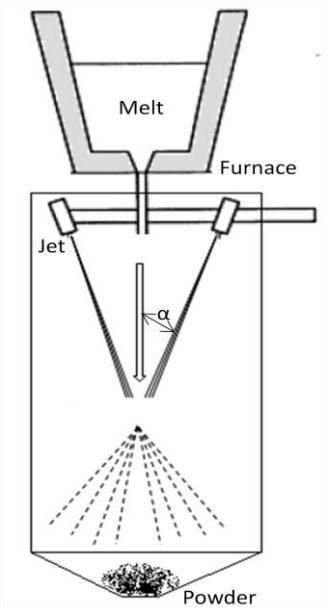

FIGURE2.THE WATER ATOMIZATION PROCESS (PLOTTED FROM [1],[2])

Pressure is the main process control variable in water atomization. Higher water pressures result in higher water velocities and smaller particle sizes [1].

Hybrid processes

Several of the more important commercial processes used nowadays involve multiple steps, incorporating two or more of the basic powder production processes. Examples include: the QMP process, which has elements of atomizing, oxide reduction and comminution steps; the Domfer process and the Copper oxide process [4].

1.2.2 COMMERCIAL PRODUCTION METHODS FOR METAL POWDERS

Iron powder

A significant percentage of iron powder produced is made by one or other of the oxide reduction processes (Höganas Sponge Iron Process, Pyron Process or similar). Although these powders grades are mostly used in powder metallurgy, the more advanced and high performance PM now use water atomized iron or steel powders because of their higher compressibility [4].

Iron powders manufactured by the hybrid QMD and Domfer processes are used in PM applications of intermediate performance requirements [4].

Low alloy steels powders

The vast majority of steel powders are produced by water atomization. In most cases, plain iron and low-alloy steel powders for PM applications are made by the atomization of re-melted steel scrap. Purification of the melt before pouring is normally required in order to remove or reduce minor residual elements.

For low-alloy steels containing nickel and / or molybdenum, these elements are usually added in the form of ferro-alloys. There are two exceptions to this rule: the Domfer process, where nickel and molybdenum are added to liquid cast iron before shotting, grinding and decarburization; and diffusion alloyed powders, where nickel, molybdenum and copper powders are blended with plain iron or steel powder and annealed to produce powder with composite particles having the nickel partially diffused into the iron [4].

1.2.3 STEEL POWDERS

Steel powders can be classified into three general types, depending on the allowing process, a schematic picture is shown in figure 3:

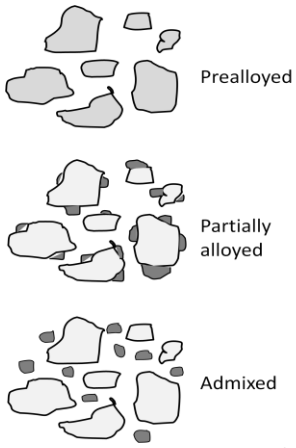

FIGURE3.SCHEMATIC MAIL ALLOYING METHODS (PLOTTED FROM [2])

- Prealloyed powders that are produced by melting and subsequent atomization, so that the alloy metals are contained already in each powder particle. They give better microstructural homogeneity, although the compositional flexibility is restricted [2, 11].

- Admixed powders that are alloyed during sintering, which requires sufficient diffusion and mass transport during the sintering process for homogeneous alloying [2].

- Diffusion alloyed powders that are similar to the admixed type, but with the difference that the powder fines for alloying are bonded to the surface of iron particle. This step reduces segregation and improves the chemical homogeneity of the alloy part after sintering [2].

1.3 Shaping and Compaction

Once the metal powder is manufactured, the shaping of a sintering component from this powder begins with its densification in a rigid die having a cavity of more or less complicated form [10]; the following basic aims during this stage are pursued:

- Consolidate powder into the desired shape.
- Give, as far as possible, the final dimension to the component, taking into account possible size changes during latter stages, e.g. during the sintering stage.
- Reduction of porosity.
- Uniform densification of the compact across its entire cross-section.
- Reach the needed strength that allows handling of the samples afterwards.

1.3.1 Compaction

There is a wide variety of processes suitable for producing a compact from powders for later transformation into a nearly fully dense material, but only relatively few of these are used on a commercial scale. These processes use either high pressure or high temperature or a combination of both to reach the desirable density level [15].

The compaction cycle that uses high pressure, can be divided into three steps:

- Filling the die
- Densifying the powder
- Removing the compact from the die

In order to facilitate the compacting operation and reduce friction to a minimum, a lubricant is admixed to the powder before compacting [10]. After filling the die, the particles rotate and reposition themselves. The powder has a density approximately equal to the apparent density. As pressure is applied, the first response is rearrangement of the particles with filling of large pores giving a higher packing coordination. The contacts points created between the powder particles are the initiation points for necks development [1, 15] later on during the sintering process.

Increasing pressure provides better packing and leads to decreasing porosity with the formation of new particle contacts: the point contacts undergo elastic deformation. Figure 4 sketches the consecutive steps in compaction [1].

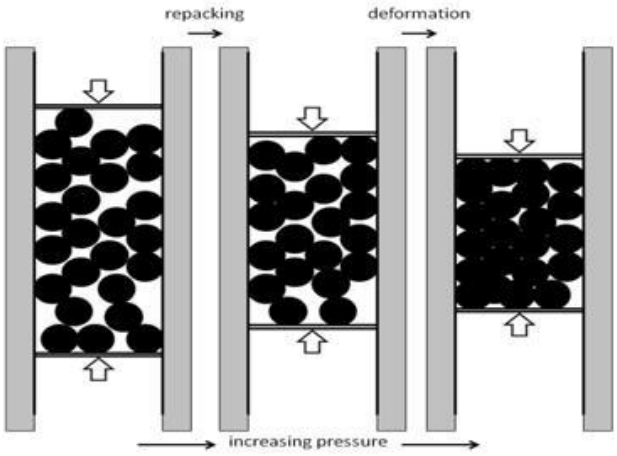

FIGURE 4. STAGES OF METAL POWDER COMPCTION (PLOTTED FROM [1])

High pressures increase density. Adhesion between particles increases with a further increase in areas of contact and increased cold-working. Thus, the pressure causes localized deformation at the contacts, allowing new contacts to form as the gaps between particles collapse [1, 15].

The mechanical cold-welding of powder particles takes place by shear deformation of surfaces, which is caused by asymmetrically opposed forces. Because of this reason, irregularly shaped particles can be compressed to high densities more easily than spherical [15].

After ejection of the die, if the compacting operation was successful, the compact owns sufficient strength (green strength) to withstand further handling without damage [10].

1.4 Sintering

1.4.1 Solid state sintering basics

As A.K. Eksi and A. H. Yuzbasioglu [9] state, sintering is the most common technique for consolidating powders. Sintering (ISO) can be defined as the thermal treatment of a powder or a compact at a temperature below the melting point of the main constituent for the purpose of increasing the strength by bonding together of the particles; it also describes the removal of the pores between the starting particles, combined with their growth and strong mutual bonding [9]. On a microstructural scale the bonding occurs as cohesive necks grow at the particle contacts, through diffusion of atoms from particle to another. Such neck growth causes mechanical properties changes [1]. The driving force behind sintering is minimization of the free surface energy of the particle agglomerate [10].

The sintering mechanism describes the path of atomic motion which produces the mass flow [1]. Bonding powder particles requires transport of material from their inside to points and areas where they are in contact with one another. In the absence of a liquid phase, five different transport mechanisms are possible [10]:

- Volume diffusion (migration of vacancies)
- Grain-boundary diffusion
- Surface diffusion
- Viscous or plastic flow
- Evaporation / condensation of atoms on surfaces

Although there is no physical formula which describes the sintering process completely [15], W. Zhang and J. H. Schneibel [6] have verified the sintering kinetics of Bross and Exner [7] using a rigorous mathematical model and a numerical approach with high stability; the mathematical model for the sintering process they have described consists of three parts: the surface diffusion effect, the grain boundary diffusion effect and the joining condition at the intersection of grain boundary and surfaces [6].

During sintering, the surface area declines rapidly from the initial value S_o, as measured by the dimensionless parameter $\Delta S/ S_o$, and provides a gauge of the degree of sintering. Another measure of sintering is the relative neck size ratio X/D, defined as the neck diameter divided by the particle diameter as illustrated in Figure [1].

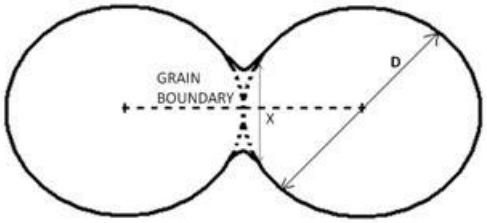

FIGURE 5. GEOMETRY OF TWO SINTERED PARTICLES (PLOTTED FROM [1],[6])

In the sintering of heterogeneous materials, alloying takes place at locations where necks are formed between particles of different metallic identity; the growth rate of the neck now depends not only on the diffusion rates in the two pure metals, but also on the different diffusion rates in the various alloy phases being formed in and on either side of the neck. The outcome of this interaction varies with the chemical identity of the two metals: it may have an accelerating, a delaying or no effect at all on the growth rate of the neck [10].

In the sintering process, packed powder particles are bonded together by the heating to improve mechanical properties such as strength, toughness and ductility: this brings out about shrinkage of the compact because of the disappearance of pores among the powder particles [7]. Shrinkage, $\Delta L/ L_o$ is the change in compact length divided by the initial dimension [1]. K. Mori, M. Ohashi and K. Osakada [7] have developed a method for simulating microscopic shrinkage behavior of powder particles during sintering.

Because of shrinkage, the compact increases its density from the green density to the sintered one ρ_S according to the relation [1]:

$$\rho_S = \rho_G/(1 - \Delta L/ L_o)^3 \qquad \text{eq 2}$$

The densification parameter ψ is the change in density due to sintering divided by the change needed to attain a pore free solid [1]:

$$\psi = (\rho_S - \rho_G)/(\rho_T - \rho_G) \qquad \text{eq 3}$$

where ρ_T is the theoretical density. Densification, final density, neck size, surface area and shrinking are related measures of the pore elimination process during sintering [1].

Some parameters that governed the sintering process can be highlighted: temperature and time, geometrical structure of the powder particles, composition of the powder mix, density of the powder compact and composition of the protective atmosphere in the sintering surface [10].

Attending to the first parameter, the higher the sintering temperature, the shorter is the sintering time required to achieve a desired degree of bonding between the powder particles in a powder compact. This constitutes a dilemma: from the view point of production efficiency, shorter sintering times would be preferable; but the correspondingly higher sintering temperatures are less economical because of the higher maintenance costs and the higher energy consumption for the sintering furnace [10].

1.4.2. STAGES

The most general form of industrial sintering consists of the following stages: non-isothermal heating to sintering temperature, isothermal dwell at sintering temperature and relatively slow cooling to room temperature. During the heating stage, the powder mass is held at a suitable average temperature until the pressing agents (lubricants, binding agents) which are added to the powder have been eliminated to avoid residuals and contamination in the chamber, and therefore allowing adjacent powder particles to come into direct contact [15]. A simplified scheme of this process is shown in figure 6.

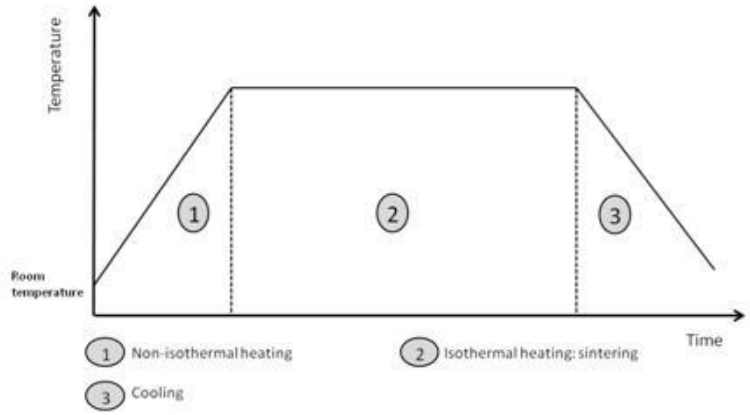

FIGURE 6. SIMPLIFIED SCHEME OF THE SINTERING PROCESS

The initial stage of sintering is the heating process up to sintering temperature, and it is characterized by rapid growth of the inter-particle connections [1]; the pores are connected and discrete necks exist between particle; in this initial stage, volume diffusion is the predominant mechanism for metal particles [10, 24].

In the intermediate stage, the pore surfaces are of almost constant curvature and the contributions to pore shrinkage are surface and grain boundary diffusion from grain boundary resources; therefore, the pore structure becomes smoother. The basic geometry of the pores resembles the initial stage of sintering and has an interconnected, cylindrical nature. It is common for growth to occur in the latter portion of the intermediate stage of sintering, giving an average grain size with fewer grains. That is accompanied by possible pore isolation at a lower sintering rate [1, 25].In the late stage of sintering, volume diffusion is, responsible for the phenomenon of pore rounding [10].

Bonds between contacting particles enlarge and merge as sintering progresses on the created contacts. At each contact, a grain boundary grows: prolonged sintering causes the two particles to coalesce into a single sphere [1]. This is sketched in figure 7.

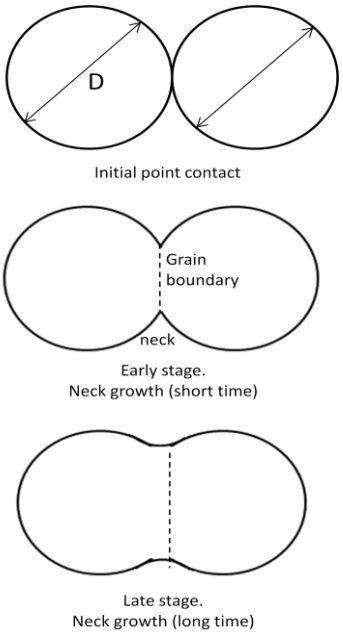

FIGURE 7. TWO SPHERE SINTERED MODEL (PLOTTED FROM [1])

No clear distinctions exist between the sintering stages. The initial stage generally corresponds to a microstructure with large curvature gradients. Both the neck size rate and shrinkage are small and the grain size is no larger than the initial particle size. In the intermediate stage, the pores are smoother and the density is between 70 and 92% of the theoretical. Grain growth occurs late in the intermediate stage, so the grain size is larger than the initial particle size. By the final stage of sintering, the pores are spherical and closed, and grain growth is evident. Spherical pores are desirable at the final stage of densification [1]. The sintering stages are illustrated in figure 7.

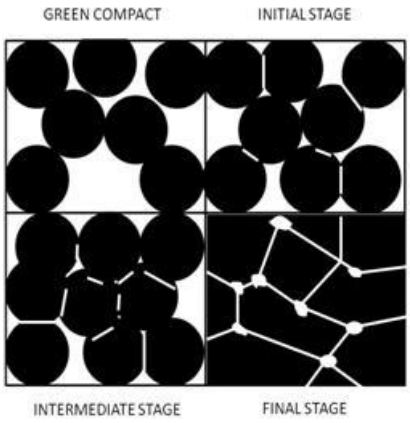

FIGURE 8. SINTERING STAGES

Pore structure development during sintering

During sintering, the contact points between particles grow into necks. After the initial stage, the grain boundary and pore configuration controls the sintering rate. At the beginning of the intermediate stage, the pore geometry is highly convoluted and the pores are located at grain boundary intersections. With continued sintering, the pore geometry approaches a cylindrical shape where densification occurs by decreasing the pore radius. A simplified sketch is displayed in Figure 9 [1].

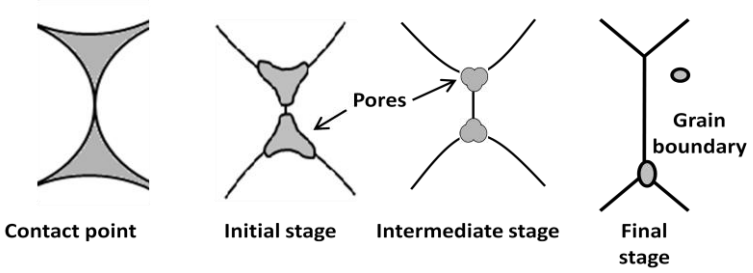

FIGURE 9. PORE STRUCTURE DEVELOPMENT DURING SINTERING (PLOTTED FROM [1])

In the latter stage of sintering, interaction between pores and grain boundaries can take three forms: the pores can retard grain growth, the pores can be dragged by the moving grain boundaries during grain growth, or the grain boundaries can break away from the pores, leaving them isolated in the grain interior. At the typical sintering temperatures, most materials exhibit moderate to high growth rates. As the temperature is raised, the rate of grain boundary motion increases; breakaway of the boundaries from the pores occurs because the pores are slower moving than the grain boundaries. At low temperatures, the rate of grain growth is small, pores remain attached and impede it. Under the tension of a moving grain boundary, pores move by volume diffusion, surface diffusion, or evaporation-condensation across the pore. But at high temperatures the rate of grain growth increases to a point where the boundaries break away from the pores [1].

1.4.3 Protective Atmospheres

Protective atmospheres are used during sintering in order to prevent oxidation in the compact and to reduce superficial oxides while maintaining the desired composition, what in fact enhances inter-particle necks development. Some of the functions of the atmosphere are:

- Help with the lubricant burnout.
- Avoid oxides formation and reduce existing oxides during heating.
- Prevent carbon loss (decarburization).
- Avoid re-oxidation during cooling.
- Avoid non desirable air flows.
- Provide homogeneous sintering results.

Due to their porous structure, pressed powder components react more readily with the surrounding atmosphere than fully dense materials; for this reason, the choice of the sintering atmosphere is very important. The protective atmospheres used are mainly gases or vacuum [15].

The choice of the gas must take into consideration possible reactions between the gas, the material to be heated and the furnace. Additional gases may be produced during annealing due to interactions with the sintering components; this is why, one of the tasks of the protective atmosphere is to prevent oxidation of the compacts during sintering, and reduce any oxide skins remaining from the powder processing, so that the contact between powder particles and thus material transport during sintering are not inhibited [15].

The protective atmosphere most widely used in sintering, are:

- Oxidizing atmospheres
- Vacuum
- Pure gasses
- Dissociated (cracked ammonia)
- Protective gases produced by burning hydrocarbons

Pure gasses

Hydrogen (H_2) is the most common of the commercially pure gases; it provides the most effective reducing atmosphere. Because of the high danger of explosion, (Hydrogen-air mixtures are explosive in the range of 4 to 74% H_2) special safety precautions must be taken into consideration. Hydrogen is often combined with nitrogen (N_2) as a cheap and explosion-safe inert gas or purging gas, especially for metals such as iron and copper which do not react readily with the furnace gas [15].

However, the limited permeability of the sintering atmosphere for relatively dense green compacts, makes that the main interaction between the gaseous mixture and the green body takes place on its outer surface, so the reducing effect it is not enough towards the internal oxides. Graphite additions are required, and the atmosphere provides the mass transport mechanism for transferring carbon to the surface of the oxidized particles, thus resulting in the reduction of the internal oxides after which necks are developed [18].

Nitrogen when mixed with hydrogen is suitable for sintering any iron or copper alloy. The hydrogen content used in the gas mixture depends on the type and composition of the alloy. If the components to be sintered contain significant oxides, these are reduced by the hydrogen and form water vapor. This has a decarburizing effect; for this reason, a carburizing gas such as propane is mixed into the sintering atmosphere in those cases where decarburization is possible but undesirable [15].

1.4.4. Reactions occurring during sintering process

As confirmed by H. Danninger and C. Gierl [22], there are some processes during sintering that strongly affect the properties of the final component, such as lubricant and additives burnout, changes of the particle surface chemistry (oxides formation and removal), formation and growth of solid metallic bridges out of pressing contacts and dissolution of alloying elements.

These processes may be produced or enhanced by reactions that occur during the sintering stage, which as H. Karlsson [5] indicates can be listed as follows:

- Reactions involving the sintering atmosphere (H_2 and O_2).
- Carbothermal reactions and other reactions involving carbon.
- Mass transfer of oxidants from the interior of the metal particle to the surface during the sintering process.

They will be referred in detail in a later section.

1.4.5. Oxides stability and removal in Cr-Mo-prealloyed steels

Chromium pre-alloyed steel powders are manufactured by water atomization followed by a reduction process to remove the thick oxide layers generated during atomization; the oxide layer is reduced, but some oxidation occurs during cooling and handling of the powders [17].

As confirmed by H. Karlsson [5], the surface of the chromium pre-alloyed powder is covered by an oxide layer. This layer is made up of a homogeneous iron oxide layer, whose thickness typically varies in the range of 6-7nm, and of particulate compounds with high content of strong oxide forming elements (Cr, Mn, Si) [13]. In addition, there are certain amounts of powder oxides inside the powder particles [16].

In powder compacts, as was mentioned above, it is important to keep in mind the limited permeability of the sintering atmospheres into the powder compacts; this is important in metallic systems containing carbon, since it consequently implies that the chemical events taking place on the external surface of the powder may be different from those in its inner part, particularly after reaching high densities [18]. Furthermore, it must be taken into consideration that the porosity of the powder compact may be open or closed, or alter from open to closed during the sintering process [5].

Therefore, powder particle surfaces are the internal surfaces of a powder compact [5]. The main surface related problems when sintering powder compacts are avoiding oxidation by interaction with the atmosphere and removal of the oxide layer covering each powder particle. For successful sintering, removal of the surface oxides is of critical importance in order to encourage necks formation and develop the properties of the material [18], and so it is necessary to identify the temperature ranges and sintering atmosphere conditions where oxide reduction preferentially takes place [17].

Surface oxide reduction can be attained by sintering in suitable atmospheres, in such containing hydrogen and carbon. For steels, also inert atmospheres are viable since the carbon acts as a reducing agent [17]: the reduction media consist of not only the atmosphere, but also the carbon admixed to the powder [5]. Carbon is less effective than hydrogen at low temperatures but becomes very much so when increasing temperature [17].

As some authors assert [17], degassing and carbothermic reduction processes can be divided in three main steps:

- Initiation of the reduction of the surface iron oxide layer by hydrogen at low temperatures, up to 500°C: some mass loss occurs, because the iron-rich layer is thermodynamically less stable and so is easily reduced by hydrogen when it is used like sintering atmosphere [13, 17].

- The reducing activity of hydrogen decreases with increasing temperature. In the presence of oxygen and excess graphite, the composition of the gas phase in equilibrium conditions is controlled by the Bouduard equilibrium ($2CO \leftrightarrow CO_2 + C$). It shows which gas, CO_2 or CO, is more favorable to occur. Above 720°C, CO production is more favorable; at this temperature, CO is reducing whereas CO_2 is extremely oxidizing. At temperatures around 700 the reducing activity of carbon increases and it begins to play a dominant role: very pronounced mass loss occurs due to carbothermic reduction of surface iron oxides that are in contact with plain graphite at above 800°C [13]. At this temperature, carbon starts to dissolve in the iron matrix [13, 19, 26].

- The third stage starts at near 900°C and reaches a maximum at the beginning of isothermal sintering [13]. In this step the reduction of the oxides from internal pores which are at least open to some extent to the surface, and the reduction of the internal iron-containing oxides takes place: this is **direct carbothermic** reaction caused by reduction of oxides by dissolved carbon [19].

As H. Danninger et al conclude [17], decarburization of steels occurs in the three temperature intervals mentioned above, where the second stage experiments the most pronounced mass loss. The gasses formed are CO, and at lower temperatures, CO_2 and H_2O, which means that the de-gassing process indicates primarily carbothermic reduction of the oxides contained by the powder particles [17].

The carbothermal reduction of chromium oxides is much more difficult that of the iron oxides: only at high temperatures the stability of the chromium oxides is low enough and on the other hand the reducing power of CO is high enough to result in sufficient reduction of these oxides. For CO, the free energy of formation becomes more negative when increasing the temperature, while with all other oxides becomes less negative. Thus, carbon is a less reducing agent than H_2 at lower temperatures but becomes more effective at higher ones [17] hence inducing CO/CO_2 gas mixtures [18].

It is important to notice that the generation of CO takes place with an increase of volume of the gaseous species, and hence creating a self- generated atmosphere from the inside of the powder compact resulting in the displacement of the surrounding atmosphere [18]. Furthermore, through compaction and subsequent sintering, the total porosity decreases and therefore the final density of the compact is increased. Then, the accessibility for the sintering atmosphere to the interior of the compact being sintered is restricted, which in turn restricts the macroscopic transport of reaction products that result from reduction of surface oxides. This way, special microclimate will be developed inside semi-closed and closed pores [5].

It can be assumed that CO/CO_2 based mass transport mechanism for transferring carbon to the surface of the oxide, that is the **indirect carbothermal** reduction reaction, is the fastest and more likely reduction process in these powder systems; in addition, by creating an oxygen gradient across the particles, the internal oxides are destabilized causing their reduction by the migration of oxygen anions to the particle surface in contact with the internal atmosphere and the dissolution of chromium in the metallic matrix [18].

As H. Danninger, C.Xu, B.Lindqvist indicate [12] for Cr-Mo and Mo alloyed steels the oxygen levels after sintering are clearly related to the carbon contents; the lower the oxygen content, the higher the carbon loss during sintering. Moreover, decarburization increases with higher oxygen partial pressure, which shows that oxygen in the atmosphere picks up carbon from the material; this effect is enhanced by higher sintering temperatures and slow cooling rates, since more time is allowed for oxygen in the atmosphere to pick up carbon from the material. For Cr-Mo alloyed powder, according to these authors, oxygen removal is completed at higher sintering temperatures [12, 16].

1.4.6. THERMODYNAMICS CALCULATIONS

E. Hryha, L. Cajkova, E. Dudrova and L. Nyborg [13] have carried out thermodynamic calculations to establish the required sintering atmosphere purity during the sintering process in nitrogen / hydrogen atmosphere for chromium pre-alloyed powders, paying special attention on carbothermal reduction processes. Reactions involving the sintering atmosphere must also be taken into account (H_2 and O_2). Calculations were performed for the oxidation/reduction reactions of the oxides located on the base powder surface.

The equilibrium condition among a metal and its oxide in contact with oxygen gas at a certain temperature indicates that the reduction of the metallic oxide will occur when:

$$P(O_2)^{atmosp\ here} < P(O_2)^{oxide}$$

Where $P(O_2)^{oxide}$ represents the oxygen dissociation pressure of the oxide and $P(O_2)^{atmosp\ here}$ the oxygen partial pressure of the atmosphere [18]. For the reduction of Cr_2O_3 by graphite, the following reactions have to be considered:

$$\frac{1}{3}Cr_2O_3 = \frac{2}{3}Cr + \frac{1}{2}O_2 \qquad \text{eq. 4}$$

$$C + O_2 = CO_2 \quad \text{eq. 5}$$

$$2C + O_2 = 2CO \quad \text{eq. 6}$$
$$C + CO_2 = 2CO \quad \text{eq. 7}$$

The algorithm for the sintering gas conditions was developed for Mitchell [14], and it was also used in the mentioned study [13]. Since:

$$\Delta G_T^0 = \Delta H - T\Delta S \quad \text{eq. 8}$$

and

$$\Delta G_T^0 = -R \cdot T \ln K_p \quad \text{eq. 9}$$

The changes in the free energy of Gibbs of oxide formation are a measure of how readily the material oxidizes. From the free energy values at a given temperature, the pressure balance between reducing / oxidizing gases can be obtained an is summarized in Richarson – Ellingham diagram (Figure 10) [19].

Hryha et al [13] used the database of the computer software HSC Chemistry 6.1, in order to obtain the free energy changes and therefore the equilibrium constants. Thereby, the composition for the atmosphere at 1393K for Cr_2O_3, Cr and C in equilibrium with a gaseous atmosphere can be calculated.

For the first reaction, the oxygen partial pressure was estimated using the equilibrium constant value, whose value is $K_P = 2{,}163 \cdot 10^{-10}$. For this reaction $K_P = P(O_2)^{1/2}$, so:

$$K_P = P(O_2)^{1/2} \rightarrow P(O_2) = (K_P)^2 = 4{,}67 \cdot 10^{-20} atm$$

This result agrees with the thermodynamic calculations carried out by O. Bergman [16], which demonstrates that the oxygen partial pressure should be below $4 \cdot 10^{-18}\ atm$ in order to have reducing conditions during sintering and by P. Ortiz and F. Castro [18] where the thermodynamic condition for reducing the internal oxides requires that an oxygen partial pressure below $5 \bullet 10^{-18}\ atm$.

Now, considering that C reduces Cr_2O_3 to produce Cr + O:

$$\frac{1}{3}Cr_2O_3 + C = \frac{2}{3}Cr + CO \quad \text{eq. 10}$$

The CO partial pressure can be calculated. For equation 10:

$$K_P = P(CO) \rightarrow P(CO) = (K_P) = 0{,}135 atm$$

CO is in equilibrium with C and CO_2, so from equation 7:

$$K_P = \frac{P(CO)^2}{P(CO_2)} \rightarrow P(CO_2) = \frac{P(CO)^2}{K_P} = 3{,}36 \cdot 10^{-5} atm$$

Finally, the reaction between carbon and water vapor needs to be taken into consideration as well:

$$C + H_2O = CO + H_2 \quad \text{eq. 11}$$

$K_P = 247{,}7$

For the nitrogen / hydrogen sintering atmosphere of composition 90% N_2/10% H_2:

$$K_P = \frac{P(H_2) \cdot P(CO)}{P(H_2O)} \rightarrow P(H_2O) = \frac{P(H_2) \cdot P(CO)}{K_P} = 5{,}45 \cdot 10^{-5} atm$$

The water partial pressure corresponds to a dew point close to -45ºC, what means that an atmosphere with a dew point below -45ºC is required for reduction of chromium oxide in the N_2/H_2 (90/10) atmosphere at 1120ºC.

To sum up, the value of the partial pressures obtained:

$$\mathrm{P(CO)} = 0{,}135 atm$$
$$\mathrm{P(CO_2)} = 3{,}36 \cdot 10^{-5} atm$$
$$\mathrm{P(O_2)} = 4{,}67 \cdot 10^{-20} atm$$
$$\mathrm{P(H_2O)} = 5{,}45 \cdot 10^{-5} atm$$

As was said above, the oxygen partial pressure should be below $4 \cdot 10^{-18}\ atm$ in order to have reducing conditions during sintering. Moreover, the CO partial pressure controls if reduction or oxidation takes place. If:

$$P(CO) < P(CO), eq$$

carbothermic reduction occurs; otherwise the atmosphere oxidizes the metal [17].

Considering the value of the partial pressures obtained, the CO/CO_2 ratio can be calculated, resulting:

$$\mathrm{CO/\ CO_2} \approx 4 \cdot 10^3$$

The H_2/H_2O ratio can be also calculated as follows:

$$\mathrm{H_2/\ H_2}O \approx 1{,}8 \cdot 10^3$$

Since it is 10% H_2.

Plotting these values into the Ellingham-Richardson diagram (Figure 10), it results that for the conditions described above, the reduction of chromium oxides will take place above at 1120°C.

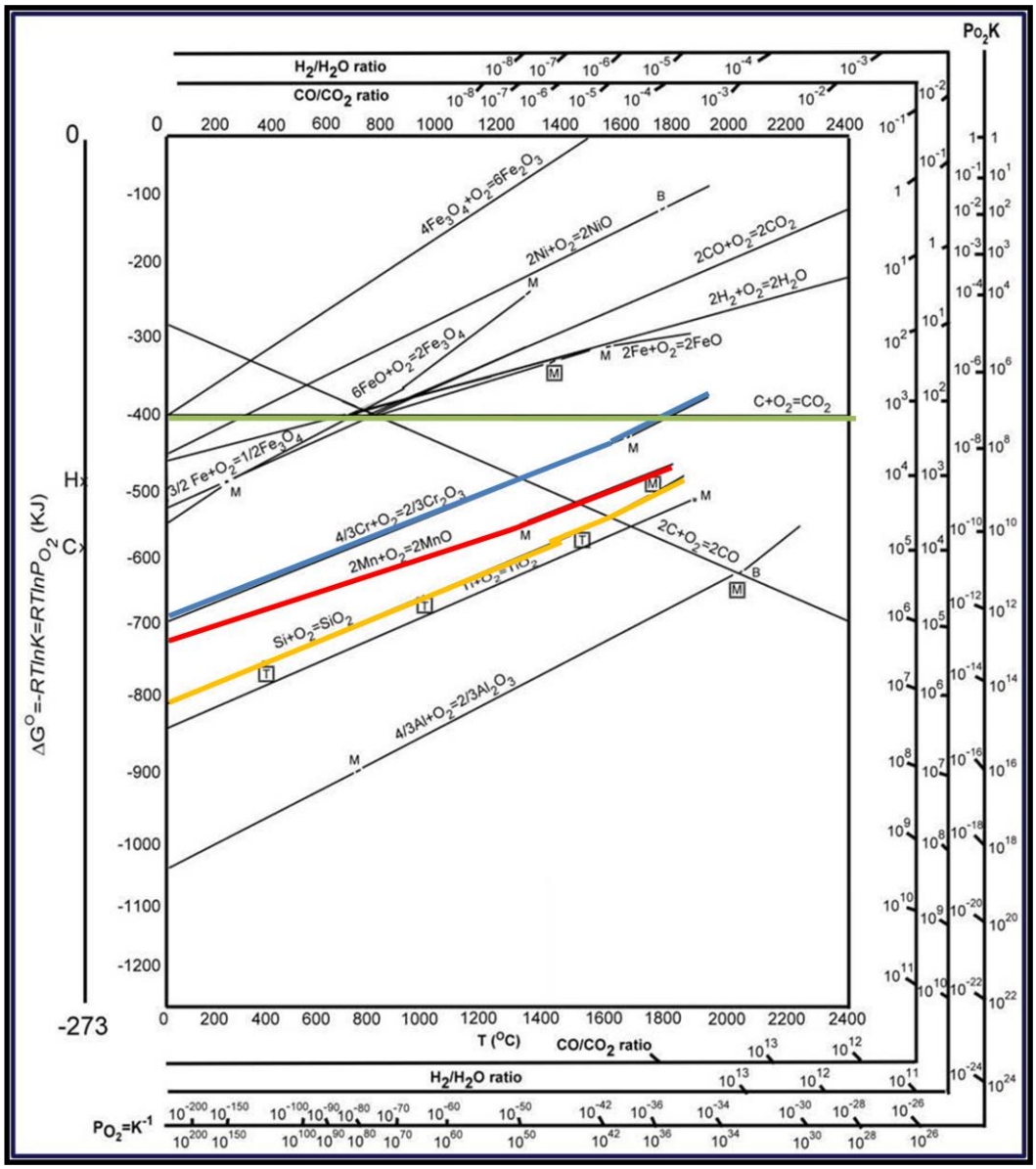

FIGURE 10. ELLINGHAM-RICHARDSON DIAGRAM (PLOTTED FROM [19])

Considering the description of the system that was made above, both CO and CO_2 are formed during the carbothermal reduction of chromium oxides; in total agreement with the Ellingham-Richardson diagram for the formation of oxides, CO/CO_2 gas mixtures are more reducing as the CO level in the mixture is higher [18].

1.4.7. FURNACES

The main function of the sintering furnace is to process the components to be sintered under conditions which ensure densification of the parts in line with their final application. The factors that limit the choice of furnace construction are [15]:

- Temperature
- Cycle time
- Sintering atmosphere
- Throughput
- Accuracy to which temperature and time must be maintained

The sintering furnaces more widely used in powder metallurgy, can be divided in two groups: continuous sintering furnaces and batch-type sintering furnaces [15].

Tube furnaces

Tube furnaces belong to the group of the batch-type sintering furnaces. They are used for the production of individual or small number of parts, or for large compacts. Very simple in construction, they are sometimes used for vacuum sintering at temperatures up to 3000ºC. The compact to be sintered is heated to the required temperature directly by electrical resistance or indirectly with the help of resistive or inductive heating elements [15].

1.5 Materials

The properties of a component manufacture by PM techniques may be tailored or improved by the addition of alloying elements; traditionally, the common alloy metals for sintered steels have been copper, nickel and in part molybdenum due to the low stability of their respective oxides; nowadays, they are currently regarded with some disfavor, because of their recycling and health hazard problems and because of their high price. For these reasons, and also because of the increasing requirements towards mechanical properties, chromium, manganese and silicon are increasingly being used as alloying elements, and sometimes as substitutes of copper and nickel [2, 11, 27].

Carbon

Carbon is the most efficient, effective and of lowest cost alloying element used in powder metallurgy. In steel PM parts made from prealloyed or diffusion alloyed powders and due to compactability reasons, it is usually mixed as graphite to form steel during sintering: this way, it increases strength and hardness of steels and compressibility is not reduced. It is an austenite stabilizing element. As was already mentioned, during the sintering stage, carbon acts as reducing agent [5, 22].

Chromium

Chromium is the most common alloy element in heat treatable structural steels; it increases hardenability, mechanical properties and hardness, as it has a solid solution strengthening effect. It has a high affinity to carbon, what strongly improves strength at higher temperatures, and is a ferrite stabilizing element. Additional advantages of chromium as an alloying element in powder metallurgy are its low cost and good recyclability as compared with other elements widely used in powder metallurgy, such as copper [2, 5, 11, 21].

In contrast, the usage of chromium in low alloyed powder metallurgy steels has been very limited. The reason for this is that chromium has a high affinity for oxygen, which makes material sensitive for oxidation during processing and because it also reduces compressibility [16]. Recently, new pre-alloyed PM steels powders have been developed based on Fe-Cr-Mo and Fe-Cr-V [17].

Manganese

Manganese, which is one of the cheapest alloy metals, is present in virtually any cast or wrought steel up to 0.8%, without the steel being classified as alloyed steel. It can be added to increase hardenability. Manganese stabilizes bainite: it does not form stable carbides, and thus does not improve the resistance of steels to grain coursing during austenitising [2, 5, 11].

Manganese is also a strong oxide former, which requires better atmosphere control or higher furnace temperatures during sintering. During this process, part of the manganese vapor escapes from the compact into the surrounding atmosphere, resulting in a manganese vapor shell where manganese reacts with the oxygen in the atmosphere as a consequence of its high affinity for it. The result is a self-cleaning effect for the sintering atmosphere [5, 11].

In contrast, manganese (due to oxide formation and significant solid-solution hardening) degrades powder compressibility of prealloyed steel powders; therefore, even though manganese is a powerful hardenability agent in steels, it is not commonly used in excess of 0.5% in prealloyed powders [2].

Molybdenum

Molybdenum is more rarely used because of its high price and is employed mostly as an additive to chromium steels or, in higher concentrations, in various tool steel grades. Like manganese, it increases hardenability and stabilizes bainite. On the other hand, it has a strong affinity to carbon, like chromium. Molybdenum addition also makes manganese and chromium alloyed steel insensitive to temperature embrittlement [2, 11].

Sulphur

Sulphur is sometimes considered as an impurity in powder metallurgy; some other times it is used when machinability wants to be enhanced. Besides, sulphur is a surface active element that can round the pores, what leads to a decrease in the risk of crack formation and subsequent propagation [5].

Sulphur reacts with manganese, producing MnS, what coherently consumes manganese from the matrix. These inclusions can act as crack initiators, reducing the mechanical properties of the material [5].

Silicon

Silicon is often used in powder metallurgy because it avoids oxidation during atomization in some kinds of steels, e.g. in stainless steels. Like chromium, it is a ferrite stabilizing agent. On the other hand, silicon can reduce compressibility and their oxides, as can be seen in figure 10, are the most stable as detrimental effects [5]. The decrease in compressibility produced by some of the alloying elements studied in this section is plotted in figure 11.

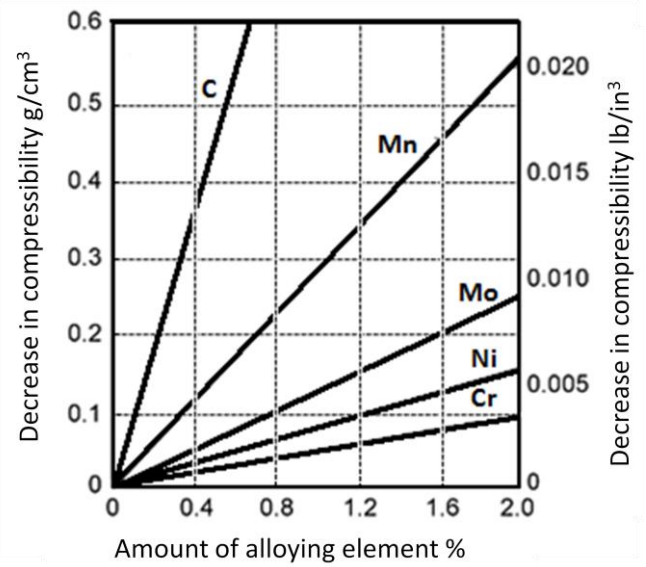

FIGURE 11. DECREASE IN COMPRESSIBILITY VS. AMOUNT OF ALLOYING ELEMENT ADDED (RE-PLOTTED FROM [2])

2. EXPERIMENTAL PROCEDURE

In this project, a pre-alloyed water atomized steel with low Cr-Mo content provided by Höganäs AB, Sweden was used as test material. The nominal composition of the powder is shown in table (1).

Table 1. Chemical composition of investigated powder grade, wt %

Alloying elements	Cr (wt %)	Mo (wt %)	C (wt %)	O (wt %)	Fe (wt %)
Material	1.5	0.2	< 0.01	0.15	Bal

The manganese content is less than 0.1 wt% and traces of other elements were also encountered. The powder was mixed with 0.5% Graphite. Kenolube 0.6% was added to the blend as lubricant. The powder mixes were uniaxially compacted at 600 MPa into impact test bars (55 x 10 x 10 mm^3). The green density of the compact was approximately 7 $g \cdot cm^{-3}$.

After pressing, the sintering process of the green bodies was carried out in a tube furnace in a $90N_2/10H_2$ atmosphere with dew point below -45ºC. Heating rate to the peak sintering temperature was 10°C min^{-1}. After the dwelling time, the specimens were slowly cooled down to room temperature (1.3°C min^{-1}). The sintering temperatures and times for the specimens are shown in table (2).

Table 2. Sintering temperatures and times for the powder mixes.

Temperature (ºC)	700	800	900	1000	1120	1120	1120
Time (min)	3	3	3	3	3	15	30
Specimen Denomination	A700-3	A800-3	A900-3	A1000-3	A1120-3	A1120-15	A1120-30

In this study, the inter-particle necks development during sintering was investigated; for this purpose, Impact test was performed in all the specimens so as to produce the fracture surfaces (see fig. 13). For Fractographic investigation, a high resolution field emission Scanning Electron Microscope (SEM) Leo 1550 Gemini was used (Voltage 15kV; aperture 20µm). The microscope was equipped with a Link Energy Dispersive X-ray (EDX) instrument for quantitative elemental analysis and an in-lens secondary electron detector (see Fig. 12). This equipment was used in order to estimate both the development of the inter-particle connections with temperature and time and the presence of inclusions.

FIGURE 12. EQUIPMENT USED (A) SEM B) OPTICAL MICROSCOPE)

For microstructural analysis the specimens were polished up to 1µm with diamond paste and observed under Leica optical microscope (see fig. 12). The analysis was performed in non etched and etched states. The etchant used was a 2% nital solution. Figure 13 shows the specimens.

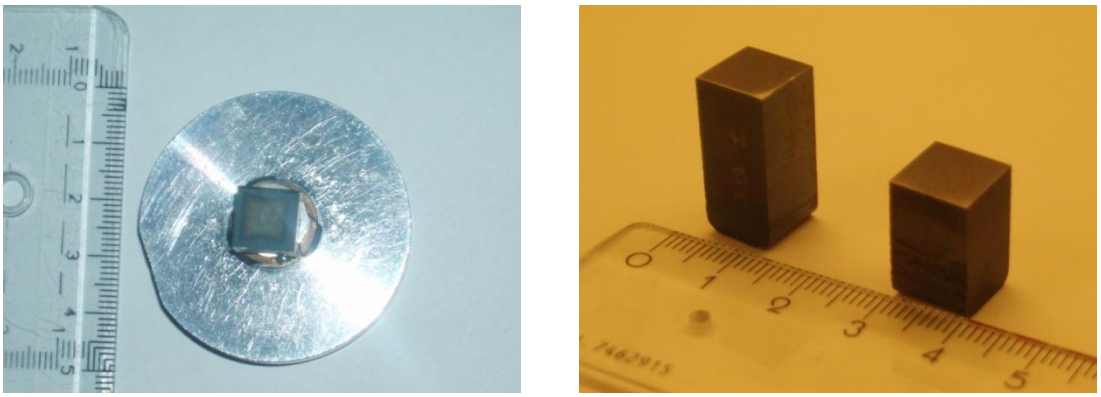

FIGURE 13. SPECIMENS (A) FRACTURE SURFACE, B)POLISHED)

3. RESULTS

Simulations were performed using the software JMat-Pro 4.0 prior to the microstructure study in order to estimate the expected phases.

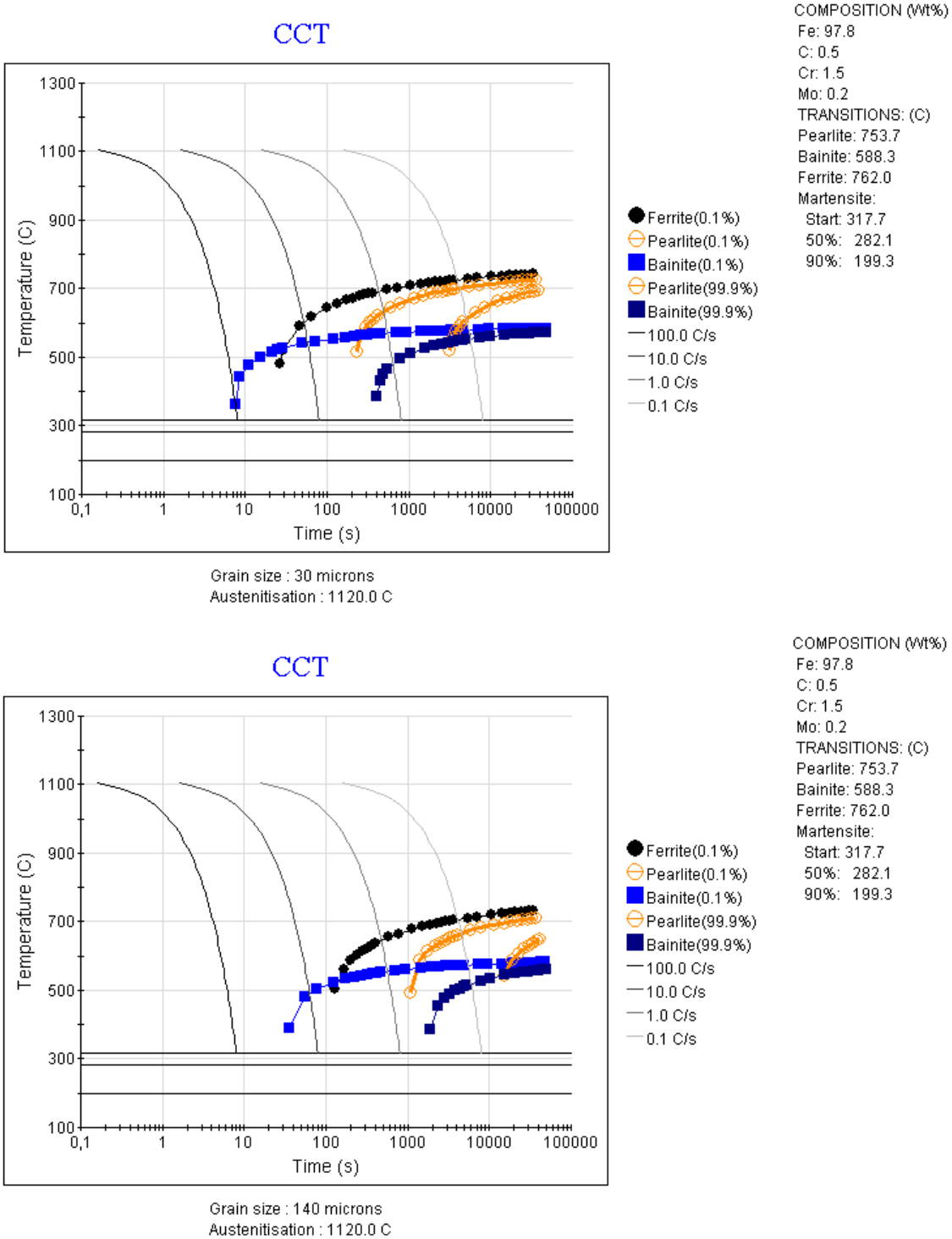

FIGURE 14. CCT DIAGRAM FOR THE TEST MATERIAL AND COOLING RATE.

The CCT diagram shown in figure 14 A predicts that for the low cooling rate used (0.02 °C•s^{-1}) only ferrite and pearlite will be presented. This CCT diagram was plotted for a grain size of 30µm, which is adequate for lower sintering temperatures. For higher sintering temperatures the diagram plotted

for a grain size of 140µm (see fig. 14 B) shows that for the cooling rate (0.02 °C•s^{-1}) only ferrite and pearlite will be presented as well.

Besides, in fig. 15 it is shown the portion and expected phases for cooling rates of A)0.02°C•s^{-1} and B) 1 °C•s^{-1} for a grain size of 30µm and 140µm. For low cooling rates and both grain sizes (see fig 15 A and C) the phases present are ferrite and pearlite; the expected portion for the latter is close to 90% in both cases. On the other hand, when increasing the cooling rate, bainite appears and becomes the most abundant phase for both grain sizes, while the portion of pearlite decreases considerably (fig. 15 B and D). For a grain size of 140µm (fig. 15D) also small portions of martensite can be found.

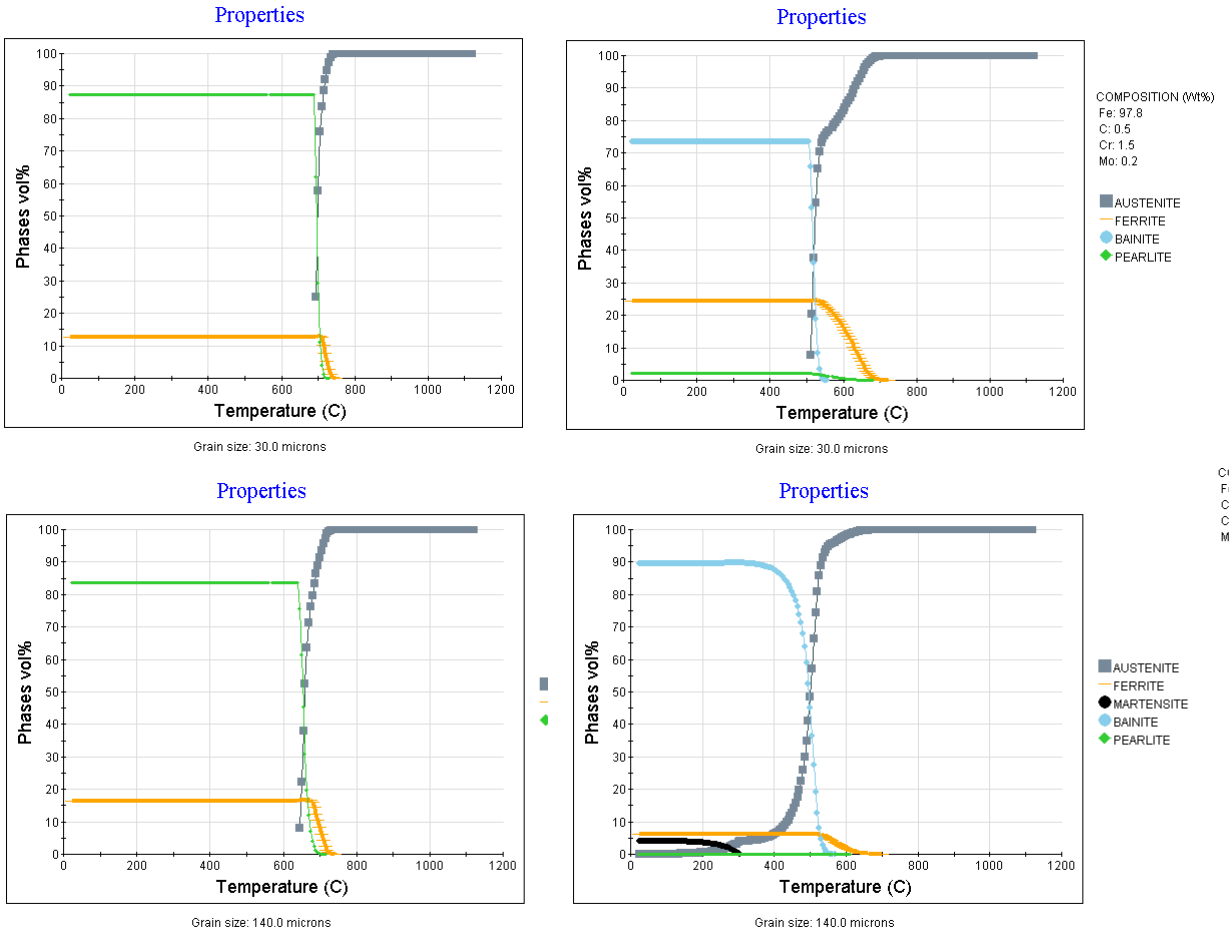

FIGURE 15. PHASES VOL.% VS TEMPERATURE (°C).

A700-3

In figure 16 are presented the microstructures of specimens sintered at 700°C in as-polished state. Some internal oxides, uniformly distributed inside the powder, with sizes below 1µm can be distinguished. In these pictures, both big irregular pores and particle boundaries are evident.

In all the microstructures for different specimens pores will be shown with arrows, internal oxides with circles and pearlite with squares.

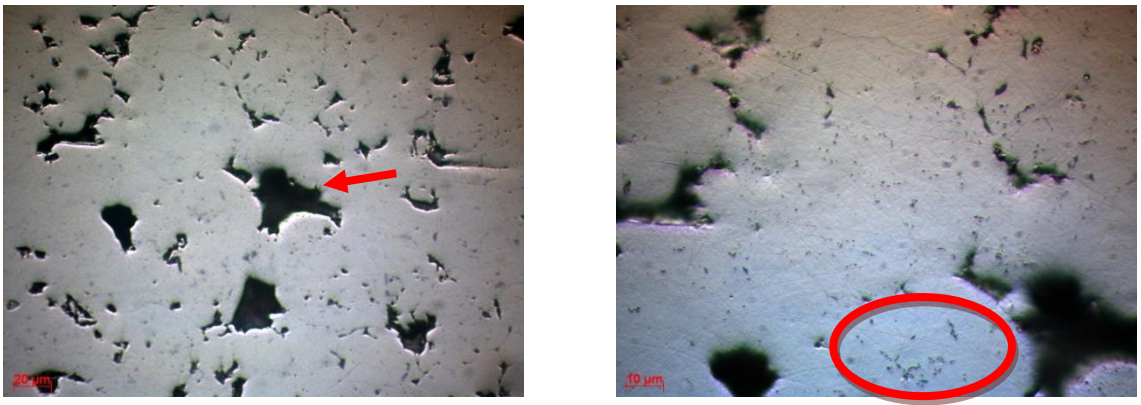

500x 1000x

FIGURE 16. SPECIMEN A700-3 IN AS-POLISHED STATE.

Picture 17 (A and B) shows the etched microstructure of material A, showing ferritic homogeneous microstructure.

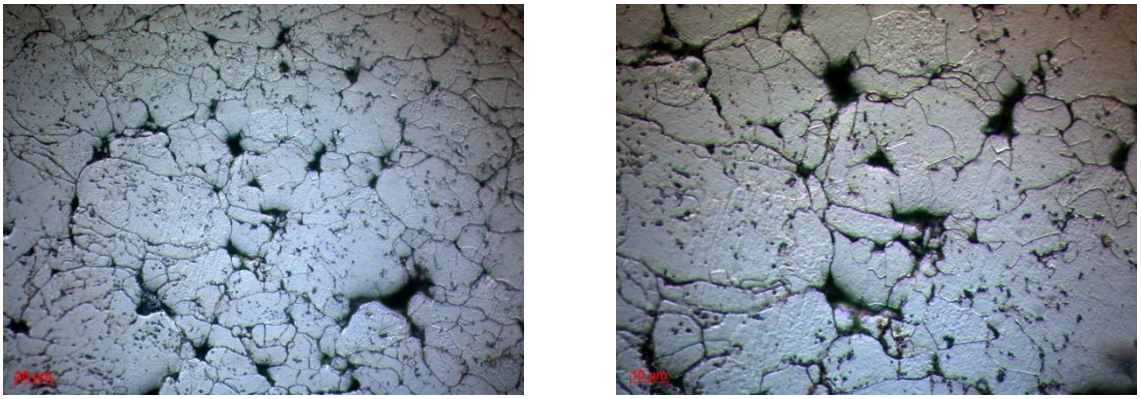

500x 1000x

FIGURE 17. SPECIMEN A700-3 ETCHED.

Figure 18 shows the overview of the fracture surface of the sample sintered at 700°C during 3minutes. The fracture surface is rough, particles and their agglomerates can be easily distinguished.

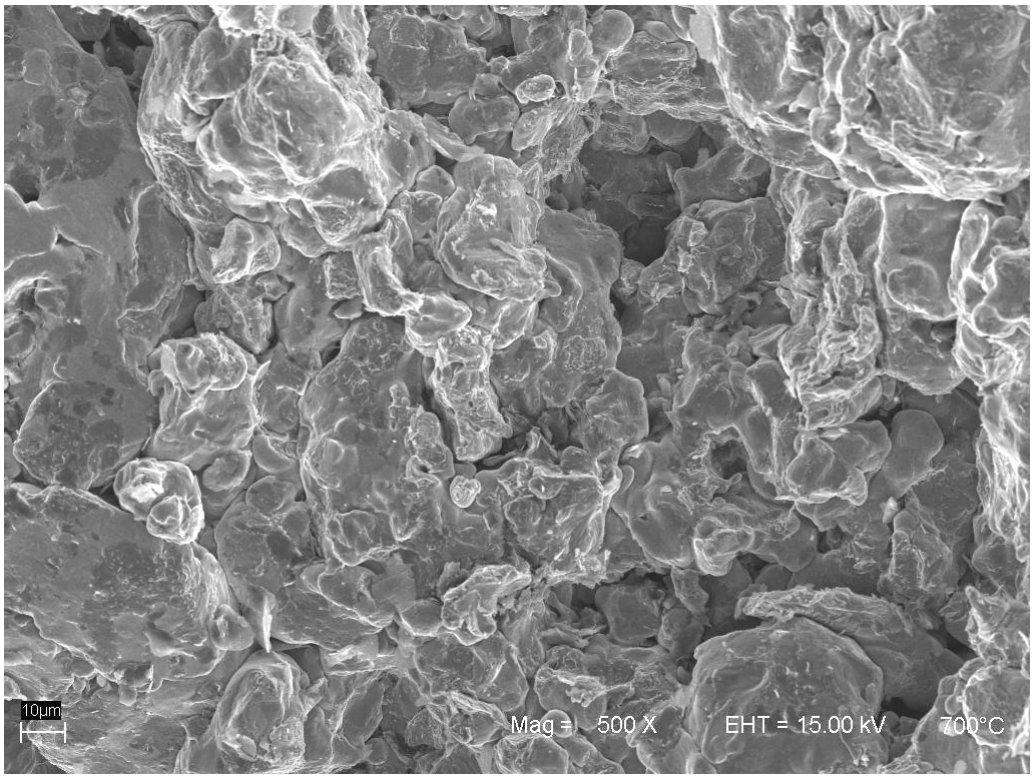

FIGURE 18. FRACTURE SURFACE OF A700-3 AT 500X.

For A700-3, weak inter-particle connections can be seen. Inter-particle point and short line ductile fracture is the main failure micro-mechanism for this specimen. Some remaining of the surface oxide layer is still present, that describes lower amount of developed inter-particle connections. See Appendix I.

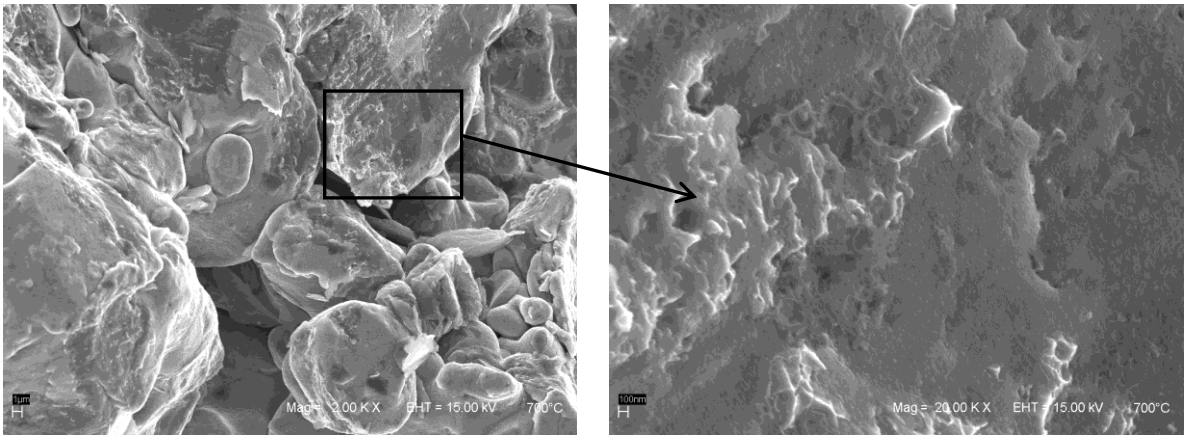

FIGURE 19. FRACTURE SURFACE OF A700-3.

Analysis of the fracture surface at higher magnification indicates (see Fig. 20 and Appendix I) presence of irregular particulate features inside the inter-particle necks with size up to 0.5 µm, which is comparable with the size of the particulate features on the initial powder surface [5]. SEM combined with EDX analysis indicate high manganese and chromium content in the particulate features. However as it is evident from the Fig.21 interaction volume is much bigger than particulate features size that together with influence of the geometry of fracture surface gives possibility to make only qualitative chemical analysis of particulate features composition; this fact must be taken into consideration for all the specimens analyzed.

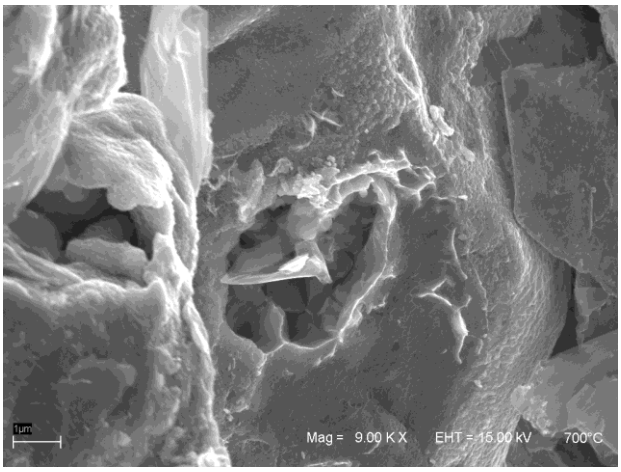

FIGURE 20. FRACTURE SURFACE OF A700-3 AT 9000X.

It is common that particulate features create agglomerates sizing up to 2µm. (see figure 21 and Appendix II)

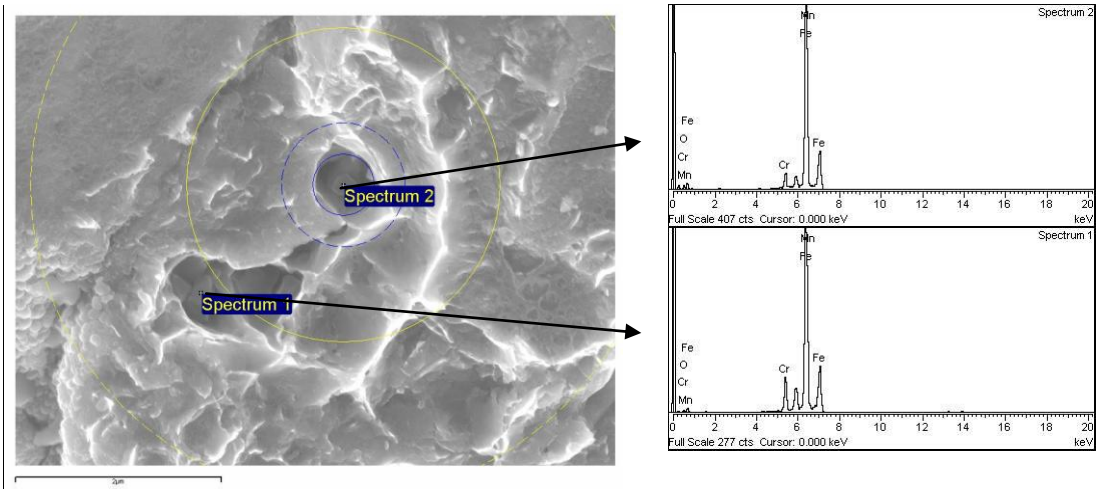

With Oxygen					
Spectrum	O	Cr	Mn	Fe	Total
Spectrum 1	0.00	7.87	6.74	85.40	100.00
Spectrum 2	2.55	4.46	3.83	89.16	100.00

Without oxygen				
Spectrum	Cr	Mn	Fe	Total
Spectrum 1	7.87	6.74	85.40	100.00
Spectrum 2	4.57	3.93	91.50	100.00

FIGURE 21. SEM+EDX ANALYSIS OF A700-3.

A800-3

Microstructures of specimen A800-3 in as-polished state are presented in figure 22. Like in specimen A700-3, internal oxides uniformly distributed inside the powder and sizing up to 1µm can be identified. Irregular pores and particle boundaries are visible as well.

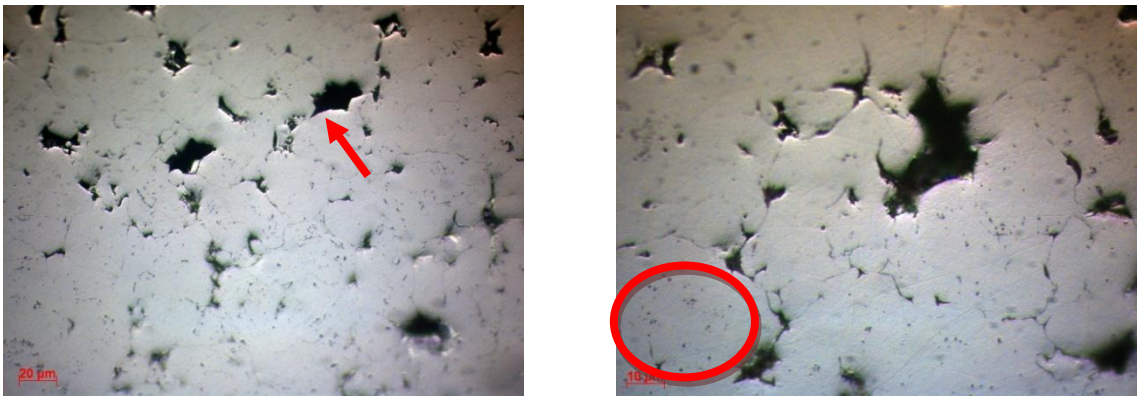

500x 1000x

FIGURE 22. MICROSTRUCTURE OF A800-3 IN AS POLISHED STATE.

In turn, figure 23 (A and B) shows the etched microstructure of A800-3, showing ferritic homogeneous microstructure. Pearlitic microstructure has firstly been registered in this specimen in small amount (~5%) close to the particle boundaries.

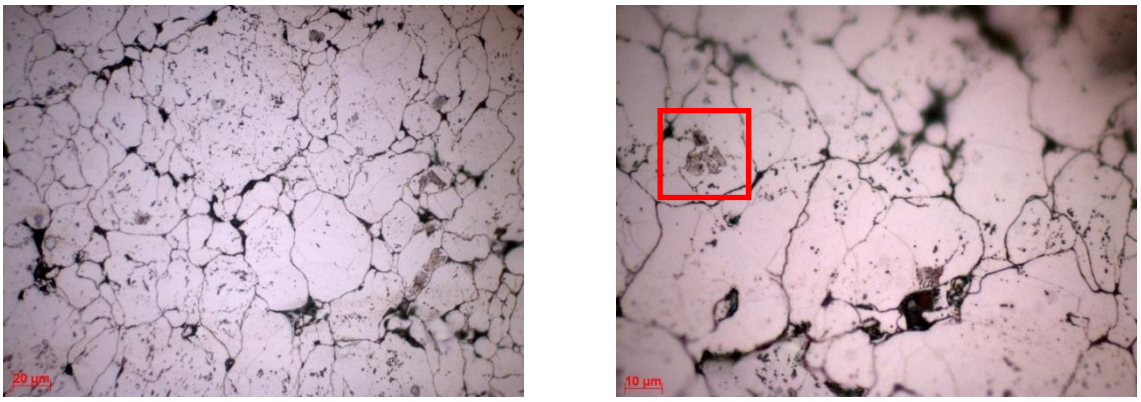

500x 1000x

FIGURE 23. MICROSTRUCTURE OF A800-3 ETCHED.

The overview of the fracture surface for A800-3 can be seen in figure 24. It is rough and particles and their agglomerates can be easily distinguished.

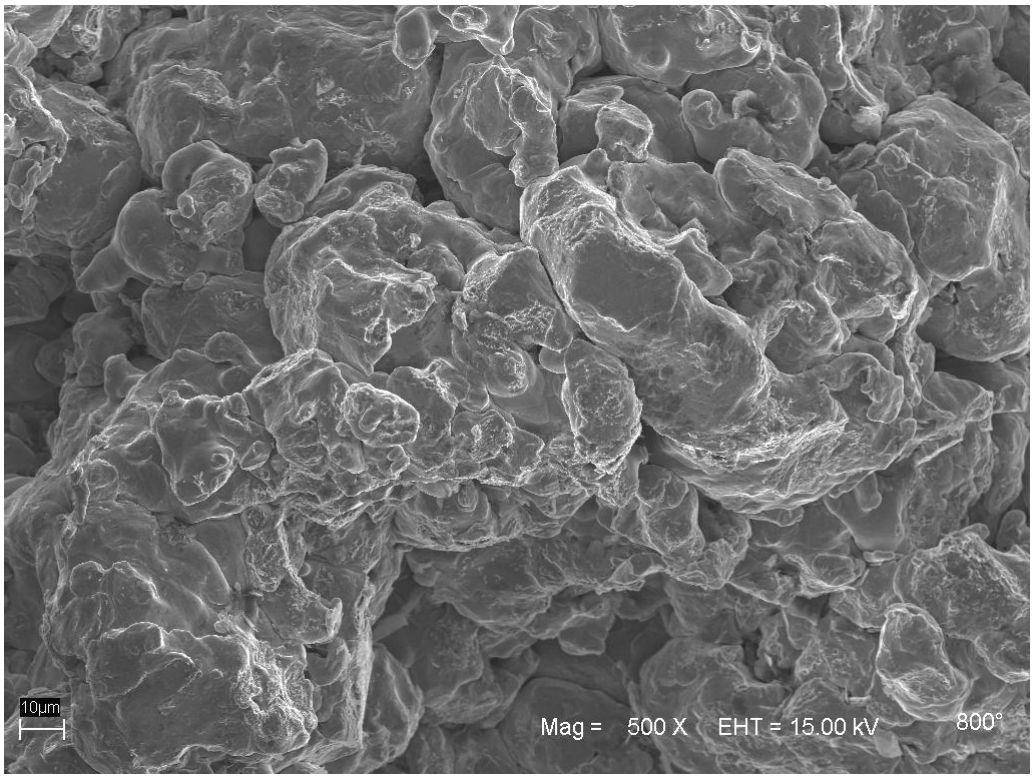

FIGURE 24. FRACTURE SURFACE OF A800-3 AT 500X.

For A800-3 inter-particle point, line and branched ductile fracture is the main failure micro-mechanism. Some remaining of the surface oxide layer is still present. However it is "purer" when compared with A700-3. This implies that the development of inter-particle connections is higher in comparison with A700-3. See also figure 25 and Appendix I.

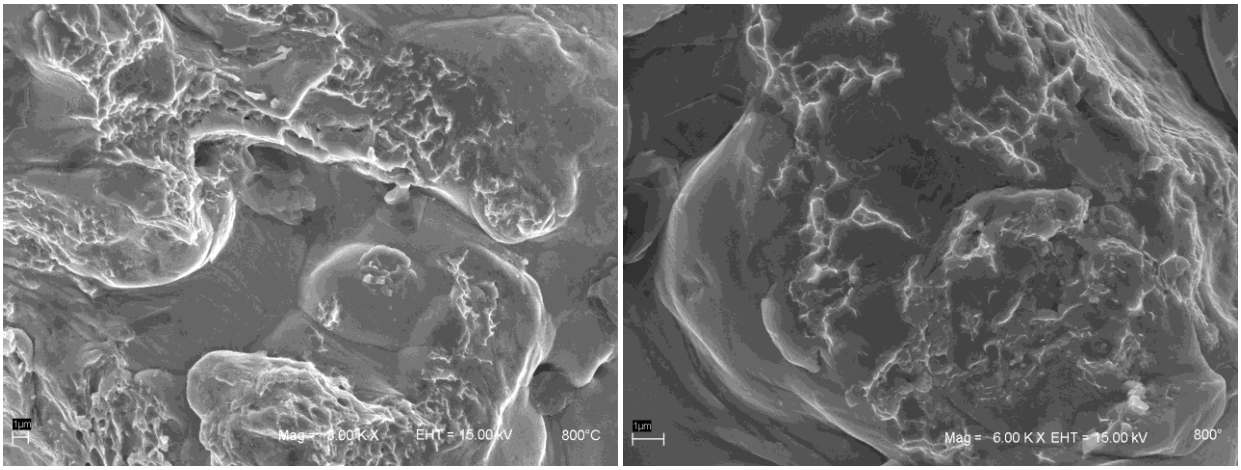

FIGURE 25. FRACTURE SURFACE OF A800-3.

Close to the edges of the specimen, more developed networks of inter-particle connections can be identified when compared with the inner part of the specimen. See figure 26.

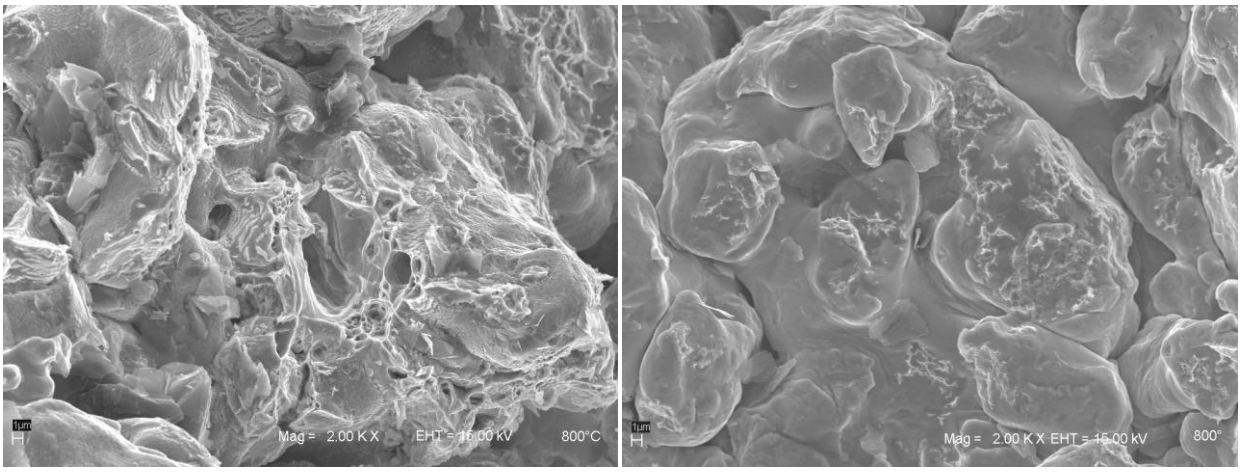

FIGURE 26. INTER-PARTICLE NECKS DEVELOPMENT IN DIFFERENT PARTS OF THE FRACTURE SURFACE OF A800-3.

Larger amount of particulate features, with irregular shapes and size up to 0.5µm, can be found in A800-3 rather than in A700-3. Heavily contaminated areas that probably are originated from the base powder were also very rarely seen. Fig. 27 (see Appendix II) shows a SEM combined with EDX analysis that indicates that particulate features are complex refractory oxides with high manganese and chromium content. It "seems" that the manganese and chromium content has increased when compared with A700-3 but because of the accuracy of the method no safe conclusions can be drawn.

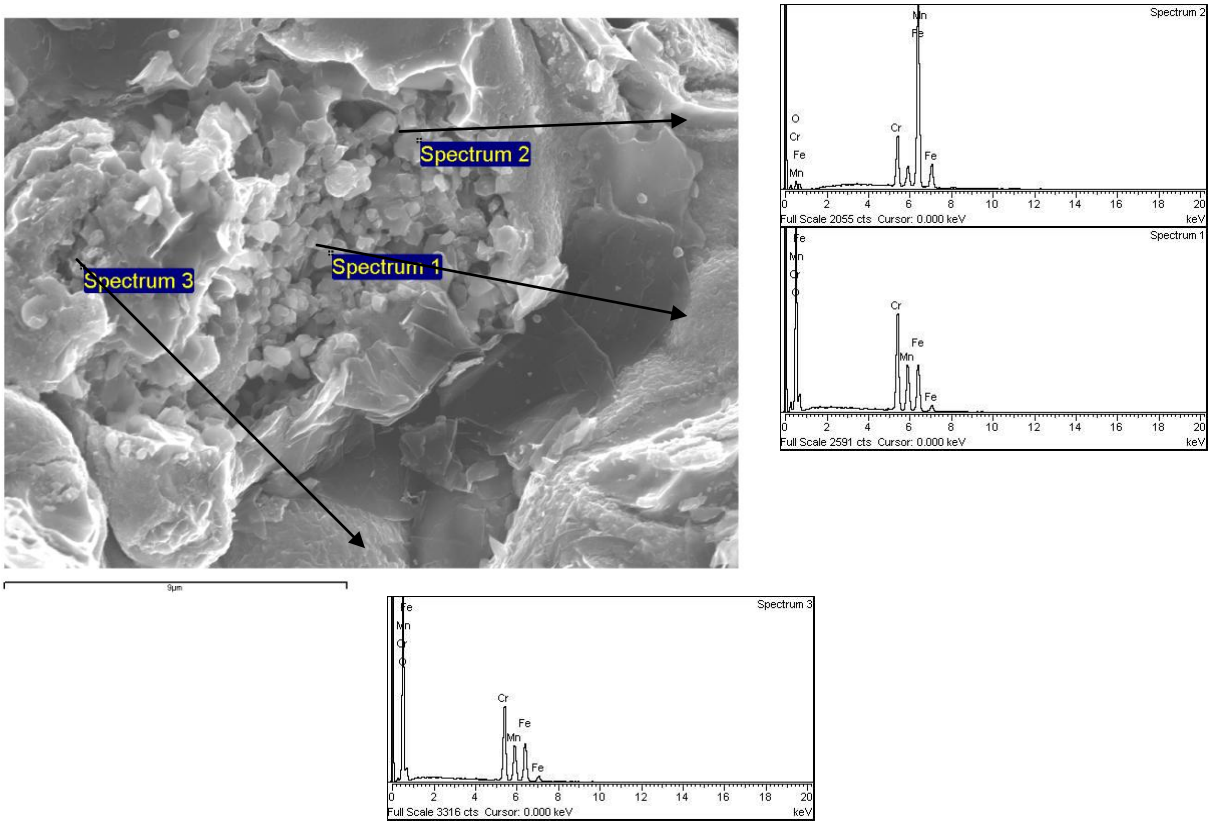

With Oxygen						Without Oxygen				
Spectrum	O	Cr	Mn	Fe	Total	Spectrum	Cr	Mn	Fe	Total
Spectrum 1	52.63	21.33	10.35	15.70	100.00	Spectrum 1	44.82	21.78	33.40	100.00
Spectrum 2	4.08	13.55	5.87	76.51	100.00	Spectrum 2	14.11	6.12	79.76	100.00
Spectrum 3	57.67	18.79	9.19	14.34	100.00	Spectrum 3	44.16	21.65	34.20	100.00

FIGURE 27. SEM + EDX ANALYSIS OF A800-3.

Occasionally, both spherical and irregular inclusions can be found as well, with size below 0.5µm. The chemical composition obtained by SEM + EDX analysis is similar to the chemical composition of the particulate features: complex refractory oxides where chromium and manganese are dominant. (See figure 28 and Appendix II)

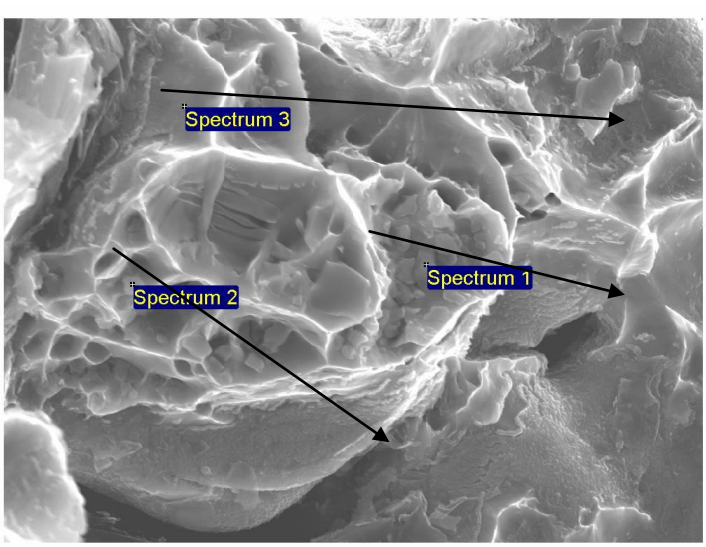

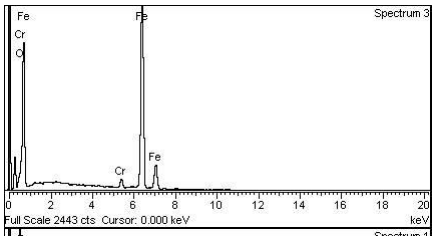

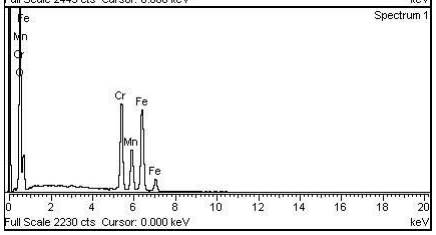

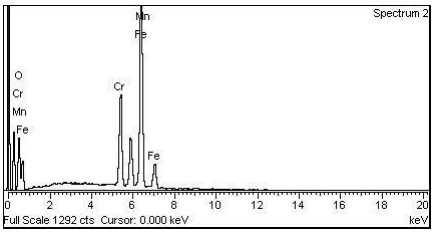

With Oxygen						Without Oxygen				
Spectrum	O	Cr	Mn	Fe	Total	Spectrum	Cr	Mn	Fe	Total
Spectrum 1	49.13	16.81	8.44	25.62	100.00	Spectrum 1	32.85	16.55	50.60	100.00
Spectrum 2	16.70	17.83	10.12	55.35	100.00	Spectrum 2	21.37	12.14	66.48	100.00
Spectrum 3	5.63	2.59	0,00	91.78	100.00	Spectrum 3	2.75	0,00	97.25	100.00

FIGURE 28. SEM + EDX ANALYSIS OF A800-3.

A900-3

Fig. 29 (A and B) presents the as polished states of A900-3: internal oxides uniformly distributed, big irregular pores and particle boundaries are visible. Rounded pores can be found as well.

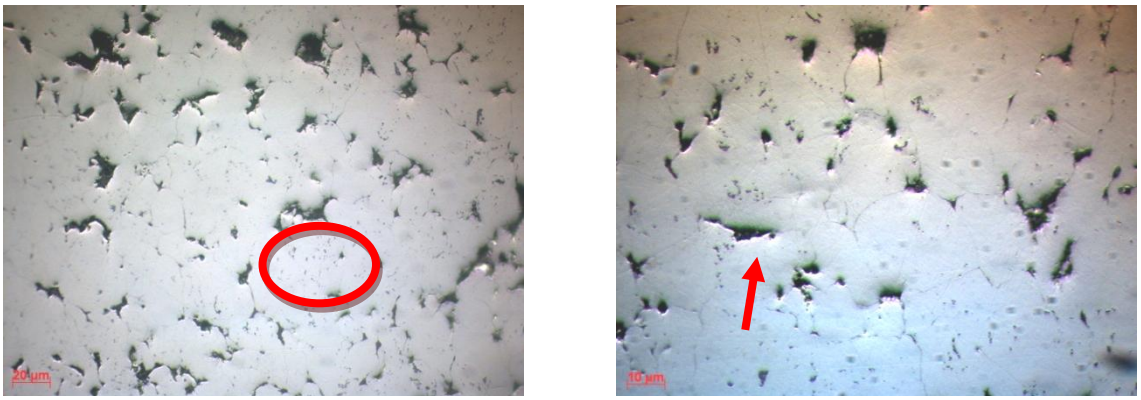

500x 1000x

FIGURE 29. MICROSTRUCTURE OF A900-3 IN AS-POLISHED STATE.

The etched microstructures presented in figure 30 (A and B) correspond to A900-3. The microstructure is heterogeneous, made up of ferrite and pearlite. Although ferrite is the abundant phase, the relative amount of pearlite increases from A800 (~10%) and it is found close to the particle boundaries.

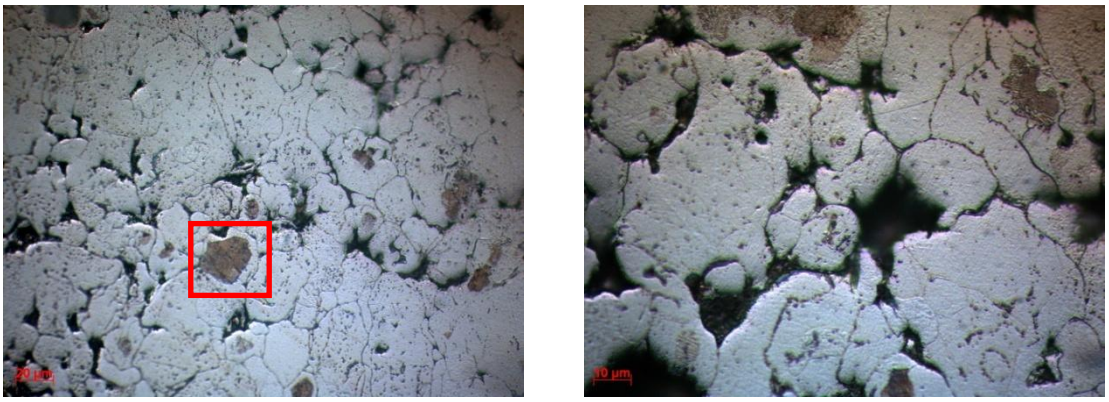

500x 1000x

FIGURE 30. MICROSTRUCTURE OF A900-3 ETCHED.

From the investigation of the fracture surface it was seen that the fracture surface is rough and both individual particles and their agglomerates still can be distinguished. (See fig. 31)

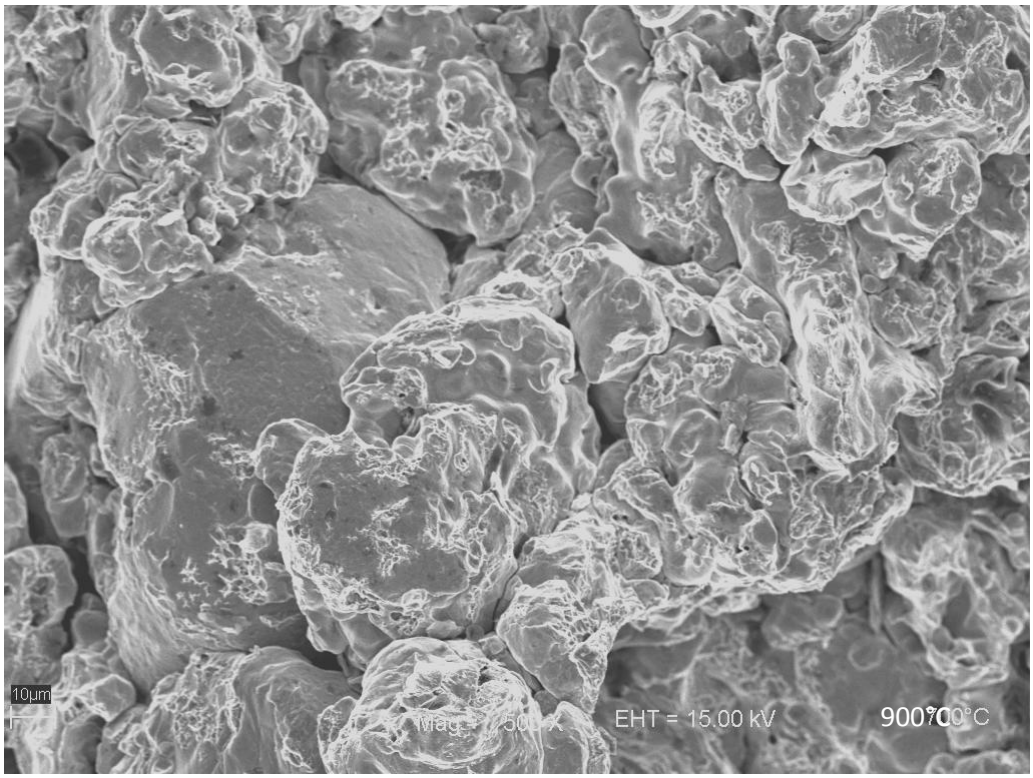

FIGURE 31. OVERVIEW OF THE FRACTURE SURFACE OF A900-3 AT 500X.

The surface of the base powder particle looks “purer” for A900-3 than for specimens sintered at lower temperatures. Inter-particle point, branched and dimple ductile fracture is the main failure micro-mechanism for A900-3.

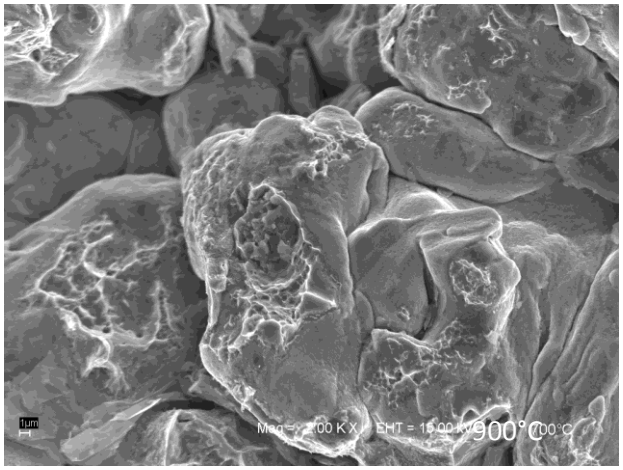

FIGURE 32. FRACTURE SURFACE OF A900-3 AT 2000X.

Inter-particle connections are more developed in comparison with specimens sintered at lower temperatures especially close to the specimen surface. (See fig. 33 and Appendix I)

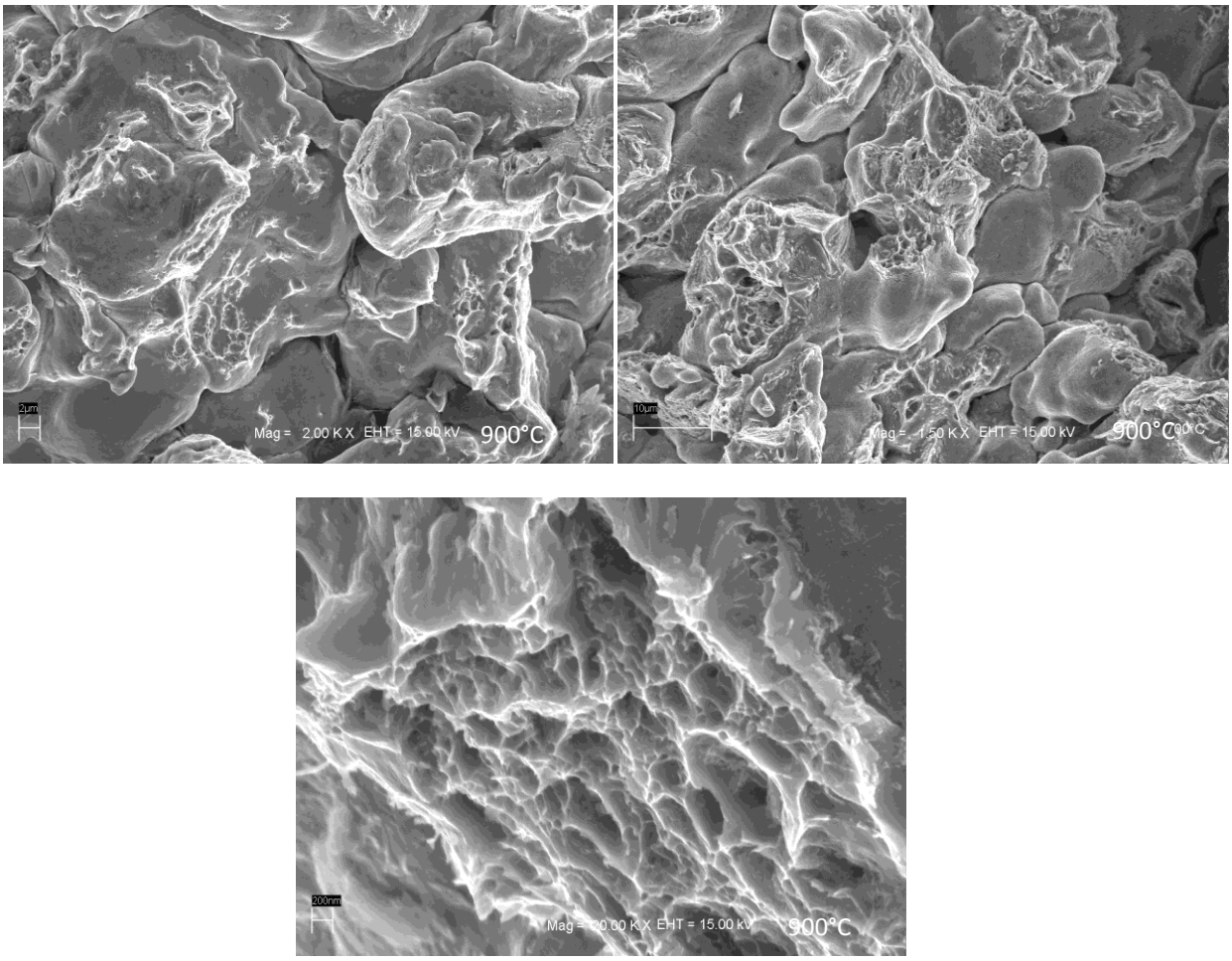

FIGURE 33. DIFFERENCES BETWEEN INNER PART AND EDGES OF A900-3.

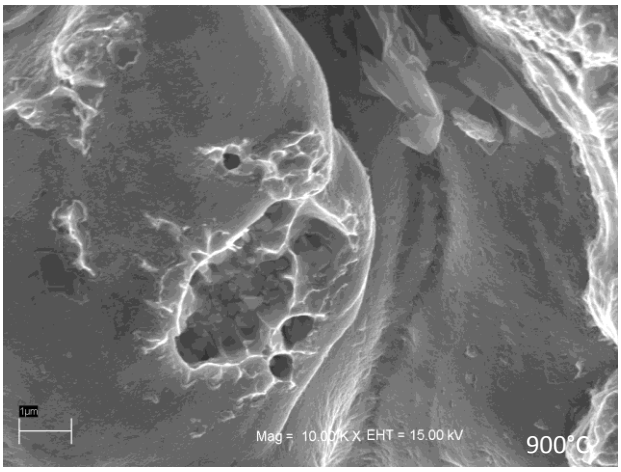

FIGURE 34. PARTICULATE FEATURES IN A900-3.

Higher amount of the inclusions inside dimples of inter-particle ductile fracture is characteristic for this specimen. Analysis these particulates at higher magnification shows, they have irregular shape and size up to 1 µm. SEM combined with EDX analysis indicate increase in manganese and chromium content and compared to A800-3 and A700-3. See Figures 34 and 35 and Appendix I.

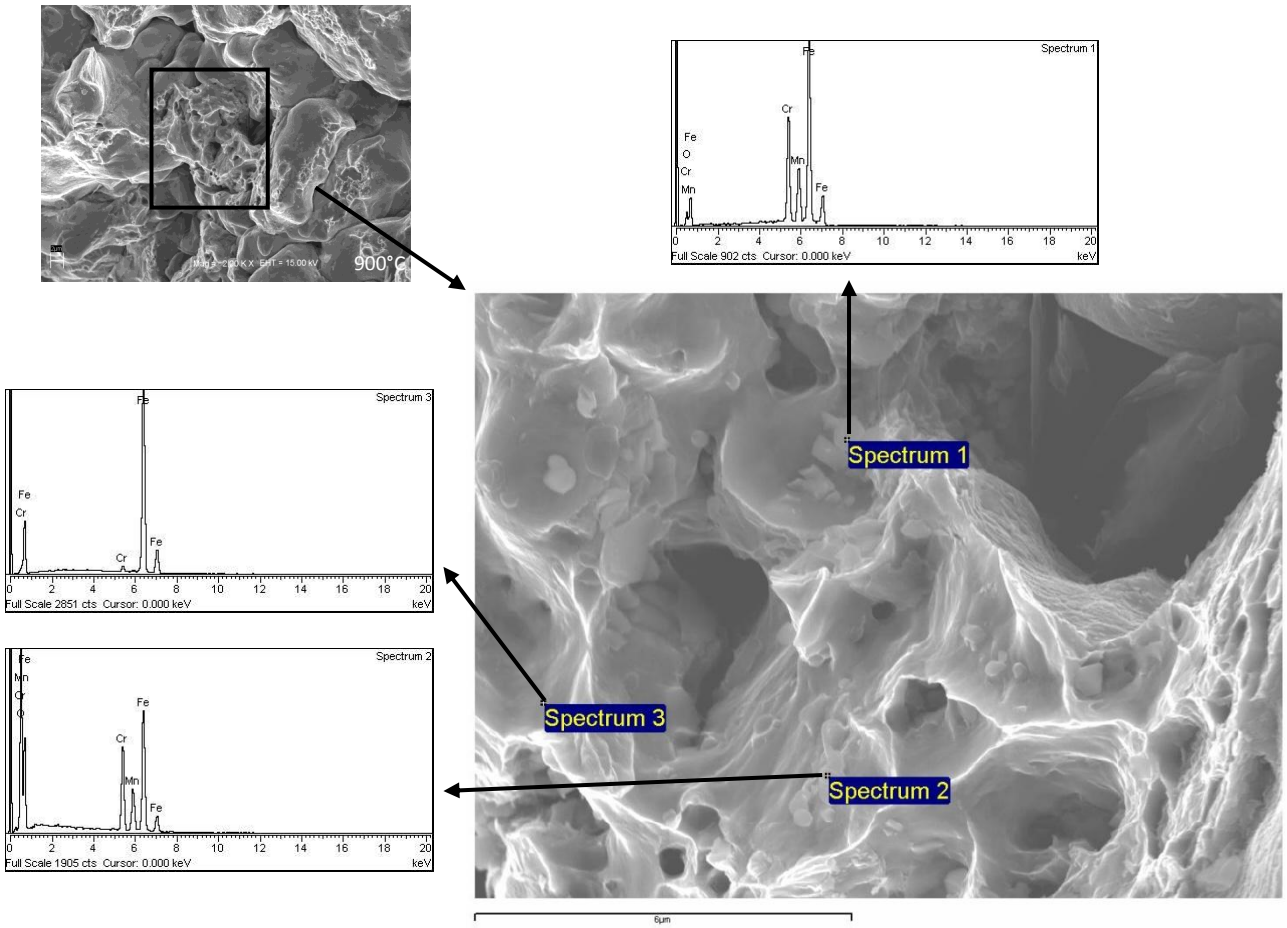

With oxygen						Without oxygen				
Spectrum	O	Cr	Mn	Fe	Total	Spectrum	Cr	Mn	Fe	Total
Spectrum 1	3.65	22.29	12.69	61.37	100.00	Spectrum 1	23.13	13.17	63.70	100.00
Spectrum 2	42.58	15.51	7.60	34.32	100.00	Spectrum 2	26.86	13.21	59.93	100.00
Spectrum 3	0,00	1.64	0,00	98.36	100.00	Spectrum 3	1.64	0,00	98.36	100.00

FIGURE 35. SEM + EDX ANALYSIS IN A900-3.

According to the microstructure observation, areas where failure of the pearlitic structures took place are occasionally visible on the fracture surface.

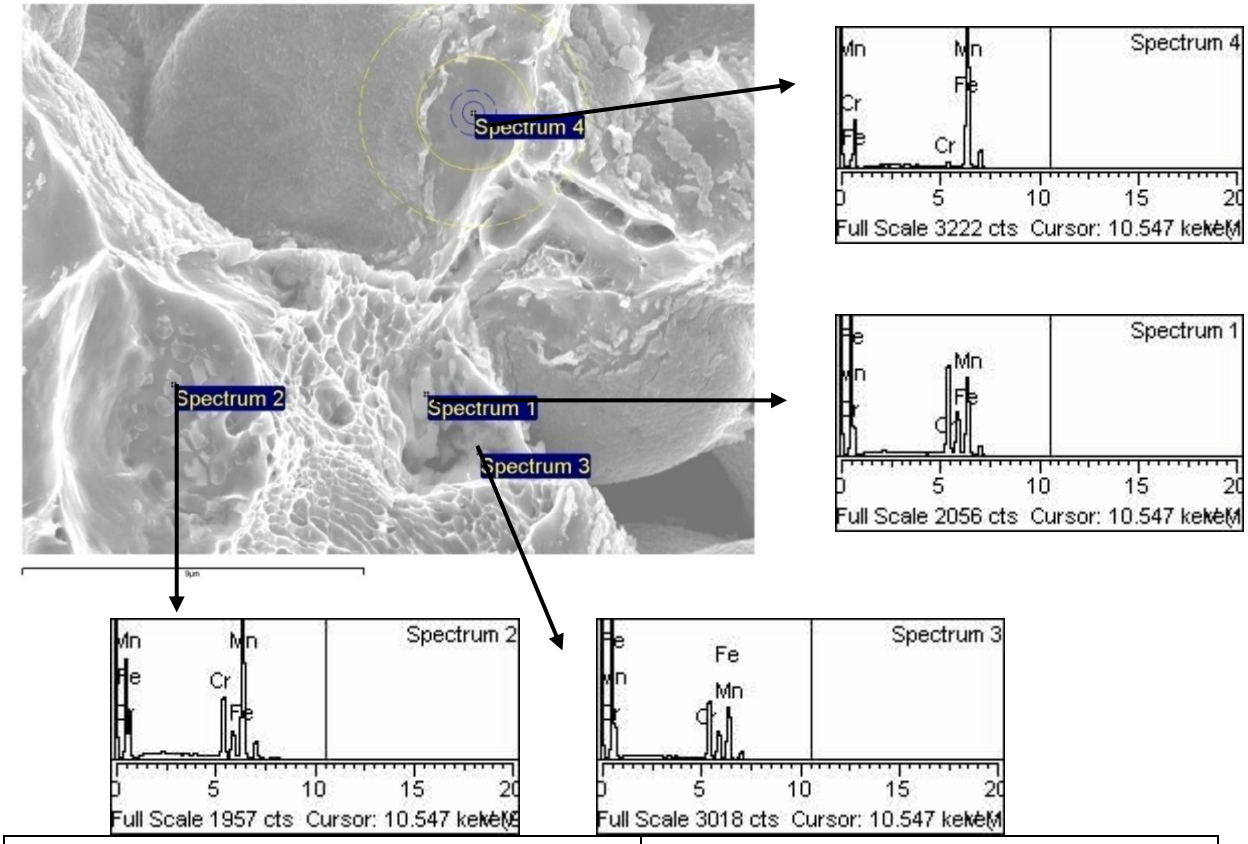

With oxygen						Without oxygen				
Spectrum	O	Cr	Mn	Fe	Total	Spectrum	Cr	Mn	Fe	Total
Spectrum 1	40.61	21.38	10.42	27.60	100.00	Spectrum 1	35.85	17.51	46.65	100.00
Spectrum 2	30.74	13.36	6.50	49.40	100.00	Spectrum 2	19.22	9.38	71.41	100.00
Spectrum 3	48.37	17.49	8.71	25.42	100.00	Spectrum 3	33.70	16.84	49.46	100.00
Spectrum 4	3.88	1.60	0.00	94.52	100.00	Spectrum 4	1.66	0.00	98.34	100.00

FIGURE 36. SEM + EDX ANALYSIS IN A900-3.

A1000-3

The presented as-polished microstructures of specimens sintered at 1000°C clearly indicate presence of oxides inside the powder particle (see figure 37). The same irregulary-shaped pores but slightly more rounded in comparison with other specimens previously analyzed are observed. Small spherical ones can be visible as well.

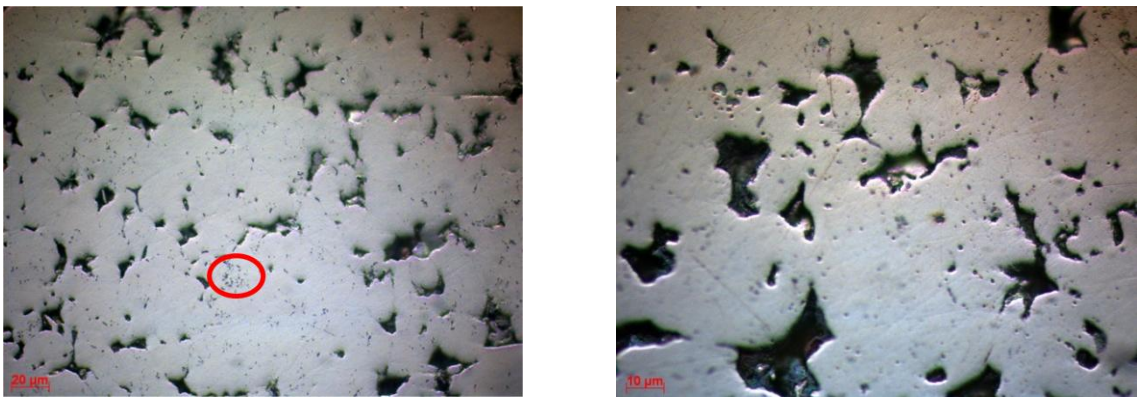

500x 1000x

FIGURE 37. MICROSTRUCTURES OF A1000-3 IN AS-POLISHED STATE.

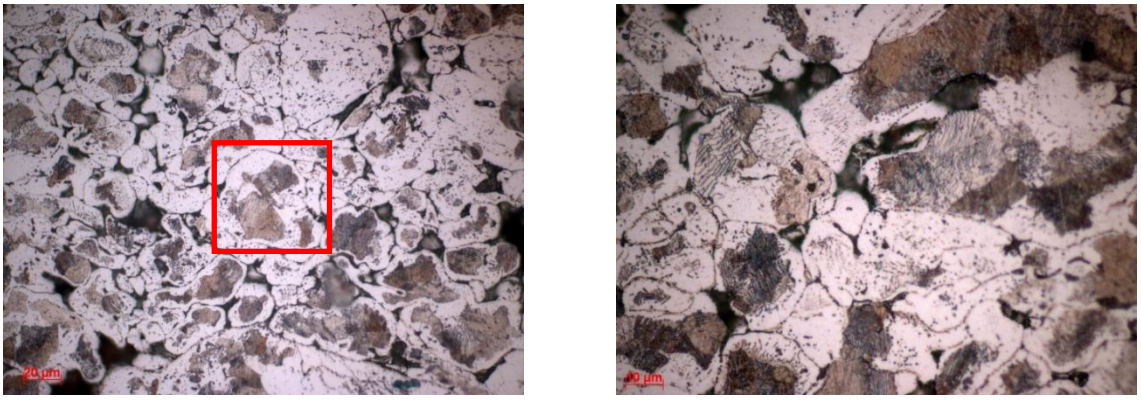

500x 1000x

FIGURE 38. MICROSTRUCTURES OF A1000-3 IN ETCHED STATE.

Etched microstructure of specimen A1000-3, presented in Fig.38, indicate much higher portion of pearlite as it was observed for A900-3. Relative amount of pearlite found in this specimen reach was below 40%.

The overview of the fracture surface for A1000-3 can be seen in figure 39. The surface is still rough. There is evidence of inter-particle dimple ductile fracture, initiated by particulate features, bridge porosity and cementitic lamellae (see Appendix I).

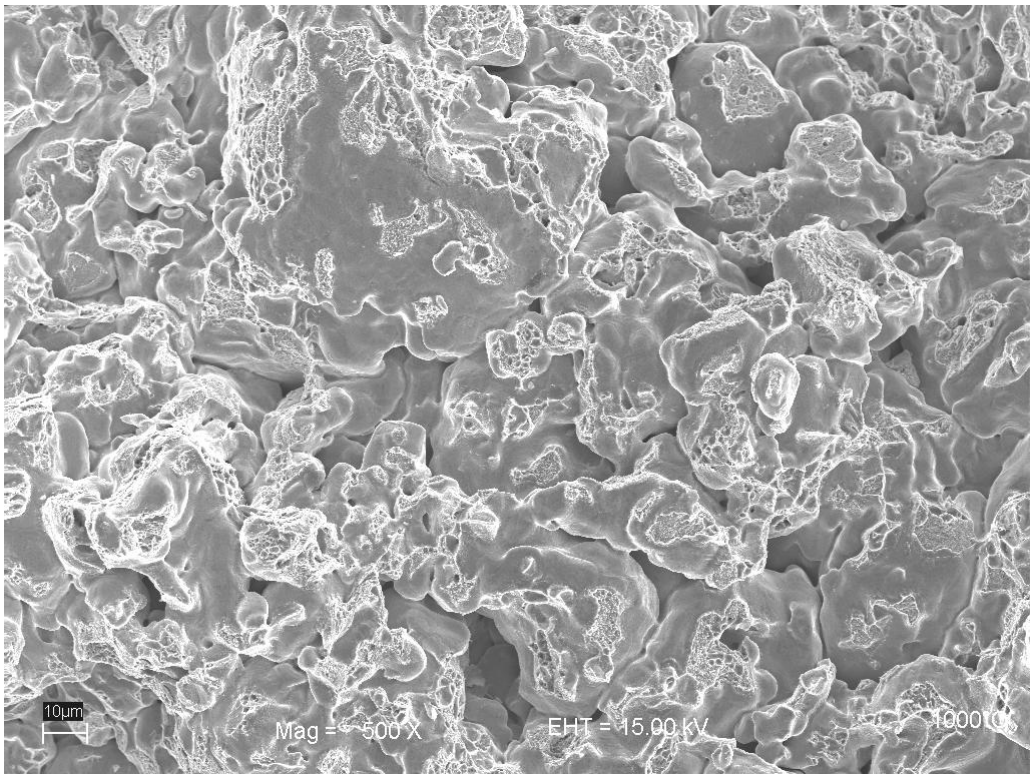

FIGURE 39. FRACTURE SURFACE OVERVIEW OF A1000-3.

Surface of the initial powder particles is “pure”, indicating full reduction of the surface oxides. Fine particulate features still can rarely observed on the free particles surface, however their size is below 0.5 µm. (See fig. 40 and Appendix I).

Inter-particle necks formation is developed for A1000-3, especially close to the specimen surface.

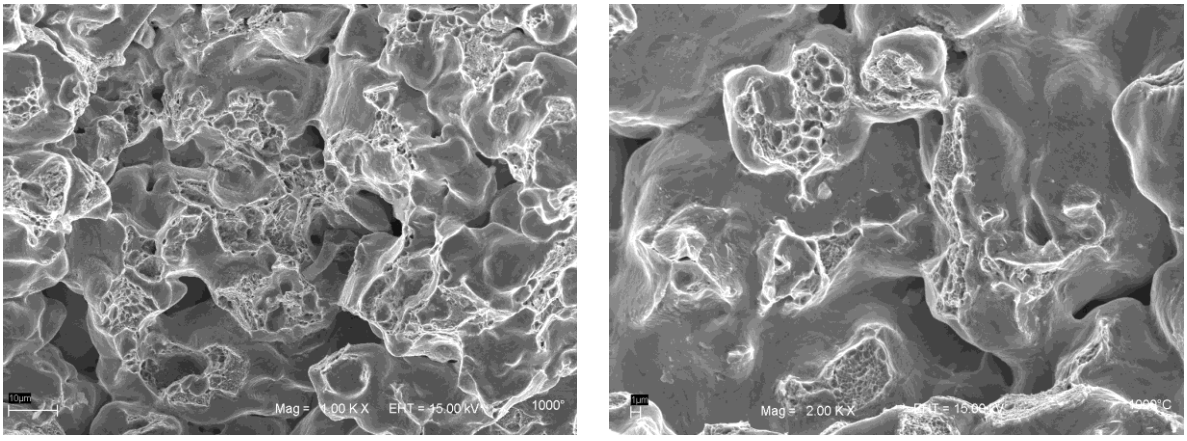

FIGURE 40. DETAIL OF THE FRACTURE SURFACE OF A1000-3.

Inclusions inside the inter-particle necks reach a size up to 1 µm and have mostly a spherical shape, but also irregular ones were found. Close to the specimen surface, bigger (up to 2 µm) and more regularly shaped inclusions inside inter-particle necks were registered. According to the microstructure observation, ductile failure of pearlitic structures is often visible on the fracture surface and inclusions can be found inside lamellae as well. (See Fig.41 and Appendix I).

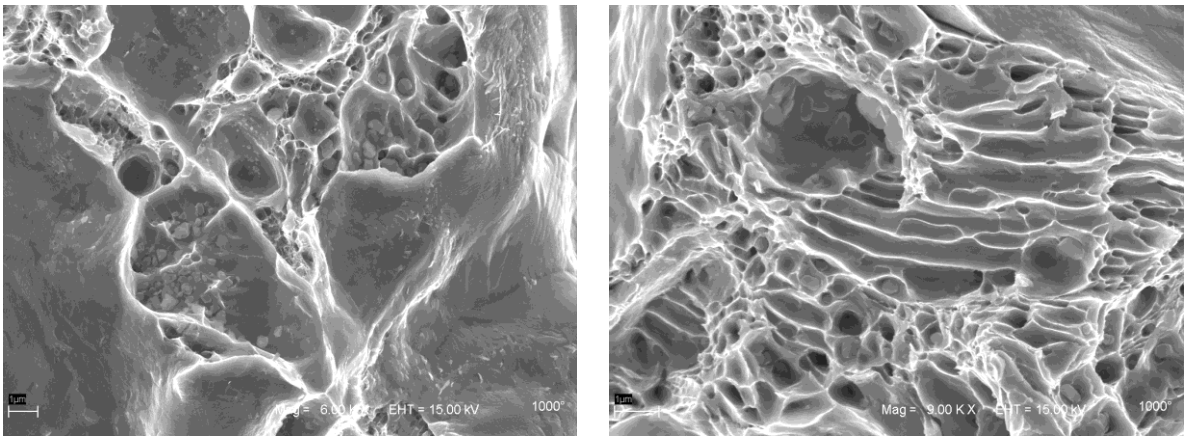

FIGURE 41. MAIN FAILURE MECHANISM FOR DUCTILE FRACTURE IN A1000-3.

As in the previous cases, SEM + EDX analysis indicate that studied inclusions are reach in manganese and chromium, see fig. 42 and Appendix I.

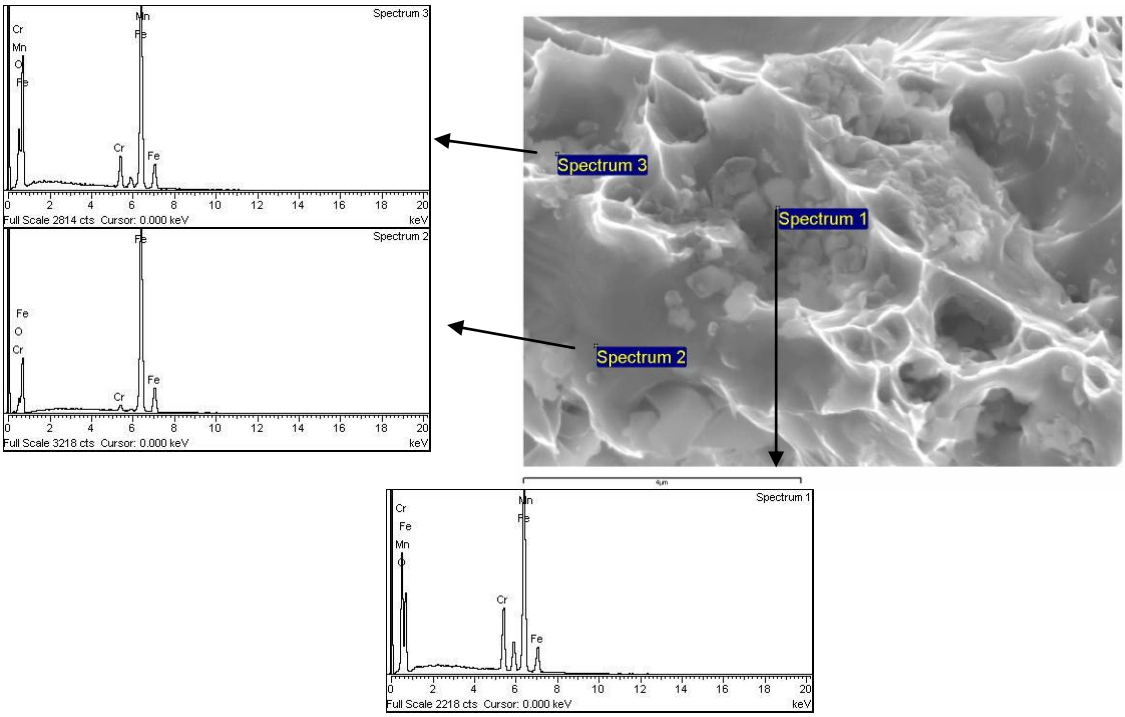

Oxygen						No Oxygen				
Spectrum	O	Cr	Mn	Fe	Total	Spectrum	Cr	Mn	Fe	Total
Spectrum 1	1.28	13.40	7.54	77.79	100.00	Spectrum 1	13.57	7.63	78.80	100.00
Spectrum 2	9.16	2.81		88.03	100.00	Spectrum 2	3.09		96.91	100.00

FIGURE 42. SEM + EDX ANALYSIS IN A1000-3.

Figure 43 shows a SEM + EDX analysis performed in A1000-3:

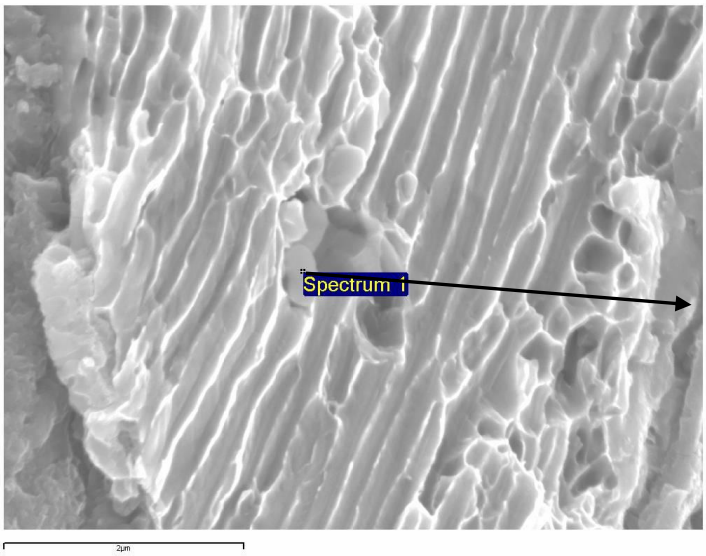

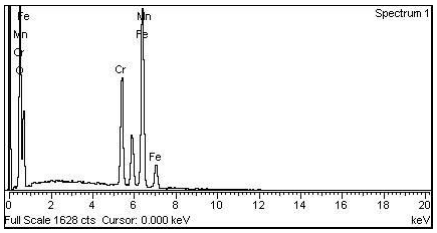

With Oxygen						With Oxygen				
Spectrum	O	Cr	Mn	Fe	Total	Spectrum	Cr	Mn	Fe	Total
Spectrum 1	38.34	14.69	7.80	39.16	100.00	Spectrum 1	23.72	12.64	63.64	100.00

FIGURE 43. SEM + EDX ANALYSIS IN A1000-3.

A1120-3

In figure 44 A and B are presented the microstructures of A1120-3 in as-polished state. Although big pores have similar sizes in comparison with other specimens, they are more rounded. Smaller rounded pores are also present.

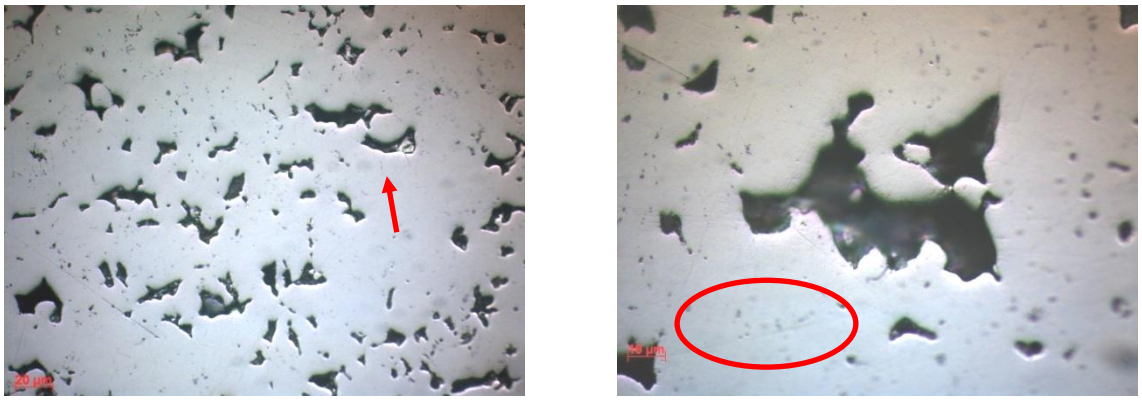

500x 1000x

FIGURE 44. MICROSTRUCTURES OF A1120-3 IN AS POLISHED STATE.

Picture 45 (A and B) show the etched microstructure of A1120-3. It shows higher portion of pearlite as it was observed for other sintering temperatures (~90%).

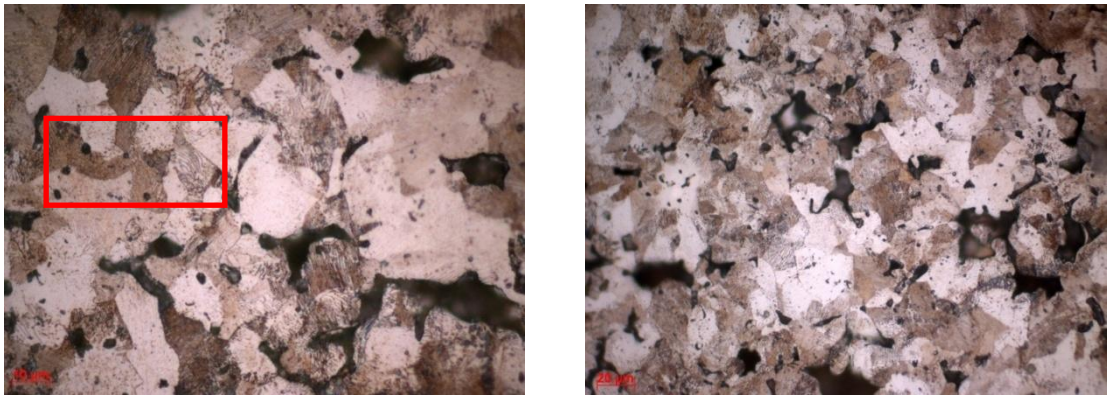

1000x 500x

FIGURE 45. MICROSTRUCTURE OF A1120-3 IN ETCHED STATE.

Investigations of the fracture surfaces A1120-3 after simple impact test, illustrates the roughness of the surface. No individual particles can be identified. The main failure mechanism for inter-particle ductile fracture is bridge porosity and cementitic lamellae (See fig. 46 and Appendix I).

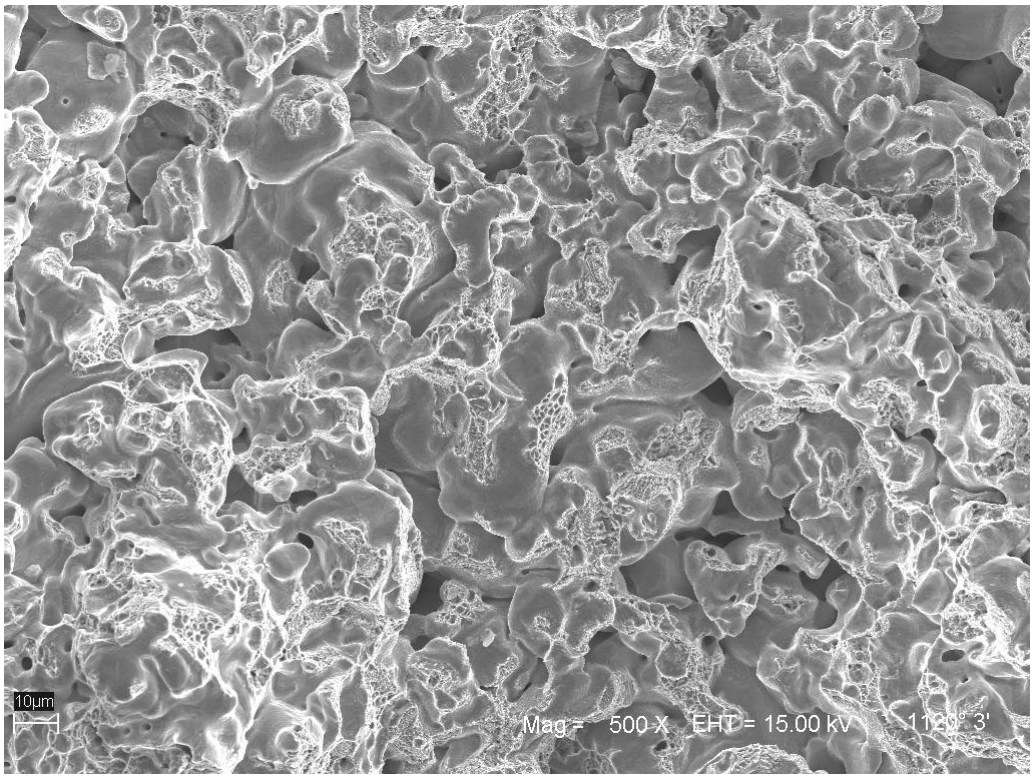

FIGURE 46. OVERVIEW OF THE FRACTURE SURFACE OF A1120-3 AT 500X.

The surface of the initial powder particles is "pure" what indicates full reduction of the surface oxide layer. Moreover, fine particulate features still can rarely be observed on the free particles surface. Their size is below 0.5 µm, this implies that they were reduced in comparison with previous specimens. Inter-particle necks formation is strongly developed for A1000-3. See fig. 47 and Appendix I.

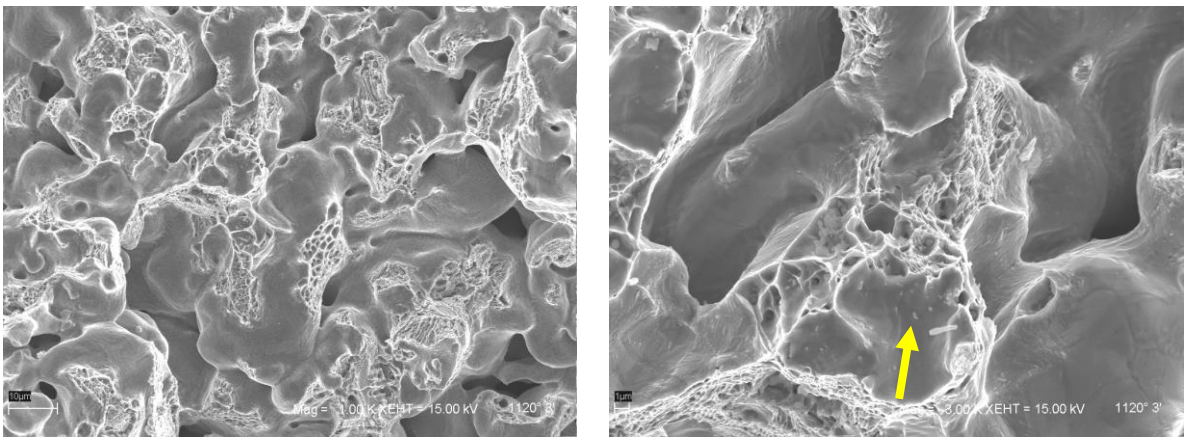

FIGURE 47. INTER-PARTICLE NECKS DEVELOPMENT IN A1120-3.

Inclusions inside dimples (closed porosity) on the inter-particle necks reach a size up to 1 µm and are irregularly shaped. Close to the specimen surface, bigger (up to 2 µm) and more spherical shaped inclusions inside inter-particle necks were found. The portion of inclusions has increased in comparison to other specimens.

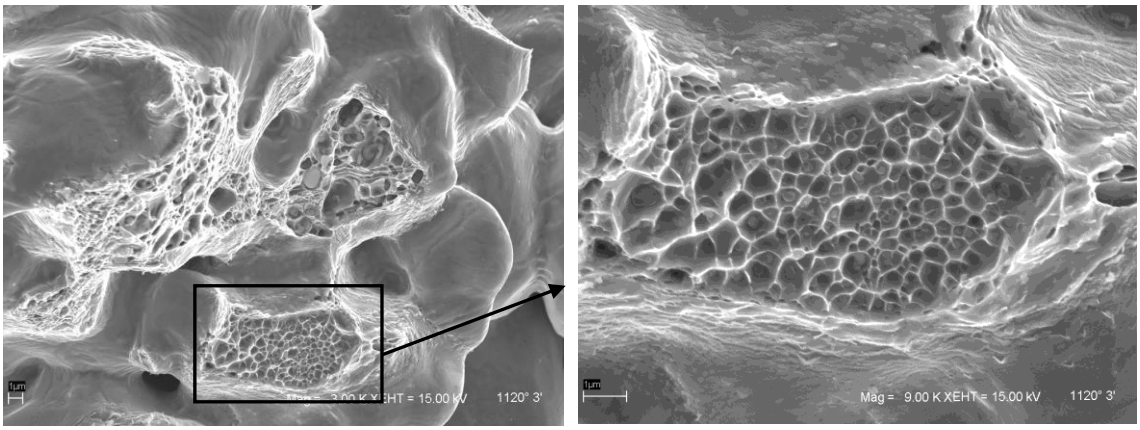

FIGURE 48. DIMPLES IN A1120-3.

In some cases, inclusions inside dimples start to be connected, which can lead to the formation of agglomerates of inclusions.

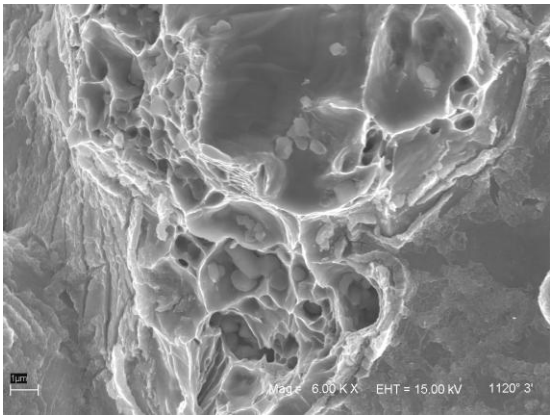

FIGURE 49. INCLUSIONS IN A1120-3.

As in the previous cases, SEM + EDX analysis indicate that studied inclusions are rich in manganese and chromium (see Figure 50 and Appendix II). As was said, it "seems" that the manganese and chromium content has increased when compared with specimens sintered at lower temperatures, but because of the accuracy of the method no safe conclusions can be drawn.

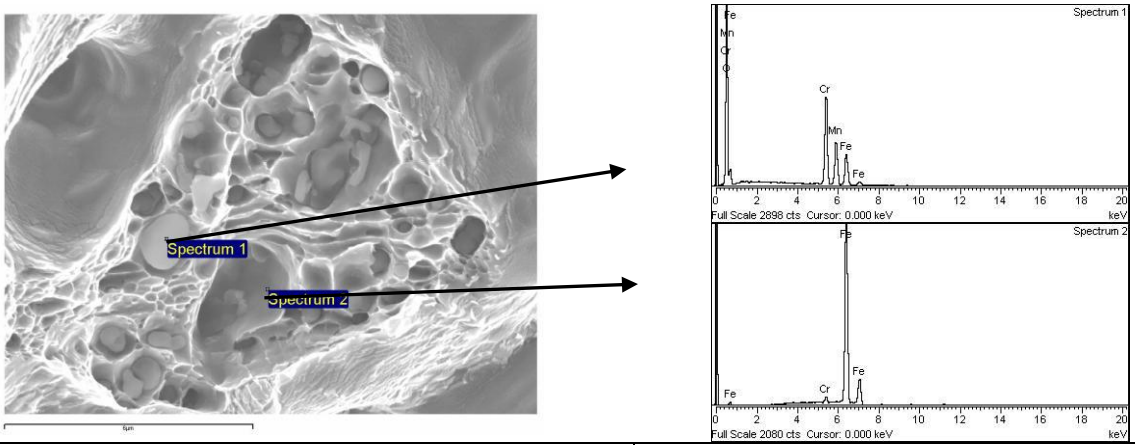

With Oxygen						Without oxygen				
Spectrum	O	Cr	Mn	Fe	Total	Spectrum	Cr	Mn	Fe	Total
Spectrum 1	27.59	34.85	18.21	19.35	100.00	Spectrum 1	47.95	25.02	27.04	100.00
Spectrum 2	0.15	1.59	0.00	98.26	100.00	Spectrum 2	1.60	0.00	98.40	100.00

FIGURE 50. SEM + EDX ANALYSIS IN A1120-3.

According to the fractographic investigation, ductile failure of pearlitic structures is often visible on the fracture surface (See fig. 51 and Appendix I).

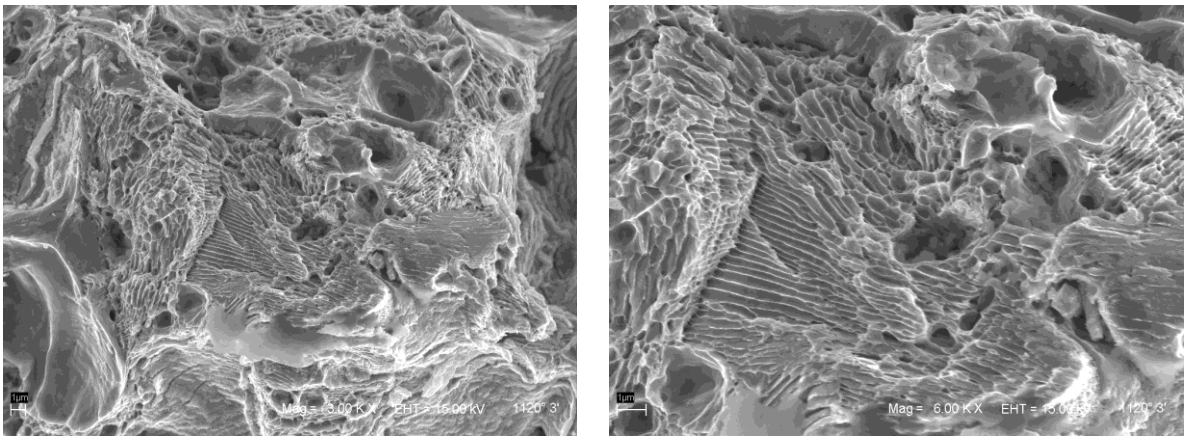

FIGURE 51. PERLITE IN A1120-3.

A1120- 15

The microstructures of A1120-15 in as-polished state are presented in figure 52 (A and B). Pores have rounded regular shapes. Internal oxides are also visible.

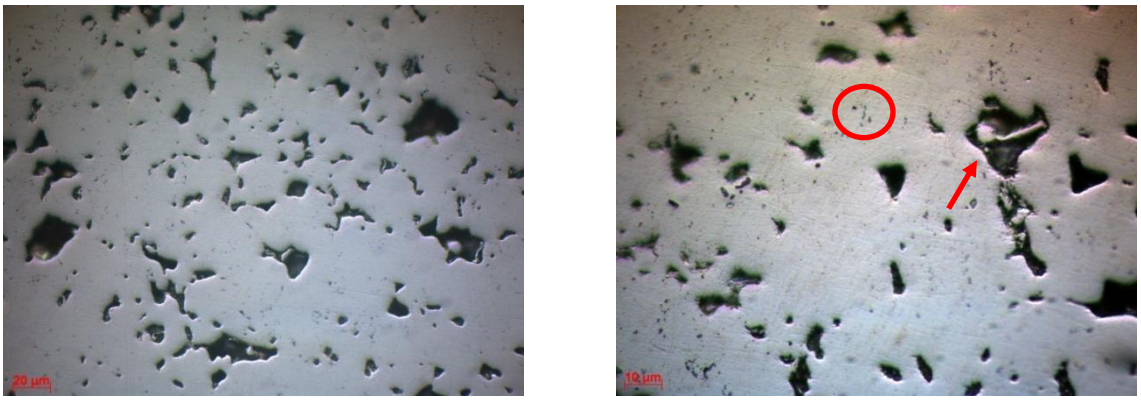

500x 1000x

FIGURE 52. MICROSTRUCTURE OF A1120-15 IN AS-POLISHED STATE.

Picture 53 (A and B) show the etched microstructure of A1120-3. It shows approximately the same portion of pearlite as it was observed for A1120-3 (~90%).

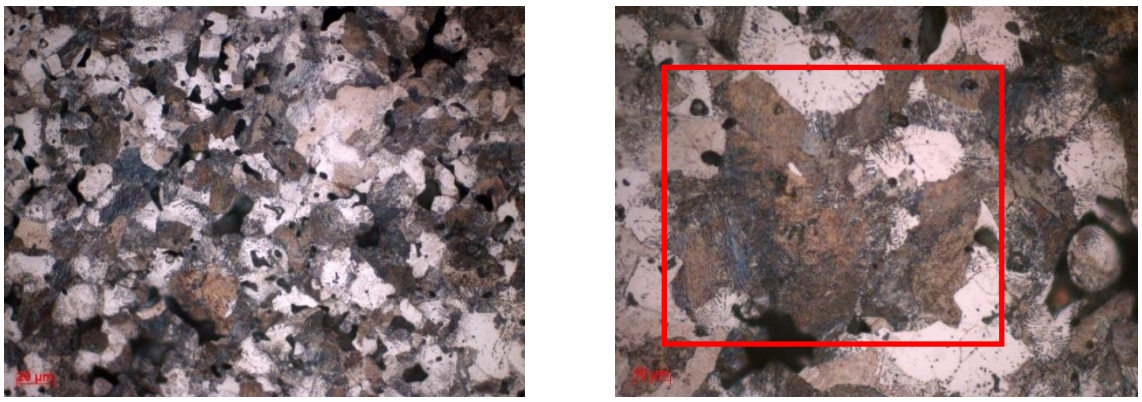

500x 1000x

FIGURE 53. MICROSTRUCTURE OF A1120-15 IN ETCHED STATE.

The fracture surface of A1120-15 was studied after simple impact test. It is rough, and no individual particles can be distinguished (See fig. 54).

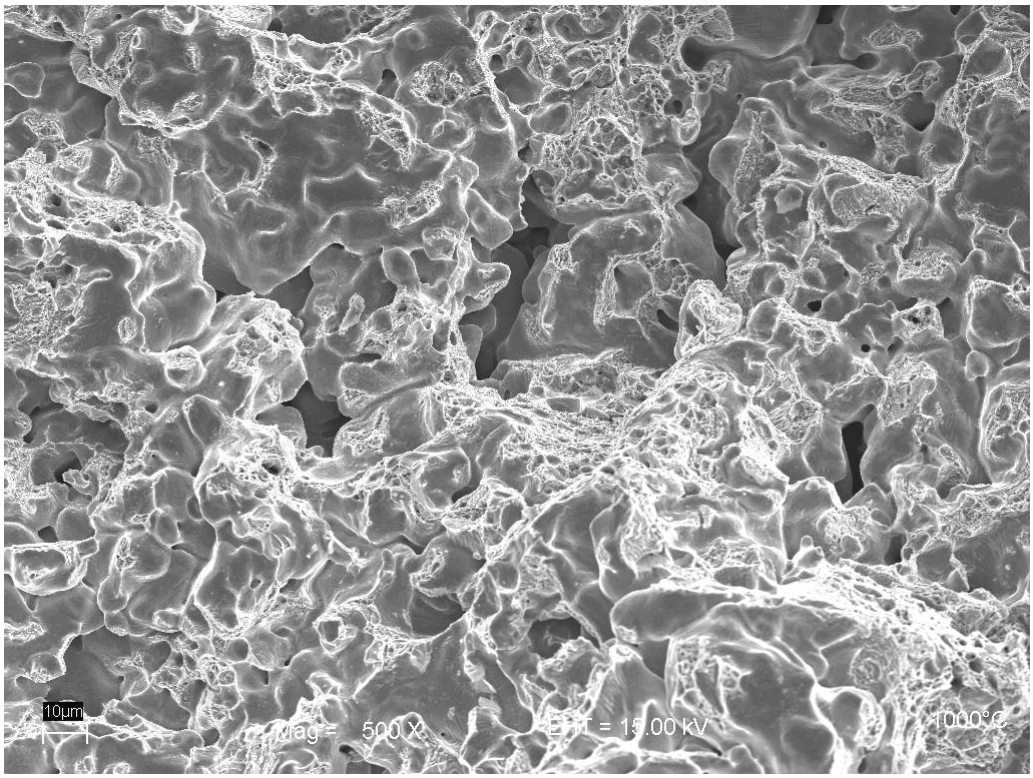

FIGURE 54. OVERVIEW OF THE FRACTURE SURFACE OF A1120-15 AT 500X.

Inter-particle connections are more developed in comparison with A1120-3. In some areas, there is some evidence of re-oxidation after cooling, because surface not as "pure" as for A1000-3 or A900-3. (See fig. 55 and also Appendix 1).

Like for A1000 and A1120-3, fine particulate features still can rarely be observed on the free particles surface that size up to 0.5 µm.

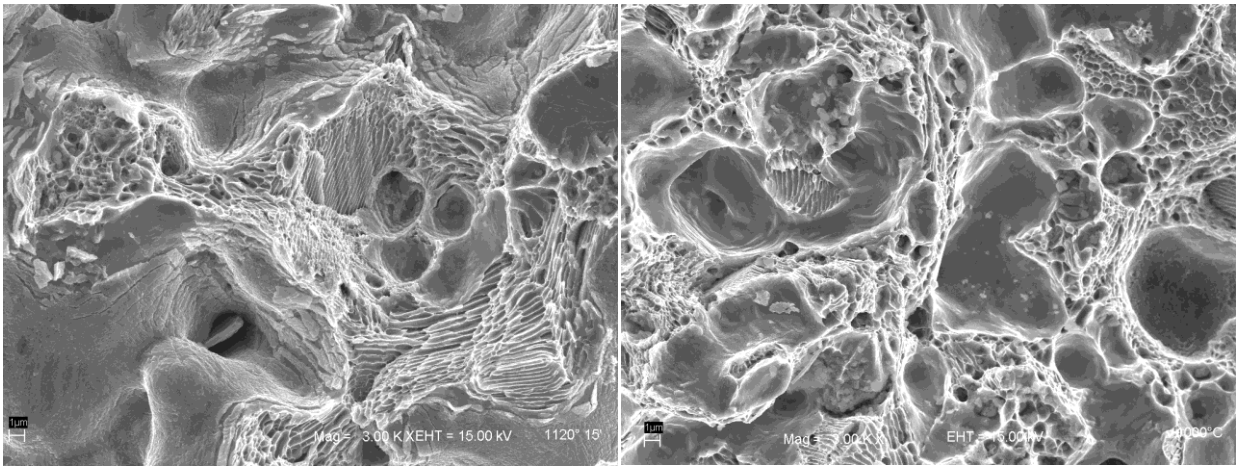

FIGURE 55. INTER-PARTICLE CONNECTIONS IN A1120-15.

The main failure mechanism for inter-particle ductile fracture is bridge porosity and ductile failure of pearlitic structures. In agreement with the microstructure investigation, ductile failure of pearlitic structures is frequently visible on the fracture surface. It is also common to see inclusions inside them (See fig. 56, 57 and also Appendix I).

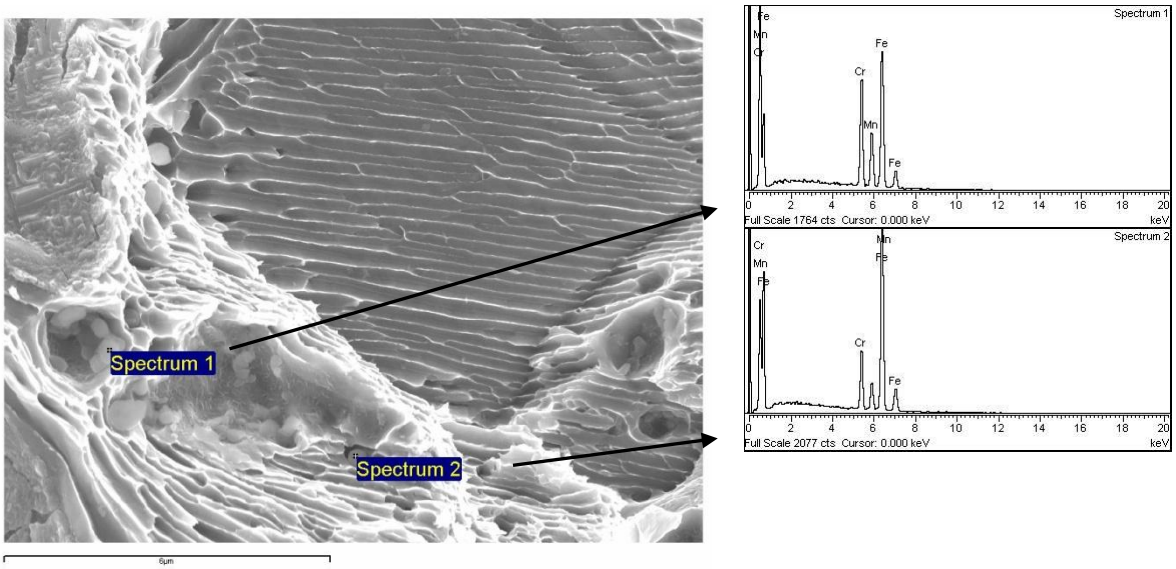

With oxygen					
Spectrum	O	Cr	Mn	Fe	Total
Spectrum 1	16.84	21.86	13.23	48.07	100.00
Spectrum 2	11.85	12.61	6.66	68.88	100.00

Without oxygen				
Spectrum	Cr	Mn	Fe	Total
Spectrum 1	26.21	15.86	57.93	100.00
Spectrum 2	14.28	7.53	78.19	100.00

FIGURE 56. SEM + EDX ANALYSIS IN A1120-15.

There are more inclusions in A1120-15 when compared with other specimens previously analyzed. As for A1120-3, it is common to find irregularly shaped inclusions inside dimples on the inter-particle necks that size up to 1 µm. Close to the specimen surface, bigger (up to 2 µm) and more spherical shaped inclusions on inter-particle necks were found.

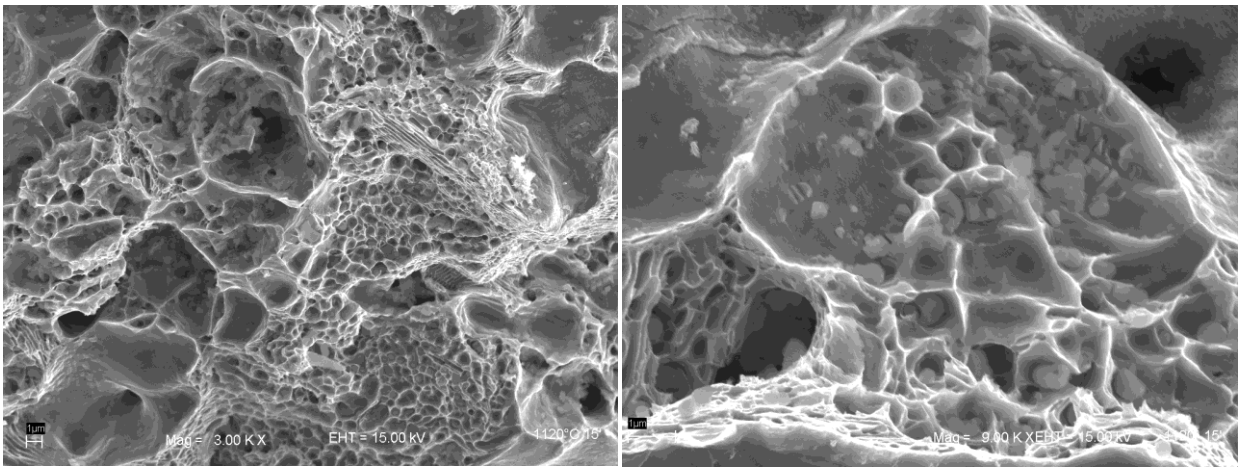

FIGURE 57. INCLUSIONS ON INTER-PARTICLE NECKS IN A1120-15.

SEM combined with EDX analysis indicate that inclusions are complex refractory oxides, rich in manganese and chromium, see Figures 56, 58 and Appendix II.

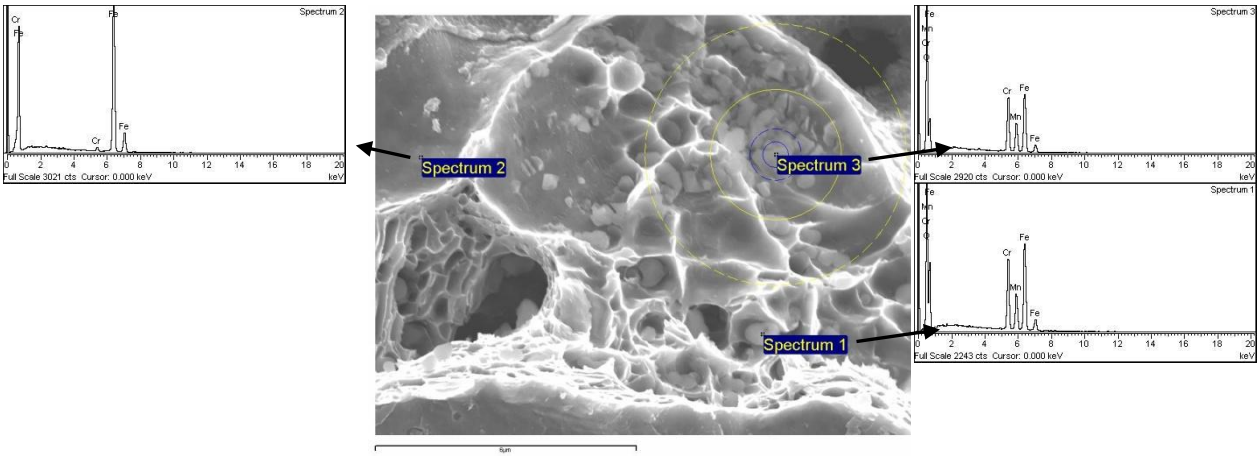

With oxygen					
Spectrum	O	Cr	Mn	Fe	Total
Spectrum 1	19.84	21.58	12.50	46.07	100.00
Spectrum 2	1.92	1.25	0.00	96.83	100.00
Spectrum 3	24.66	22.28	12.75	40.31	100.00

Without oxygen				
Spectrum	Cr	Mn	Fe	Total
Spectrum 1	26.81	15.54	57.65	100.00
Spectrum 2	1.28	0.00	98.72	100.00
Spectrum 3	29.40	16.86	53.74	100.00

FIGURE 58. SEM + EDX ANALYSIS IN A1120-15.

A1120- 30

Figure 59 A and B show the microstructures of A1120-30 in as-polished state. Pores are rounded and the proportion of spherical ones has increased when compared with other specimens previously analyzed. Internal oxides can be seen as well.

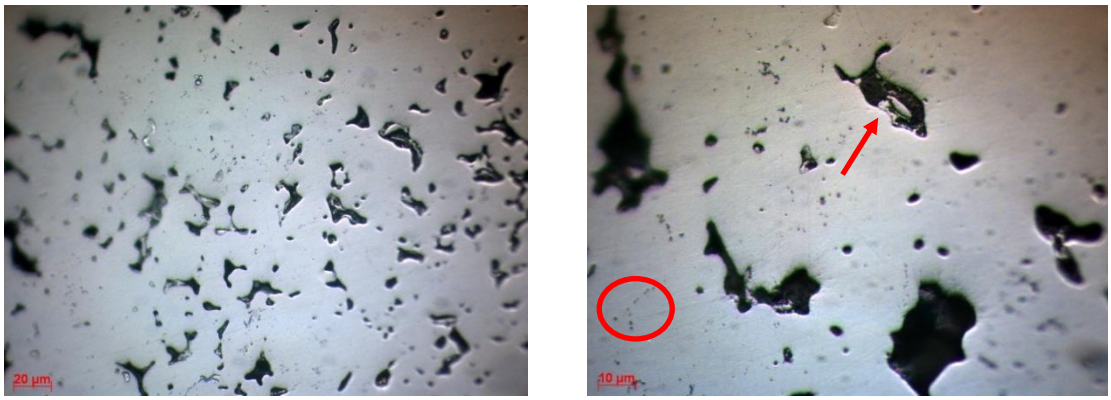

500x 1000x

FIGURE 59. MICROSTRUCTURE OF A1120-30 IN AS-POLISHED STATE.

The etched microstructures of A1120-30 show a pearlitic-ferritic microstructure. The proportion of pearlite found is similar to A1120-3 and A1120-15.

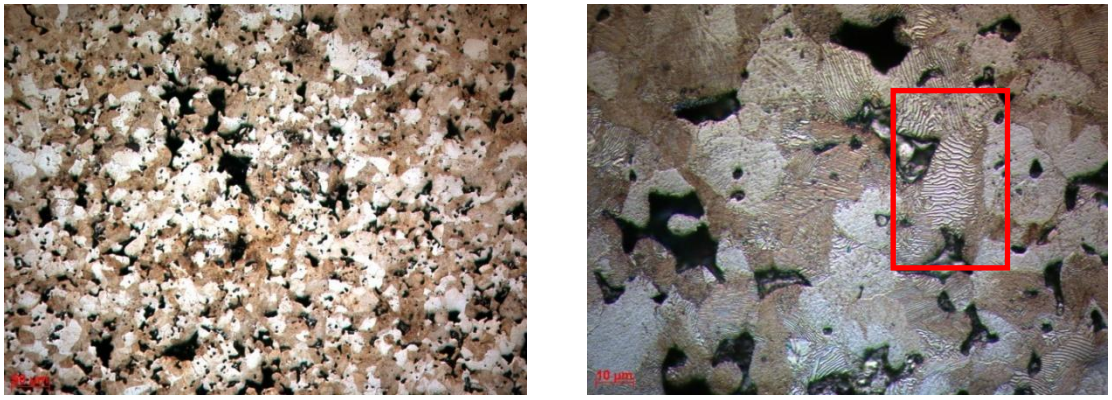

200x 1000x

FIGURE 60. MICROSTRUCTURE OF A11220-30 IN ETCHED STATE.

Figure 61 shows the fracture surface of A1120-30. Inter-particle connections are strongly developed, and therefore it is not possible to distinguished individual particles. The fracture surface is smoother than for other specimens analyzed.

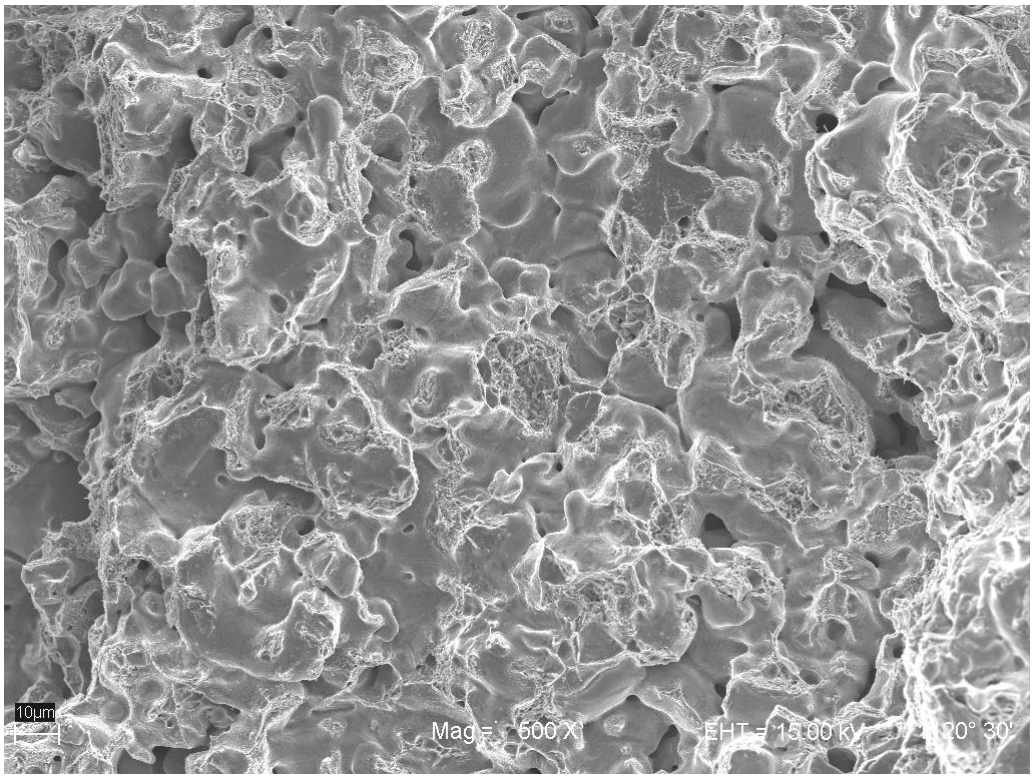

FIGURE 61. OVERVIEW OF THE FRACTURE SURFACE OF A1120-30 AT 500X.

The main failure mechanism for inter-particle ductile fracture is bridge porosity and ductile failure of pearlitic structures (See fig. 62 and also Appendix I).

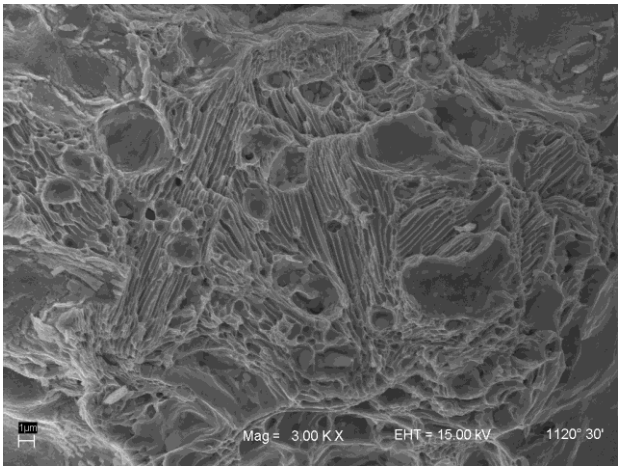

FIGURE 62. PERLITIC STRUCTURES IN A1120-30.

There are more inclusions in A1120-30 when compared with other specimens previously analyzed. Inclusions that were close to the surface, have spherical shape and size up to 1µm. See figure 63 and Appendix I.

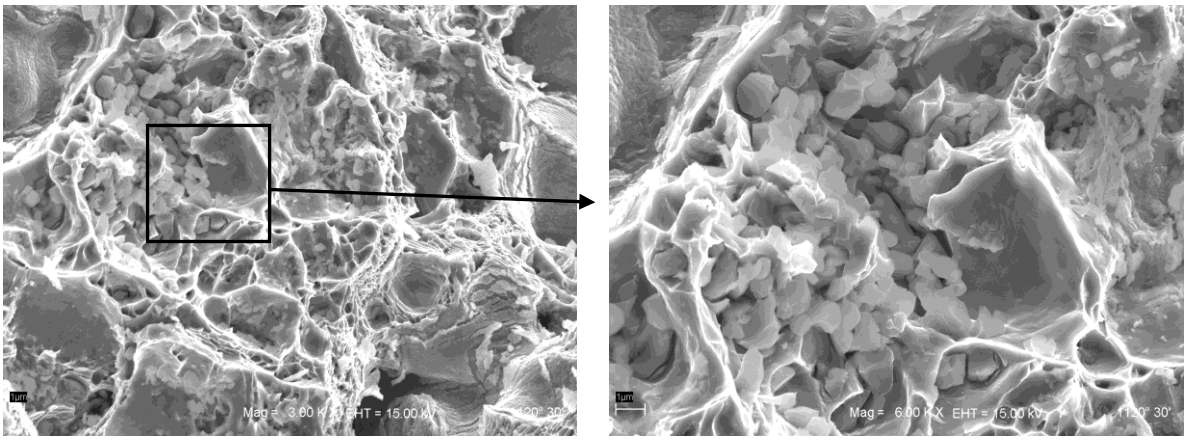

FIGURE 63. INCLUSIONS IN A1120-30.

There are irregularly but rounded shaped inclusions, sized up to 1µm from spherical inclusions that form agglomerations (See figures 64, 65 and 66 and Appendix I).

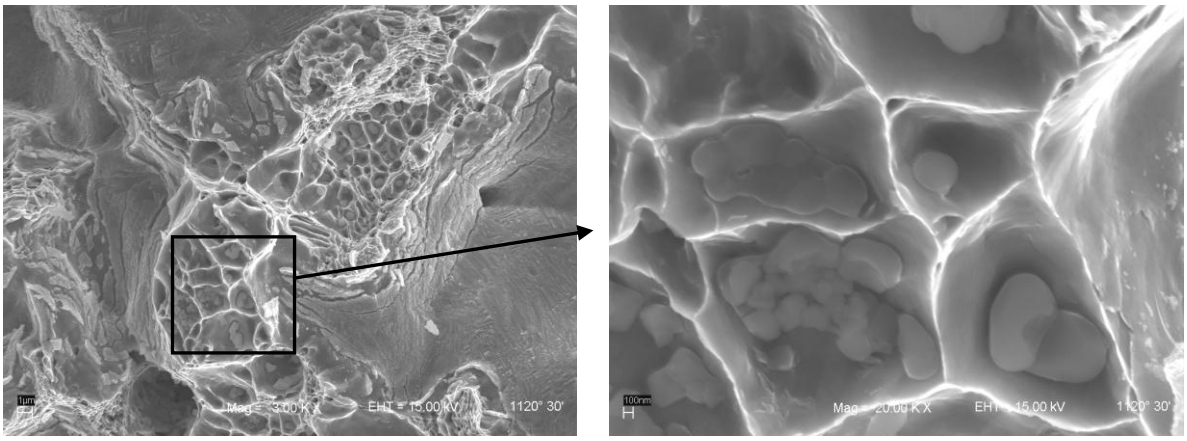

FIGURE 64. IRREGULAR INCLUSIONS IN A1120-30.

SEM + EDX analysis were performed:

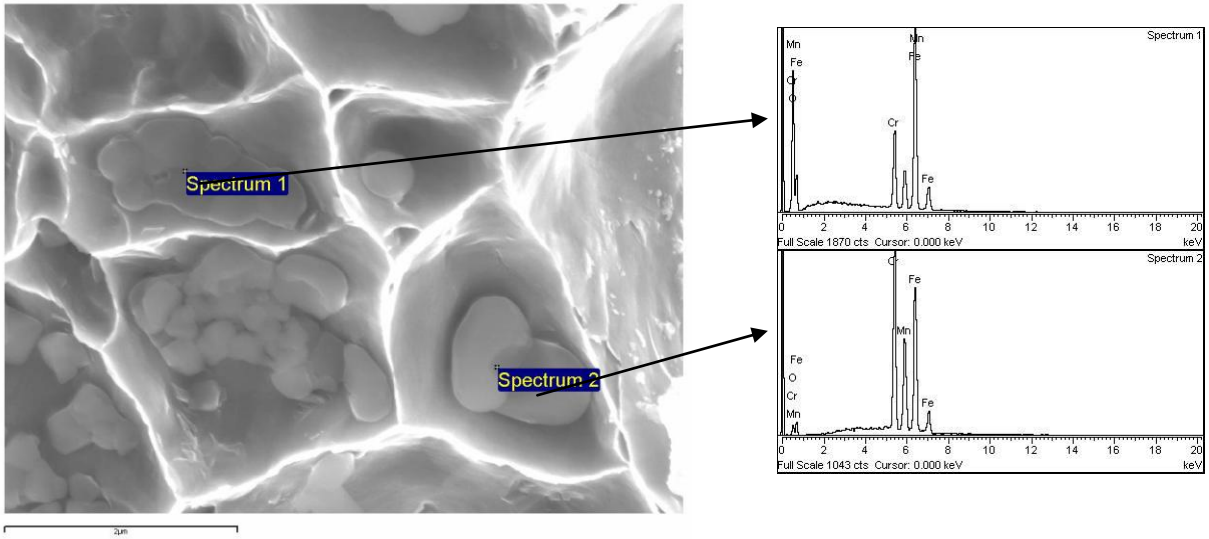

With oxygen						Without oxygen				
Spectrum	O	Cr	Mn	Fe	Total	Spectrum	Cr	Mn	Fe	Total
Spectrum 1	13.39	15.59	9.35	61.67	100.00	Spectrum 1	17.92	10.78	71.30	100.00
Spectrum 2	0.87	33.71	18.65	46.78	100.00	Spectrum 2	33.99	18.81	47.20	100.00

FIGURE 65. SEM + EDX ANALYSIS IN A1120-15.

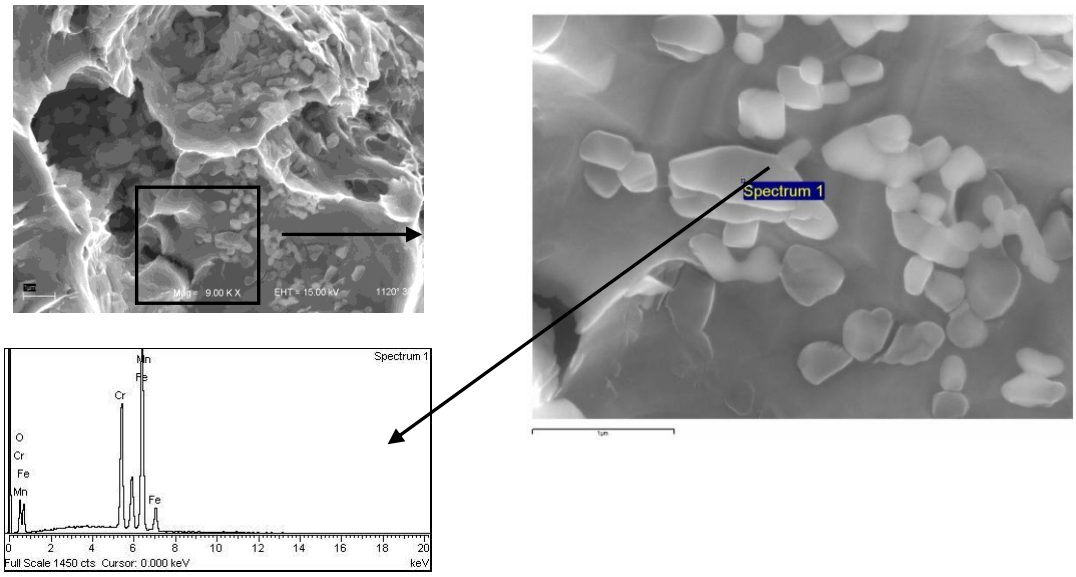

With Oxygen						Without oxygen				
Spectrum	O	Cr	Mn	Fe	Total	Spectrum	Cr	Mn	Fe	Total
Spectrum 1	3.31	24.36	10.97	61.36	100.00	Spectrum 1	25.17	11.34	63.49	100.00

FIGURE 66. SEM + EDX ANALYSIS IN A1120-15.

Analysis 65 and 66 (see Appendix II) indicate that impurities found on A1120-30 are rich in chromium and manganese. Rarely, impurities, such as sulphur, silicon, vanadium or calcium were found.

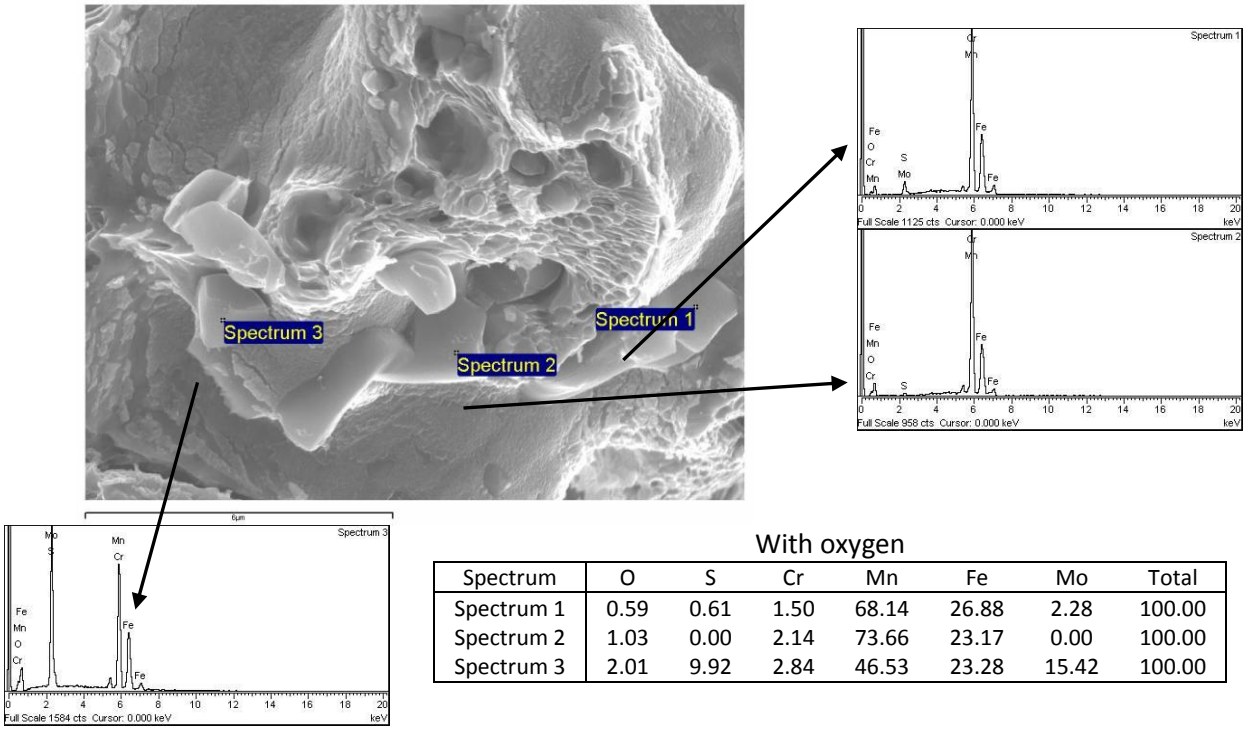

With oxygen

Spectrum	O	S	Cr	Mn	Fe	Mo	Total
Spectrum 1	0.59	0.61	1.50	68.14	26.88	2.28	100.00
Spectrum 2	1.03	0.00	2.14	73.66	23.17	0.00	100.00
Spectrum 3	2.01	9.92	2.84	46.53	23.28	15.42	100.00

Without oxygen

Spectrum	S	Cr	Mn	Fe	Mo	Total
Spectrum 1	0.59	1.47	68.60	26.98	2.37	100.00
Spectrum 2	0.00	2.16	74.48	23.36	0.00	100.00
Spectrum 3	10.20	2.91	47.57	23.74	15.58	100.00

FIGURE 67. SEM + EDX ANALYSIS IN A1120-15.

Analysis 67 shows a SEM + EDX analysis that indicates high sulphur contents, that combined with high manganese content suggest the formation of MnS. Chromium content is low. The inclusions have rectangular shapes.

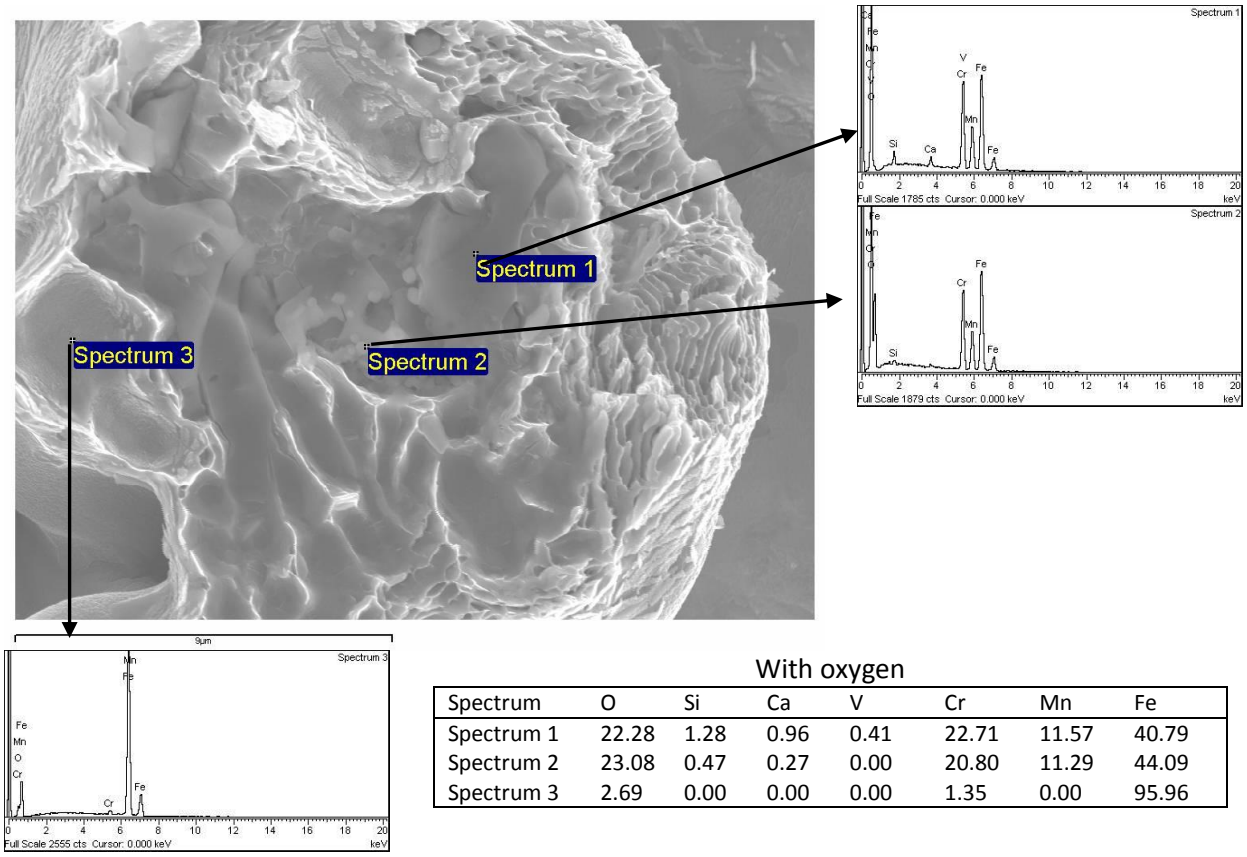

With oxygen

Spectrum	O	Si	Ca	V	Cr	Mn	Fe
Spectrum 1	22.28	1.28	0.96	0.41	22.71	11.57	40.79
Spectrum 2	23.08	0.47	0.27	0.00	20.80	11.29	44.09
Spectrum 3	2.69	0.00	0.00	0.00	1.35	0.00	95.96

Without oxygen

Spectrum	Si	Ca	V	Cr	Mn	Fe
Spectrum 1	1.76	1.25	0.52	29.02	14.83	52.62
Spectrum 2	0.66	0.36	0.00	26.85	14.64	57.49
Spectrum 3	0.00	0.00	0.00	1.38	0.00	98.62

FIGURE 68. SEM + EDX ANALYSIS IN A1120-15.

Analysis 68 shows the SEM + EDX analysis carried out at some impurities where silicon, calcium and vanadium were found. The shape of these impurities is different from other inclusions found, and form flakes. They are rich in chromium and manganese as well.

4. DISCUSSION

Microstructure

The results from the microstructural investigations show that the microstructure is heterogeneous, and that only pearlite and ferrite are presented due to the slow cooling rate. Furthermore, the pearlitic microstructure was first registered at A800-3 (~5%) close to particles edges, because the carbon diffusion was more efficient at these areas.

Above 900°C, with increasing sintering temperature carbon diffusion into the matrix becomes more pronounced. This fact leads to increasing portion of pearlite with increasing temperature. For A1120-3, A1120-15 and A1120-30 the portion of pearlite observed in the microstructures is close to 90%, result that agrees with simulations performed. This is verified by the fact that the areas with pearlitic structure were more often observed during fractographic investigation.

Some conclusions about the pores evolution can also be drawn from the microstructural investigation. With increasing temperature pores become more rounded; later on, surface and grain diffusion are contributing to pore shrinkage and rounding and thus the pore structure becomes smoother. This trend agrees with what was observed: at lower sintering temperatures, pores are irregular and distributed all along the surface. For specimens sintered at the higher temperatures, small spherical pores can be found besides irregular but rounded ones.

Fractography

As confirmed by the study of surface products formations on the chromium pre-alloyed powders by H. Karlsson and L. Nyborg [5], the surface of the powder is covered by an inhomogeneous oxide layer. This layer is made up of particulate features containing strong oxides forming elements (such as Cr, Mn , etc) and a homogeneous Fe-oxide layer (6-7nm thick) in between. Both remaining of the Fe-oxide layer and particulate features (<0.5 μm) were found on the surface of the powder particles at low sintering temperatures during electron microscopy investigation.

According to the theoretical background, the initiation of the reduction of the surface iron oxide layer occurs at low temperatures, up to 500°C by hydrogen. At temperatures above 720°C, the reducing activity of carbon increases and it begins to play a dominant role in the reducing of surface oxides due to carbothermic reduction. Therefore, for specimens sintered at lower temperatures (A700-3 and A800-3) remaining of the oxide layer is visible which points to the partial reduction of the Fe-oxide layer up to this stage. For specimens sintered at higher temperatures, the extent of the reduction of the Fe-oxide layer is much larger. Despite this, for specimens sintered at 1120°C because of the slow cooling rate, there is evidence of re-oxidation during cooling. This re-oxidation is more evident in the outer part of the specimens, because at this stage of sintering in the inner part the porosity is closed and therefore interaction with atmosphere is limited.

The pre-condition for the formation of inter-particle necks is the reduction of this oxide layer on the powder particles. As was said above, in A700-3 and A800-3 reduction of the Fe-oxide layer is not complete and therefore only point and short line connections between particles were identified. These contacts were created during the compaction stage, and from them the onset of necks development will take place. On the contrary, in A900-3, A1000-3 the Fe-oxide layer is reduced and inter-particle necks are more developed because of the high diffusion rate. Because of this, above A1000-3 sinter necks appear as interconnected networks of fine dimples. For specimens sintered at

1120°C it is clearly discernible that inter-particle necks are more developed with increasing temperature and time.

As a result of the necks formation process, it can be seen how for lower sintering times (A700-3, A800-3 and A900-3) the fracture surface is rough and individual particles and their agglomerates are visible. For specimens sintered at higher sintering temperatures, the fracture surface becomes smoother, and individual particles cannot be distinguished anymore.

Consequently, from the fractographic investigations carried out on the sintered specimens necks formation is clearly discernible from the appearance of various types of broken contacts, and conclusions about the main failure mechanisms can be made:

- Point contacts and short/branched line ductile fracture for low temperatures.
- Dimple ductile fracture for high temperatures, initiated by:
  - Bridge porosity
  - Cementitic lamellae of pearlitic structures
  - Particulates features (if not reduced)

A feature that is especially evident for specimens sintered at temperatures up to 1000°C is that inter-particle connections are more developed close to the specimen surfaces (edges); this may be due to the fact that the outer part of the specimen was more “open” to the sintering atmosphere and thus the reduction process was more efficient.

As was said, particulate compounds cover a minor part of the surface; this is favorable for the sintering behavior of the powder, since the Fe-oxides are easier to reduce than the Cr, Mn or Si oxides and therefore inter-particle necks development will start at the contact points where the iron oxides have been reduced.

In A700-3 and A800-3 spherical particulate features were found on the free powder particles surfaces sizing up to 0.5µm; in some cases agglomerates of irregularly shaped particulates sizing up to 2µm were found as well. In extremely rarely situations, they were also found inside developed contacts shielded from the atmosphere. From SEM + EDX analysis carried out at all the specimens, it must be taken into consideration that the interaction volume is much bigger than the analyzed dots, and therefore the accuracy of the method only provides qualitative information. Despite this consideration, the SEM + EDX analysis performed in A700-3 and A800-3 show that particulate features are rich in Cr and Mn.

In A900-3, besides particulate features on the powder particles surfaces, inclusions inside dimples and on developed necks were seldom found. The shape of these inclusions is more irregular when compared with features found in A700-3 and A800-3, but their size is also below 0.5µm. SEM + EDX analysis performed show that they are complex refractory oxides with high chromium and manganese content.

In turn, in A1000-3 on the inter-particle necks two different types of inclusions can be found: first, irregularly shaped with size up to 1µm and spherical inclusions up to 1µm. The difference in morphology and size depends on the local conditions, if these particulates where partially reduced by the protective atmosphere or not. EDX + SEM analysis performed indicate that both types of inclusions are complex refractory oxides with high chromium and manganese content. This content “seems” to increase in comparison with specimens previously analyzed, but no safe conclusions can be drawn because of the limitations of the experimental method.

For specimens sintered at 1120°C during different times the same patterns were observed:

- Irregularly shaped agglomerations made up by the coalescence of small (<0.5μm) spherical inclusions.
- Irregularly shaped inclusions up to 1μm, which were not reduced by the protective atmosphere.
- Spherical inclusions with sizes up to 1μm and above.

SEM + EDX analysis carried out show high Cr and Mn contents in that all these inclusions.

In addition, SEM + EDX analysis performed In A1120-30 rarely show S, Si, V and Ca presence. S found on fractured sinter necks with the simultaneous presence of manganese, this suggests the formation of MnS. A probable source for the S could be the graphite added to the original powder mix prior to the sintering. In turn, the source of Si, V and Ca is not well defined.

There is not clear understanding of the forces that govern the change in morphology, size and composition of inclusions with sintering temperature and time, and therefore the explanation to this phenomenon remains out of the purposes of this study. Nowadays, investigations are being carried out in order to define the driving forces and to create a model that predicts the evolution of inclusions with sintering temperature and time.

5. CONCLUSIONS

In the present work, impact test was performed in previously sintered specimens at different temperatures and times in order to produce fracture surfaces. For fractographic investigations, High Resolution Scanning Electron Microscopy (HRSEM) and optical microscope were used. The objective of this investigation was the evaluation of the inter-particle necks development and of the evolution of inclusions, with sintering temperature and time. The conclusions that can be drawn from the obtained results can be summarized as follows:

- The results from the microstructural investigations show that the microstructure is heterogeneous, and that only pearlite and ferrite are presented due to the slow cooling rate. Furthermore, the pearlitic microstructure was first registered at A800-3 and for specimens sintered at 1120°C the portion of pearlite agrees with simulations performed (~90%).

- Pores become more rounded with increasing temperature: for specimens sintered at the higher temperatures studied, both small spherical pores and irregular but rounded ones can be found.

- Inter-particle necks development is enhanced with sintering temperature and time. Pre-condition for the formation of solid metallic contacts is the reduction of the Fe-oxide layer present on the powder particles surface.

- Inter-particle connections are more developed close to the specimens surfaces (edges), because the outer part of the specimen is more “open” to the sintering atmosphere and therefore the reduction process is more efficient at those areas.

- Remaining of the oxide layer was visible in A700-3 and A800-3. For specimens sintered at higher temperatures, the extent of the reduction of the Fe-oxide layer is much larger. For specimens sintered at 1120°C there is some evidence of re-oxidation during cooling, that is more pronounced at the outer part of the specimens.

- The main failure mechanism of the fracture surfaces are:
    - Point contacts and short/branched line ductile fracture for low temperatures.
    - Dimple ductile fracture for high temperatures, initiated by:
        - Bridge porosity
        - Cementitic lamellae of pearlitic structures
        - Particulates features (if not reduced)

- For A700-3 and A800-3 spherical particulate features were found on the free particles surfaces (<0.5μm); in some cases, agglomerates of particulates that probably are originated from the base powder sizing up to 2μm are also found. At A900-3, inclusions inside dimples and on developed necks were seldom found as well.

- In A1000, two different types of inclusions can be found on the inter-particle necks: irregular and spherical inclusions sizing up to 1μm. The difference in morphology and size lies on whether they were reduced or not.

- For specimens sintered at 1120°C different patterns were observed:
    - Irregularly shaped agglomerations made up by the coalescence of small (<0.5µm) spherical inclusions.
    - Irregularly shaped inclusions up to 1µm, which were not reduced by the protective atmosphere.
    - Spherical inclusions with sizes up to 1µm and above.

- SEM + EDX analysis show that inclusions are complex refractory oxides, with high Cr and Mn content. Impurities such as S, Si, Ca and V can be found rarely.

6. REFERENCES

[1] Randall, M. German. *Powder metallurgy science.* Metal powder Industries federation, 1994.

[2] Various authors. *ASM Metals Handbook Volume 7*. Properties and applications

[3] A. Lawley: *Encyclopedia of Materials: Science and Technology.* Atomization, pp. 387-392, *2008*

[4] J. M. Capus. *Metal powders,* pp. 153-165, 2005.

[5] H. Karlsson. PhD Thesis: *Role of surface in sintering of Chromium-Alloyed steel powders*. Chalmers University of Technology, 2005.

[6] K. Mori, M. Ohashi and K. Osakada, *Simulation of microscopic shrinkage behavior in sintering of powder compact.* Int. J. Mech. Sci, vol 40, No. 10, pp. 989-999, 1998.

[7] P. Bross and H. E. Exner, *Acta metall*. No. 27, pp.1013, 1979.

[8] W. Zhang and J. H. Schneibel. *The sintering of two particles by surface and grain boundary diffusion; a two dimensional numerical study*. Acta metall. mater, vol 43, No 12, pp 4377-4386, 1995.

[9] A. K. Eksi and A. H. Yuzbasioglu. *Effect of sintering and pressing parameters on the densification of cold isostatically pressed Al and Fe powders*. Materials and Design 28, pp. 1364-1368, 2007.

[10] Höganas Handbook for sintered materials. Vol. 1, 2.

[11] H. Danninger, R. Pöttshacher, S. Bradac, A. Salak and J. Seyrkammer. *Comparison of Mn, Cr and Mo alloyed sintered steels prepared from elemental powders. Powder Metallurgy, vol. 48 No. 1, pp. 23-32, 2005.*

[12] H. Danninger, Chen Xu and Björn Lindqvist. *Oxygen removal during sintering of steels prepared from Cr-Mo and Mo prealloyed powders*. Materials Science Forum, Vols. 534-536, pp. 557-580, 2007.

[13] E. Hryha, L. Cajkova, E. Dudrova and L. Nyborj. *Study of reduction/oxidation processes in Cr-Mo Prealloyed steels during sintering by continuous atmosphere monitoring. Euro PM2008, sintered steels, pp. 109-114.*

[14] S. C. Mitchell, A. Cias: Powd. Met. Prog. , Vol 4, 2004, No 3, pp 132-142

[15] W. Schatt, K. Wieters: Powder Metallurgy, processing and materials. European Powder Metallurgy Association, 1997.

[16] O. Bergman: *Influence of oxygen partial pressure in sintering atmosphere on properties of Cr-Mo prealloyed powder metallurgy steel*. Powder Metallurgy, vol. 50, No. 3, 2007.

[17] H. Danninger, C. Gierl, S. Kremel, G. Leitner, K. Jaenicke-Roessler, Y.Yu: *Degassing and deoxidation processes during sintering of unalloyed and alloyed PM steels*. Powder Metallurgy Progress, Vol. 2, No. 3, 2002.

[18] P. Ortiz, F. Castro: *Thermodynamic and experimental study of role of sintering atmospheres and graphite additions on oxide reduction in Astaloy CrM powder compacts.* Powder Metallurgy, vol. 47, No. 3, 2004.

[19] E. Hryha: *Powder Metallurgy Progress*, vol 7, No 4, pp. 181-197, 2007

[20] P. Bracconi and L. Nyborg: *Quantitative phase analysis and thickness measurement of surface-oxide layers in metal and alloy powders by the chemical-granular method.* Applied Surface Science, 133, pp. 129-147, 1998.

[21] M. Campos, L. Blanco and J.M. Torralba: *Thermal analysis of prealloyef Fe-3Cr-0,5Mo sintered steel.* Journal of Thermal Analysis and Calorimetry, Vol. 84, pp. 483-487, 2006.

[22] European Powder Metallurgy Association webpage: www.epma.com

[23] H.Danninger, Christian Gierl: *Processes in Pm steel compacts during the initial stages of sintering*. Materials Chemistry and Physics, 67, pp. 49-55, 2001.

[24] Z. He and J. Ma: *Grain-growth law during Stage 1 sintering of materials. J. of Physics D:Appli. Physics , 35, pp. 2217-2221, 2002.*

[25] R.L. Eadie and G. C. Weatherly: *Solutions for the shrinkage rate in the intermediate stage of sintering. Scripta Metallurgica, vol. 9, pp. 285-294, 1975.*

[26] B. Haller, A. Grimaud,J.C. Labbe and J. P. Bonnet: *TiO-based coatings prepared by plasma spraying in air of Ti + C mixtures.* J. Mater. Res., Vol 21, No 7, 2006.

[27] H. Danninger and C. Gierl**:** *New Alloying Systems for Ferrous Powder Metallurgy Precision Parts.* Science of sintering, vol. 40, pp. 33-46, 2008.

[28] Software: JMatPro 4.0: The materials property simulation package

7. ACKNOWLEDGEMENTS

Here it is: I have finished my degree and now I am writing the last words of my Master Thesis! I am very grateful to all the people that have followed this path with me, to only some of whom it is possible to give a particular mention here:

To my examiner, Professor Lars Nyborg, who gave me the opportunity of working at the Department of Materials and Manufacturing Technology, for which I am extremely grateful.

Dimitris Chasoglou, my supervisor to whom I am deeply indebted for his help, suggestions and patience during both the research and writing of this thesis; to Eduard Hryha for all the help and encouragement especially during this last month. To Ruth Ariño and Henrik Borgström I would like to thank them for their kindness and to all the staff in the department for creating such a good working atmosphere.

To Professor Jose Manuel Torralba, for all his help during my studies at Carlos III University and especially during the months I studied abroad. Thanks for making it all easier! To my teachers in the past, Elisa Ruiz Navas and Mónica Campos Gómez because they helped me to decide what I really wanted to study.

To all my family here in Sweden: Högsbo, Frölunda, Belgium and a small part of Greece, my Catalan family, flatmates and neighbors. You have all made me feel at home, and from each of you I have learnt something that made me grow as a person. Especially I would like give thanks to my tata, Elena during these months I found the sister I never had, “and you know you will always love me”.

To all my friends at Carlos III University, in particular my close friends (Nacho, Jorge, Diego, Nico and Jaime) and my girls, Raquel and Ana. Ana, I will always be very proud of you because of your strength and for the hard fight you have won!

To my friends from “Sanse” (Laura, Diana, Marta, Nia, Cris, Irene and Laura) it is a miracle that you all are still here after these years, thank you all!

To Juan Carlos, Thank you for all the support and good moments we have lived and for all the moments still to come. You know ”No se si pensar…”

Last but not least to all my family for their support. In particular, I would like to thank my grandparents because they have showed me that all wars can be won, when you fight with your heart. To my brothers, Carlos and Abel and my parents Abel and Dolores: Now I understand how difficult it was to raise us and that you always wanted the best for us. I really think that you have done an excellent job.

I am sure I am forgetting a lot of people that I have met during these years. To you all thanks a lot!

APPENDIX I

A700-3

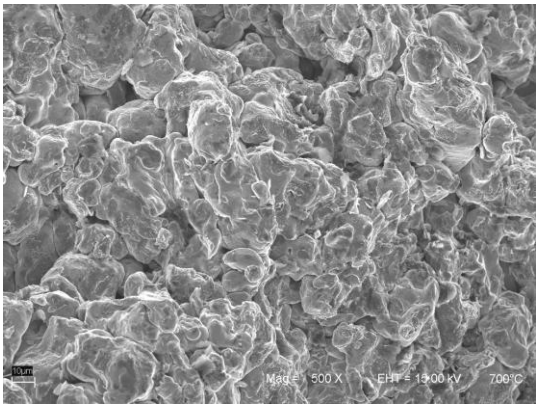
Mag = 500 X EHT = 15.00 kV 700°C

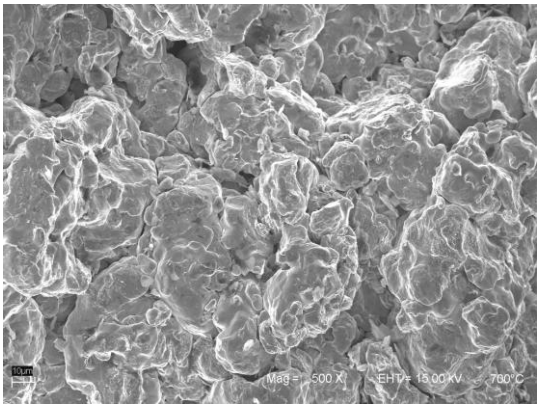
Mag = 500 X EHT = 15.00 kV 700°C

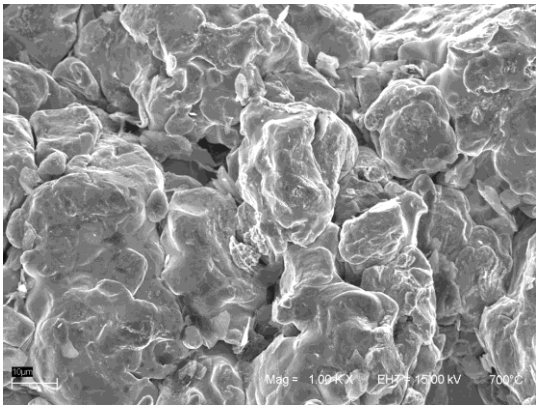
Mag = 1.00 K X EHT = 15.00 kV 700°C

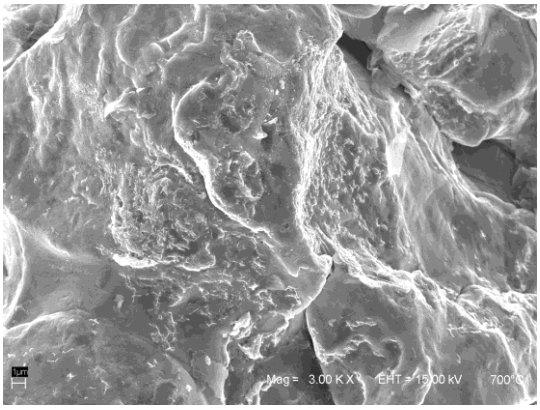
Mag = 3.00 K X EHT = 15.00 kV 700°C

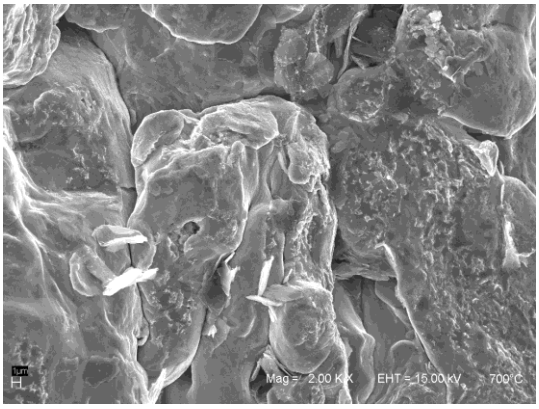
Mag = 2.00 K X EHT = 15.00 kV 700°C

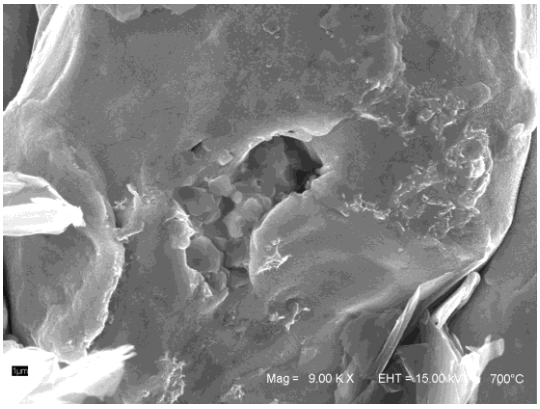
Mag = 9.00 K X EHT = 15.00 kV 700°C

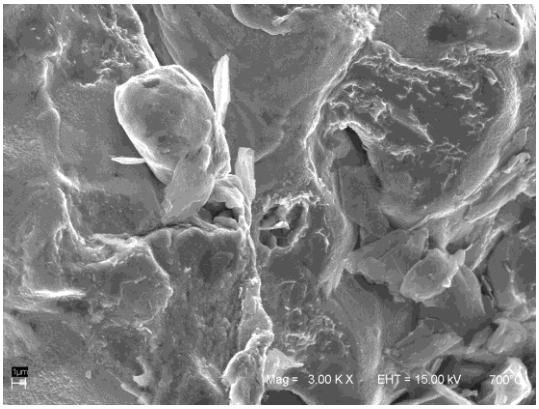
Mag = 3.00 K X EHT = 15.00 kV 700°C

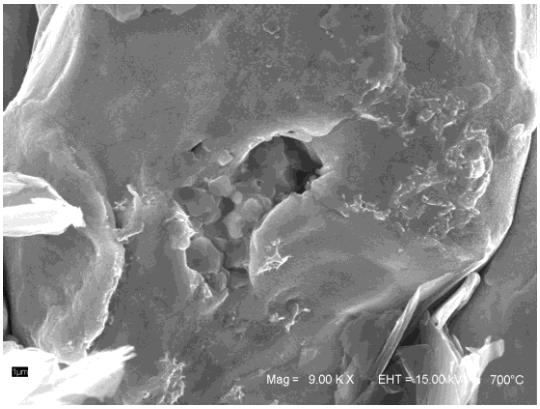
Mag = 9.00 K X EHT = 15.00 kV 700°C

A800-3

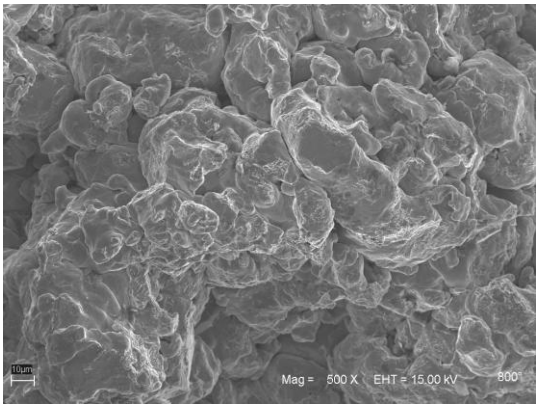
Mag = 500 X EHT = 15.00 kV
800°

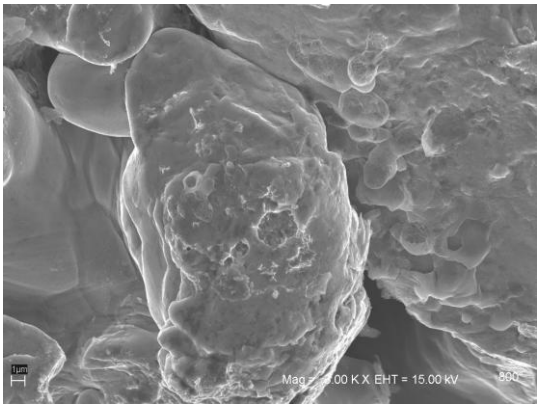
800°

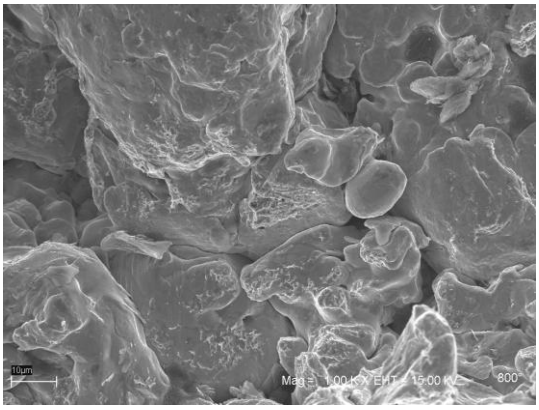
800°

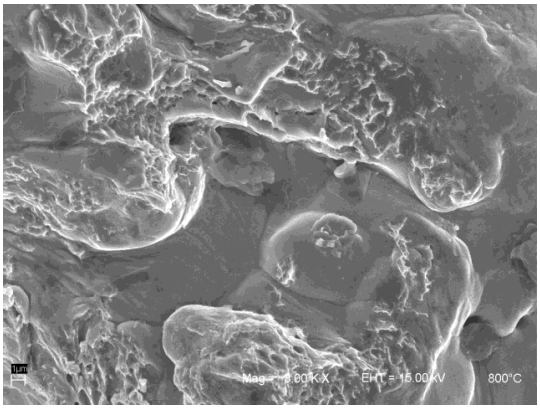
800°C

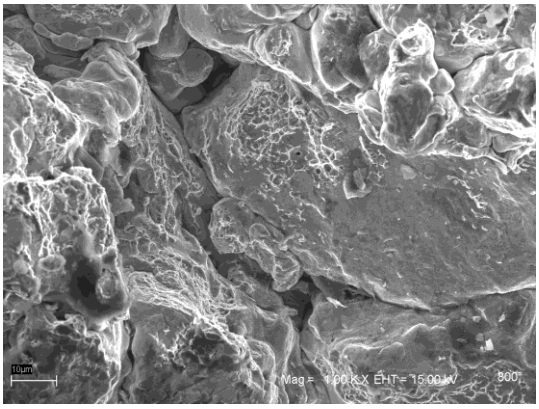
800°

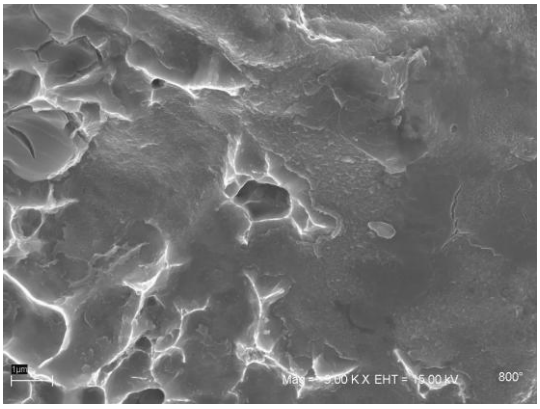
800°

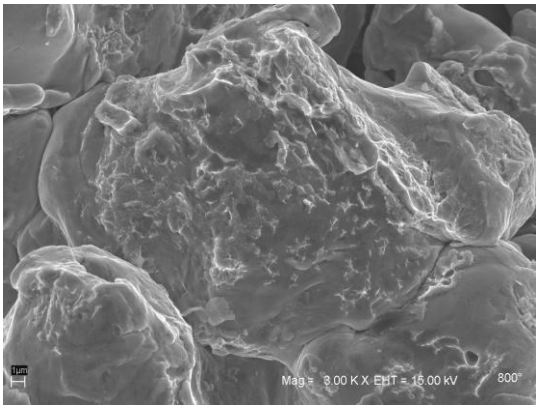
Mag = 3.00 K X EHT = 15.00 kV
800°

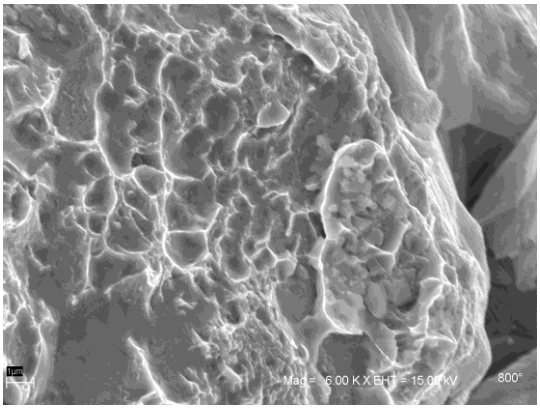
800°

A900-3

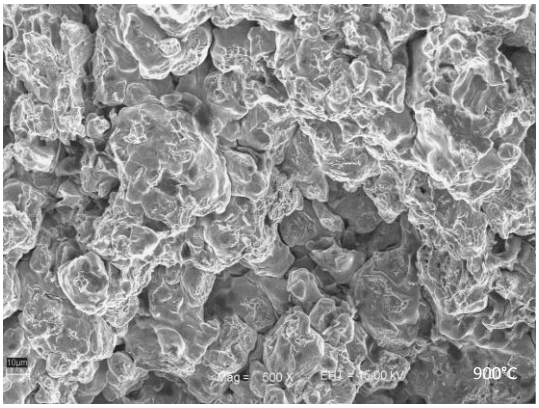
900°C

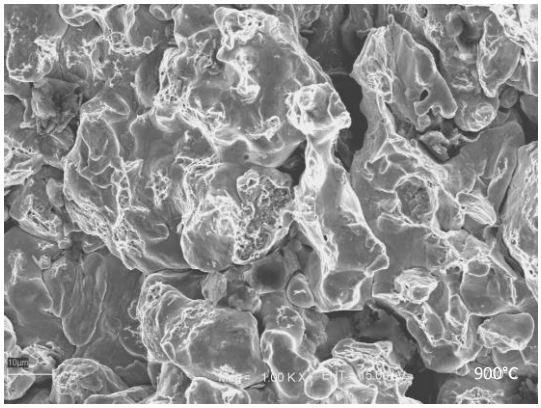
900°C


900°C

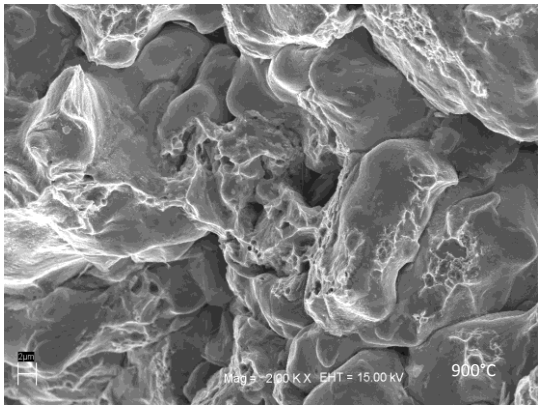
Mag = 2.00 K X EHT = 15.00 kV
900°C

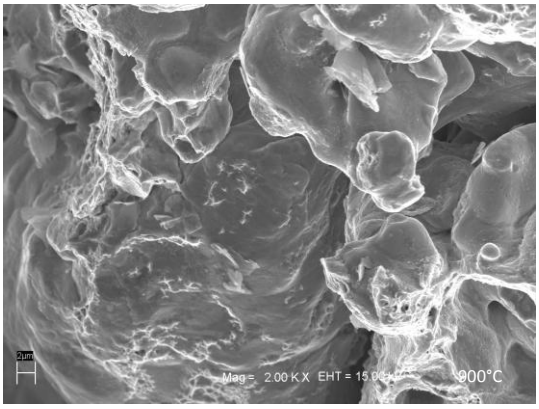
Mag = 2.00 K X EHT = 15.00 kV
900°C

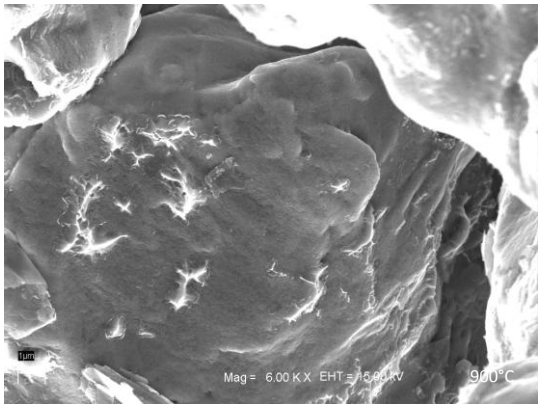
Mag = 6.00 K X
900°C

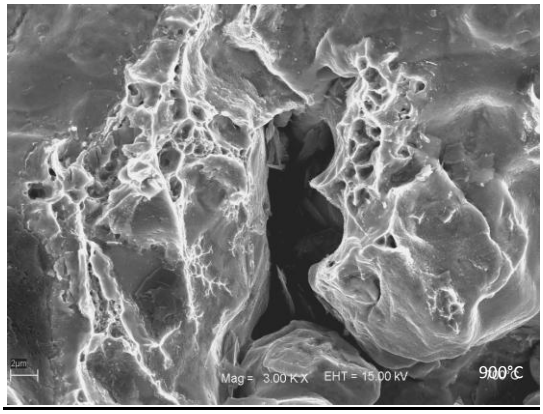
Mag = 3.00 K X EHT = 15.00 kV
900°C

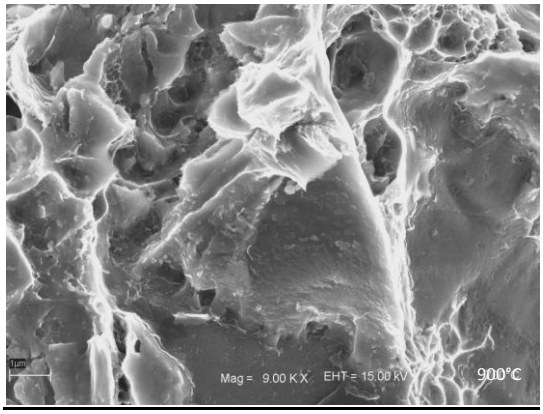
Mag = 9.00 K X EHT = 15.00 kV
900°C

1000-3

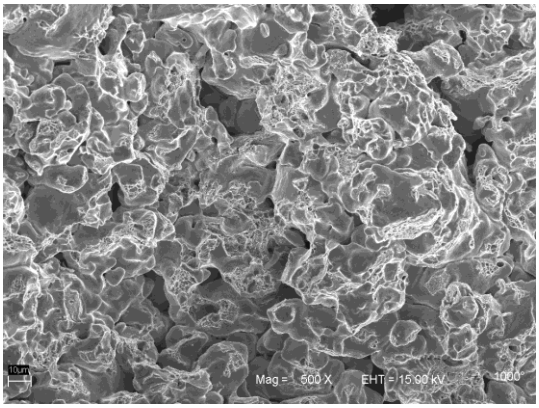
Mag = 500 X EHT = 15.00 kV 1000°

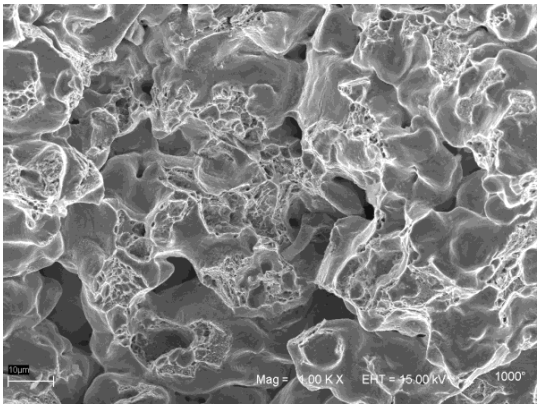
Mag = 1.00 K X EHT = 15.00 kV 1000°

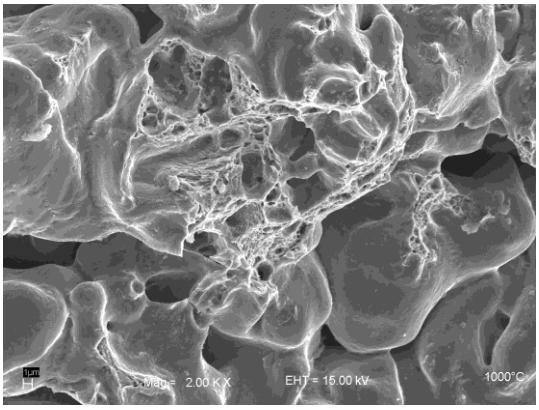
Mag = 2.00 K X EHT = 15.00 kV 1000°C

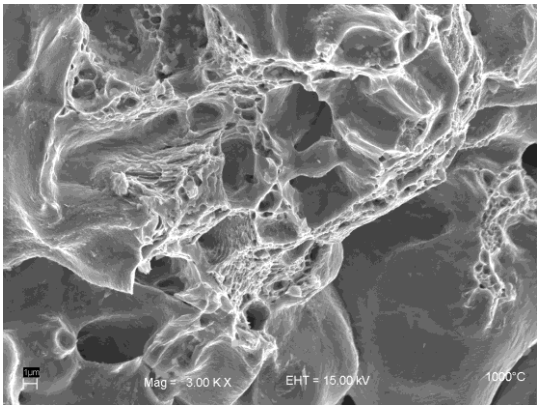
Mag = 3.00 K X EHT = 15.00 kV 1000°C

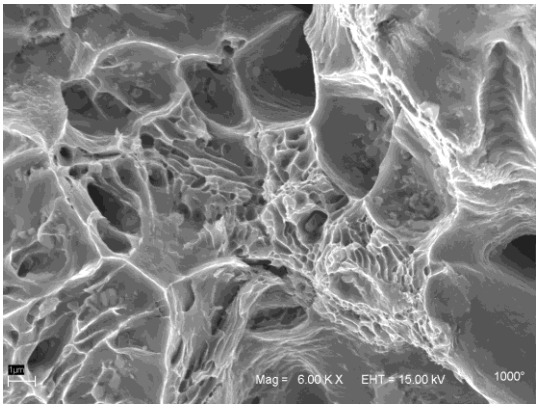
Mag = 6.00 K X EHT = 15.00 kV 1000°

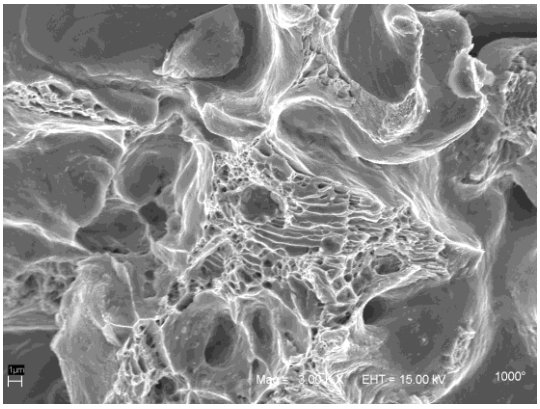
EHT = 15.00 kV 1000°

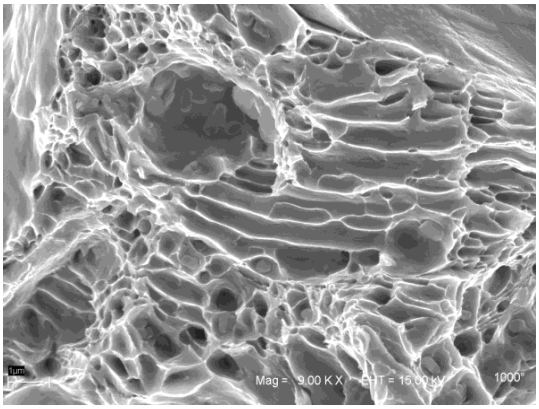
Mag = 9.00 K X 1000°

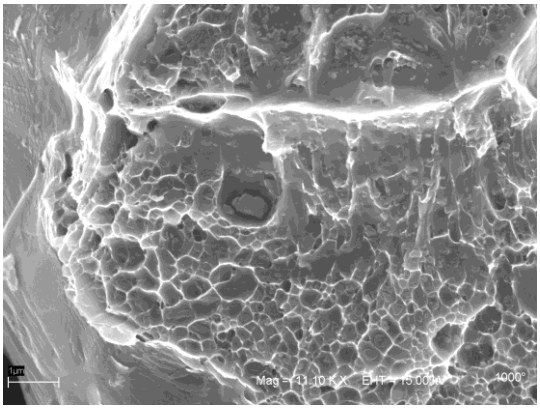
1000°

A1120-3

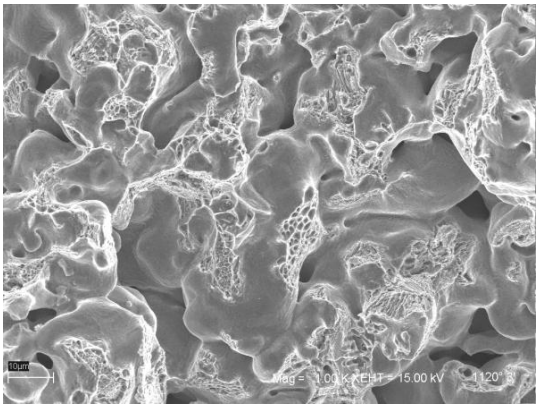
Mag = 1.00 K X EHT = 15.00 kV 1120° 3'

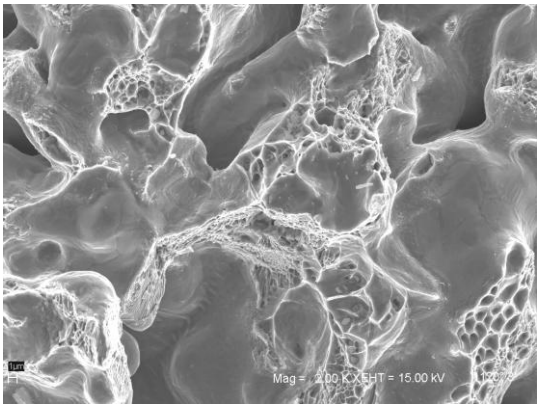
Mag = 2.00 K X EHT = 15.00 kV

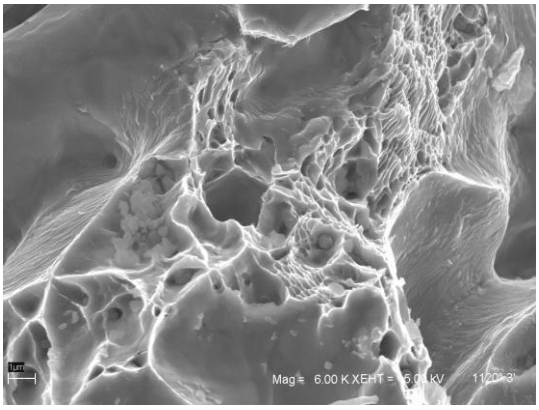
Mag = 6.00 K X EHT = 15.00 kV 1120° 3'

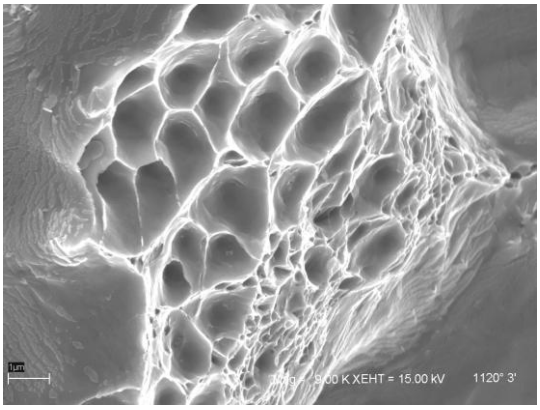
Mag = 8.00 K X EHT = 15.00 kV 1120° 3'

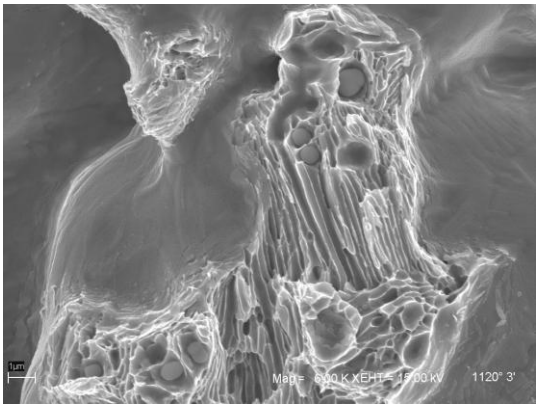
Mag = 6.00 K X EHT = 15.00 kV 1120° 3'

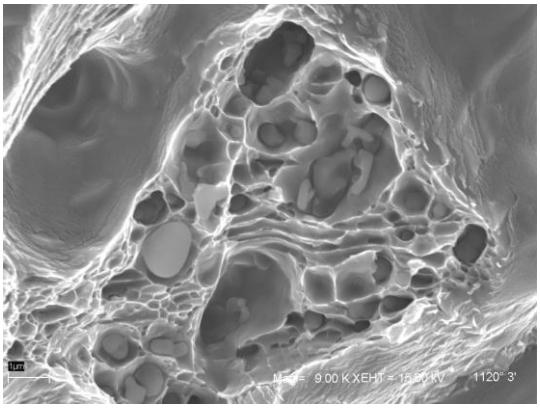
Mag = 9.00 K X EHT = 15.00 kV 1120° 3'

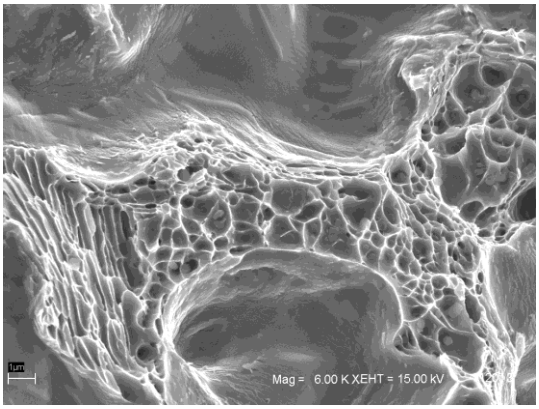
Mag = 6.00 K X EHT = 15.00 kV

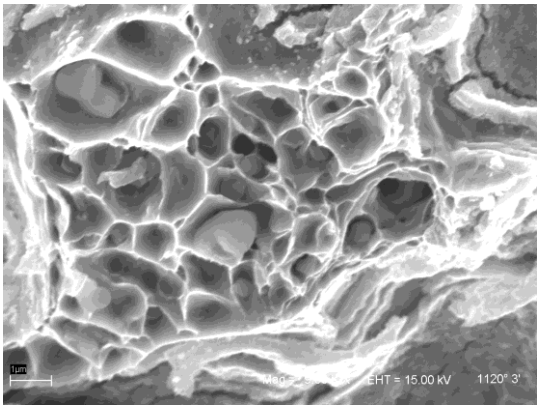
EHT = 15.00 kV 1120° 3'

A1120-15

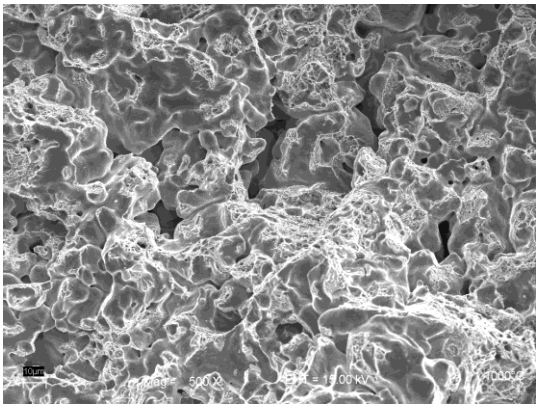
10µm
Mag = 500 X
EHT = 15.00 kV
1120°C 15'

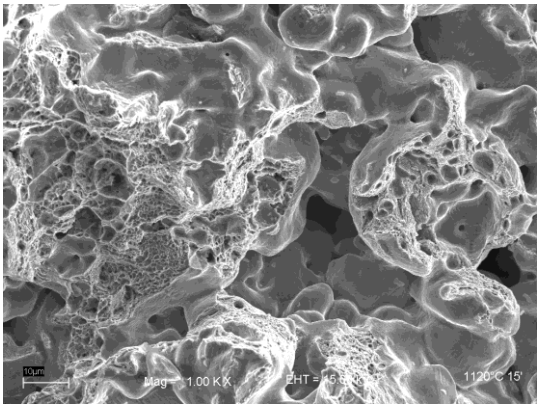
10µm
Mag = 1.00 K X
1120°C 15'

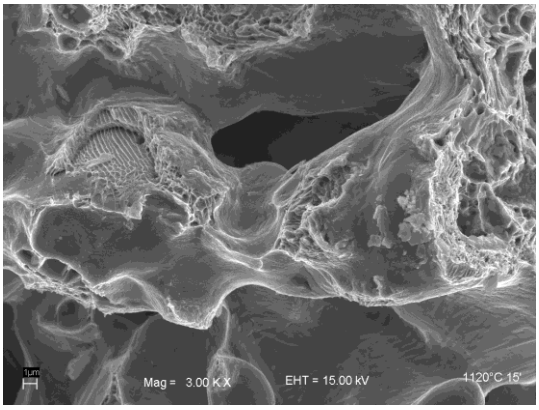
1µm
Mag = 3.00 K X
EHT = 15.00 kV
1120°C 15'

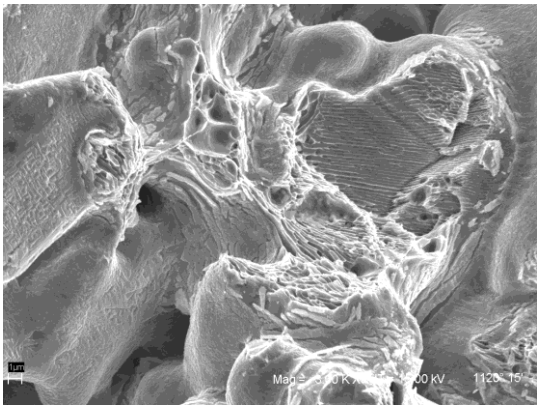
1µm
1120°C 15'

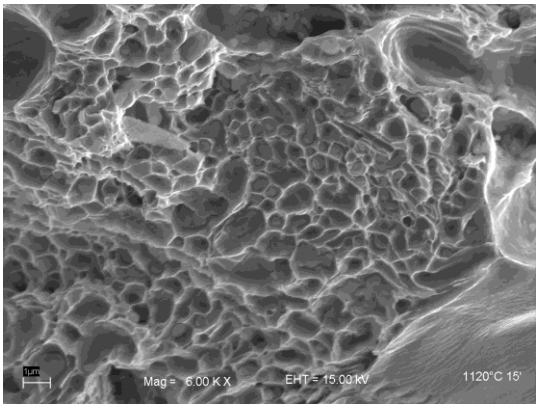
1µm
Mag = 6.00 K X
EHT = 15.00 kV
1120°C 15'

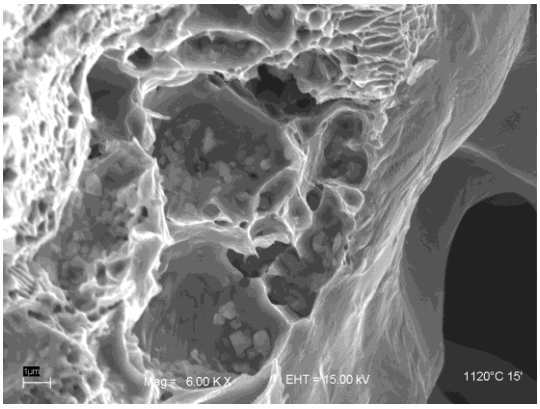
1µm
Mag = 6.00 K X
EHT = 15.00 kV
1120°C 15'

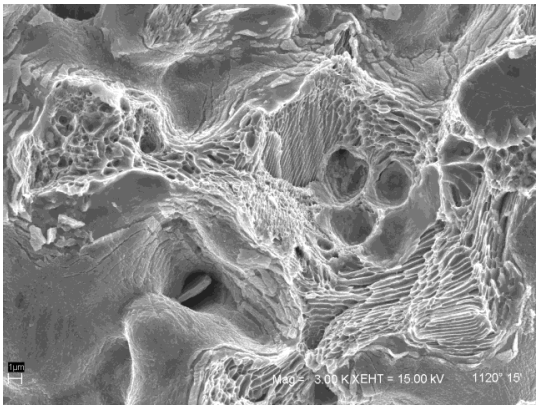
1µm
Mag = 3.00 K X
EHT = 15.00 kV
1120° 15'

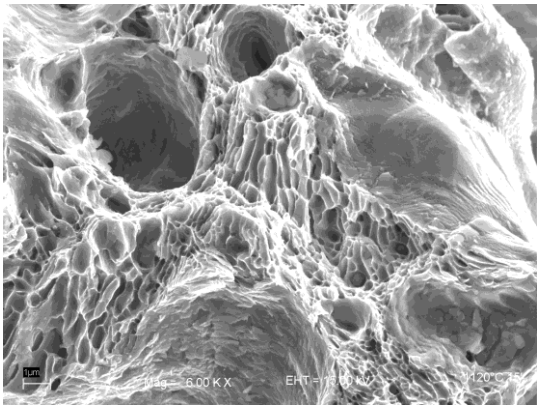
1µm
Mag = 6.00 K X
1120°C 15'

A1120-30

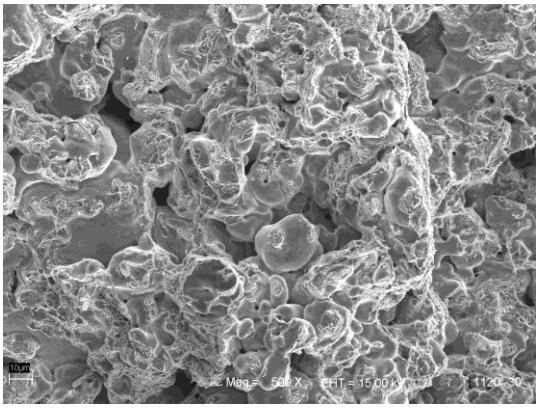
Mag = 500 X EHT = 15.00 kV 1120° 30'

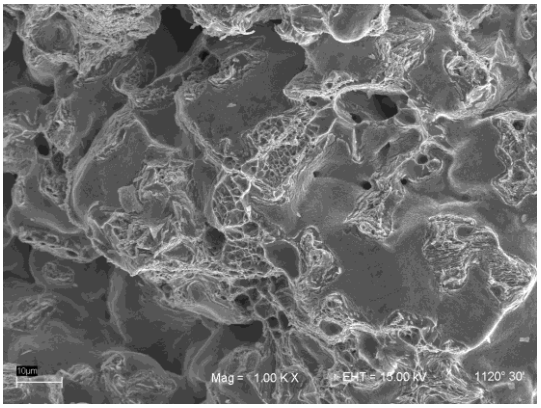
Mag = 1.00 K X EHT = 15.00 kV 1120° 30'

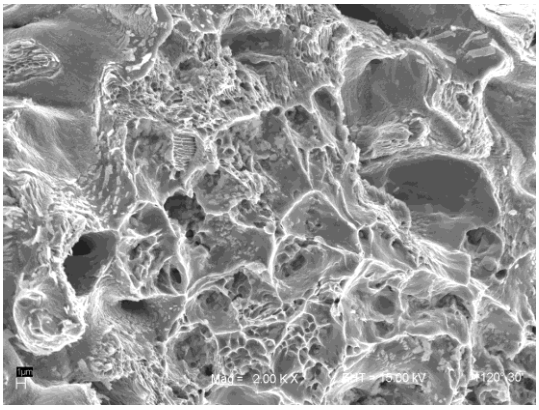
Mag = 2.00 K X EHT = 15.00 kV 1120° 30'

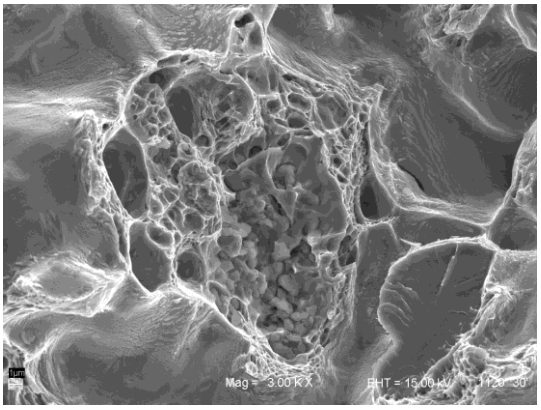
Mag = 3.00 K X EHT = 15.00 kV 1120° 30'

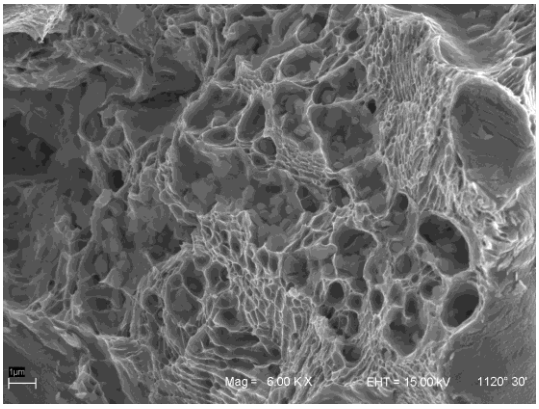
Mag = 6.00 K X EHT = 15.00 kV 1120° 30'

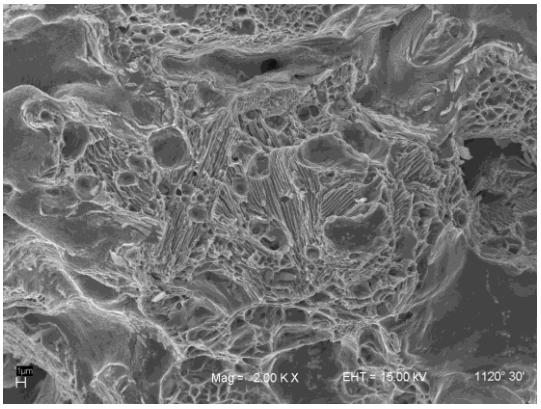
Mag = 2.00 K X EHT = 15.00 kV 1120° 30'

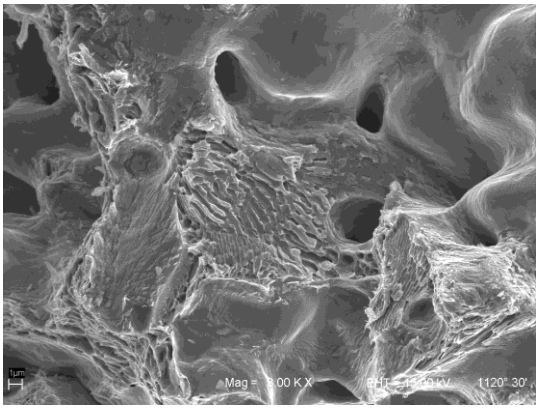
Mag = 9.00 K X EHT = 15.00 kV 1120° 30'

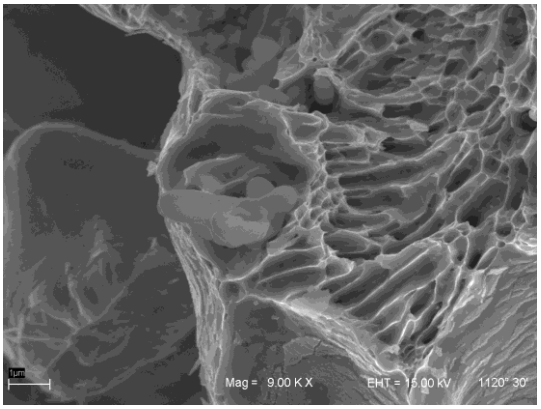
Mag = 9.00 K X EHT = 15.00 kV 1120° 30'

APPENDIX II

A700-3

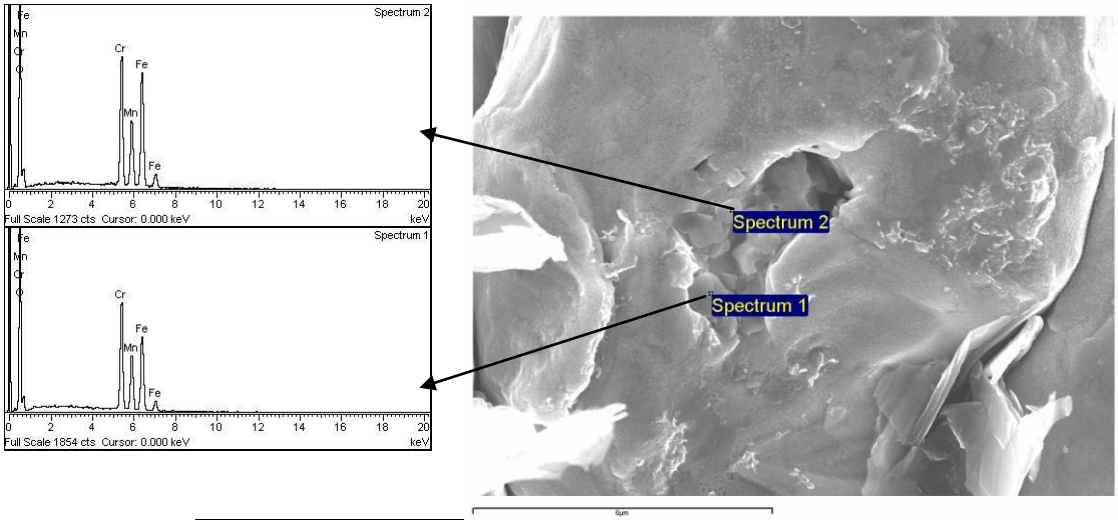

With Oxygen					
Spectrum	O	Cr	Mn	Fe	Total
Spectrum 1	47.03	20.25	11.00	21.72	100.00
Spectrum 2	39.96	20.85	11.43	27.76	100.00

Without oxygen				
Spectrum	Cr	Mn	Fe	Total
Spectrum 1	38.07	20.71	41.22	100.00
Spectrum 2	34.59	19.01	46.40	100.00

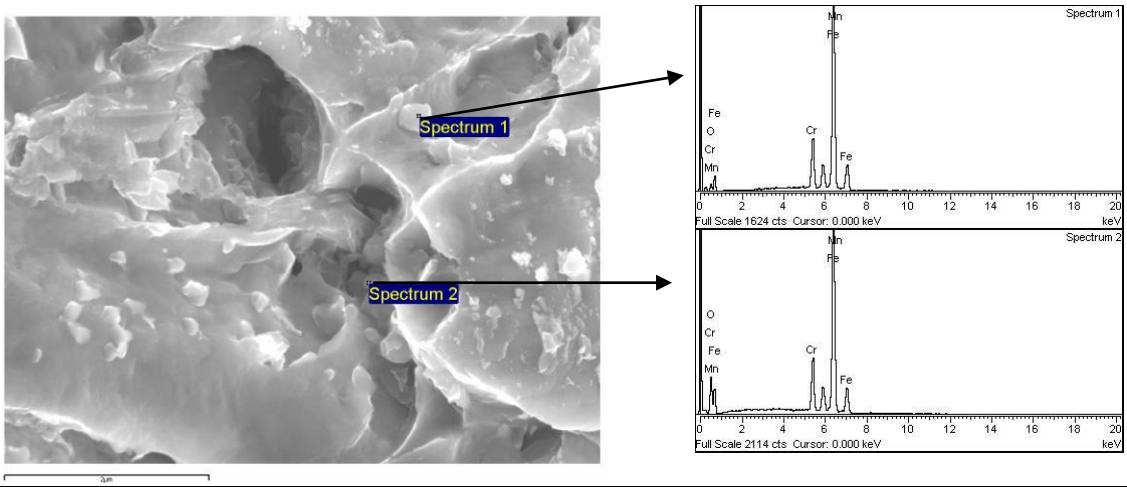

With Oxygen						Without oxygen				
Spectrum	O	Cr	Mn	Fe	Total	Spectrum	Cr	Mn	Fe	Total
Spectrum 1	3.77	12.27	6.76	77.21	100.00	Spectrum 1	12.74	7.01	80.26	100.00
Spectrum 2	14.31	12.00	6.02	67.67	100.00	Spectrum 2	13.97	7.04	78.99	100.00

A800-3

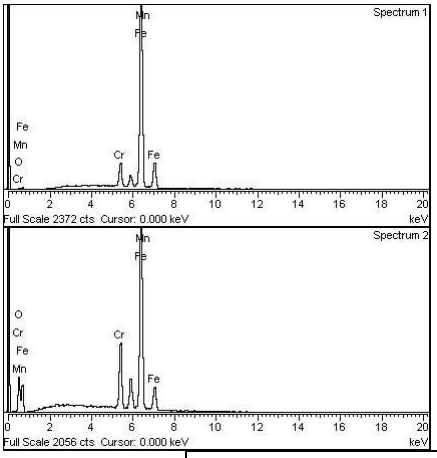

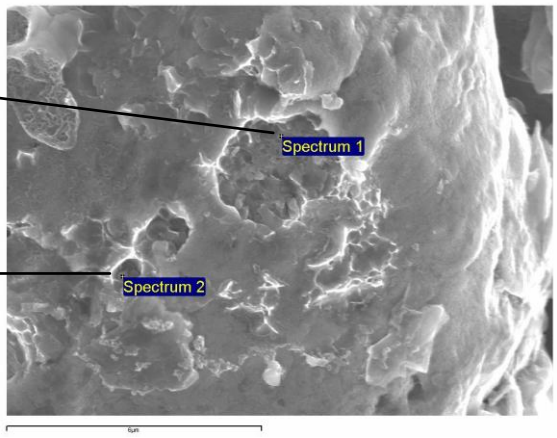

With Oxygen					
Spectrum	O	Cr	Mn	Fe	Total
Spectrum 1	0.78	6.92	3.60	88.69	100.00
Spectrum 2	12.86	14.55	7.03	65.56	100.00

Without Oxygen				
Spectrum	Cr	Mn	Fe	Total
Spectrum 1	6.98	3.63	89.39	100.00
Spectrum 2	16.67	8.07	75.26	100.00

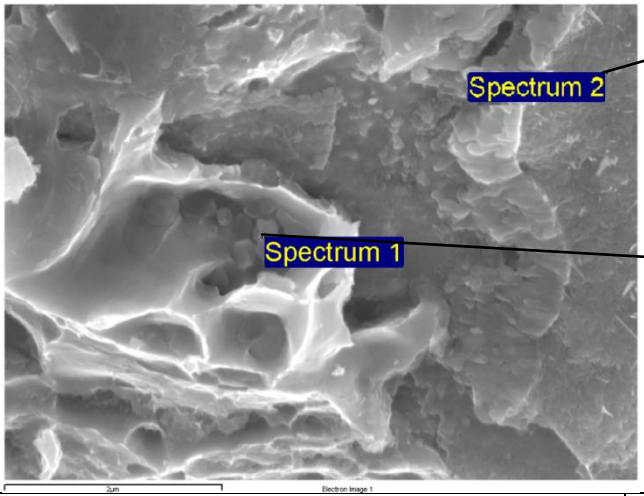

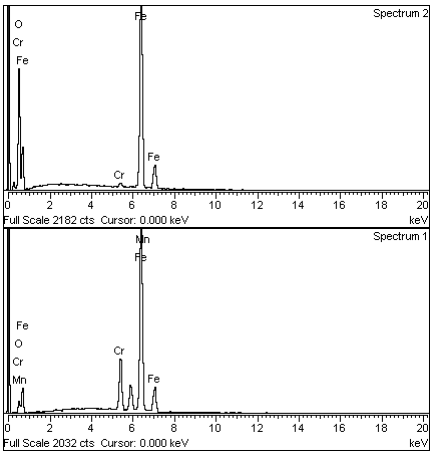

With Oxygen					
Spectrum	O	Cr	Mn	Fe	Total
Spectrum 1	5.29	13.11	6.77	74.83	100.00
Spectrum 2	40.54	0.82		58.63	100.00

Without oxygen				
Spectrum	Cr	Mn	Fe	Total
Spectrum 1	13.84	7.15	79.02	100.00
Spectrum 2	1.37		98.63	100.00

A900-3

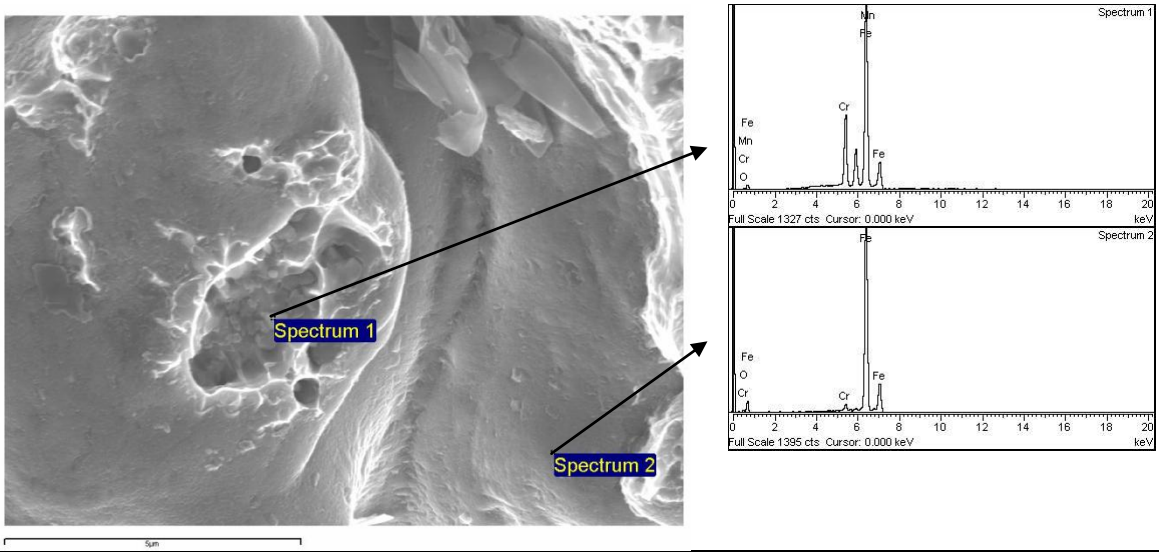

Oxygen						Without oxygen				
Spectrum	O	Cr	Mn	Fe	Total	Spectrum	Cr	Mn	Fe	Total
Spectrum 1	0.55	17.37	9.55	72.54	100.00	Spectrum 1	17.46	9.60	72.93	100.00
Spectrum 2	1.14	1.77		97.09	100.00	Spectrum 2	1.79		98.21	100.00

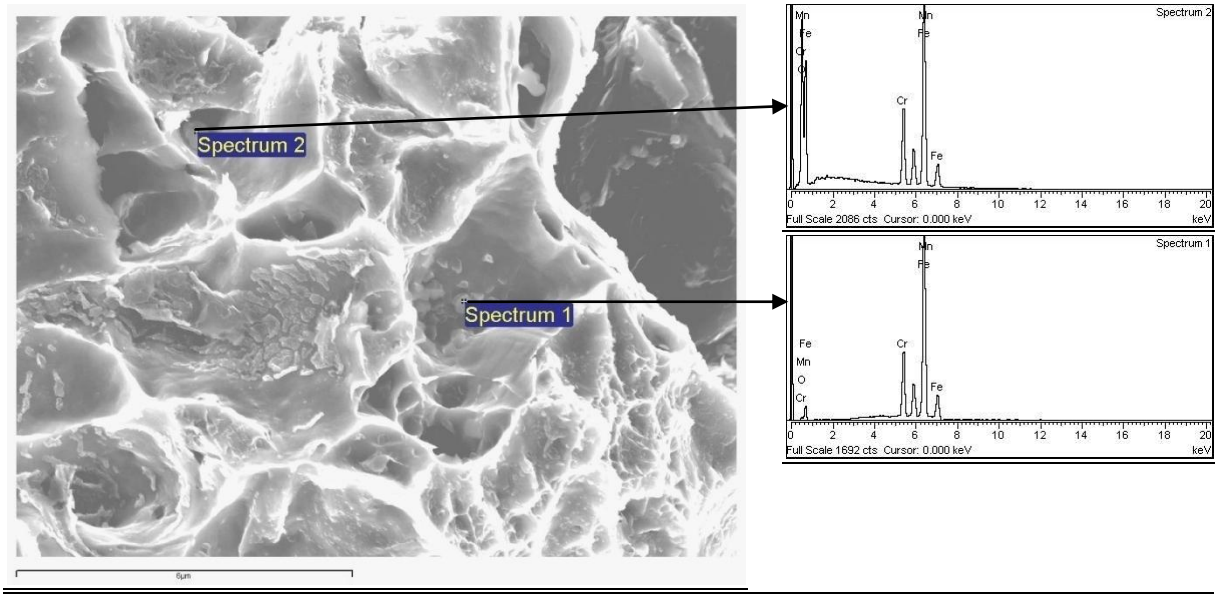

With oxygen						Without oxygen				
Spectrum	O	Cr	Mn	Fe	Total	Spectrum	Cr	Mn	Fe	Total
Spectrum 1	0.00	16.44	9.14	74.42	100.00	Spectrum 1	16.44	9.14	74.42	100.00
Spectrum 2	35.25	12.29	6.43	46.03	100.00	Spectrum 2	18.89	9.93	71.18	100.00

A1000-3

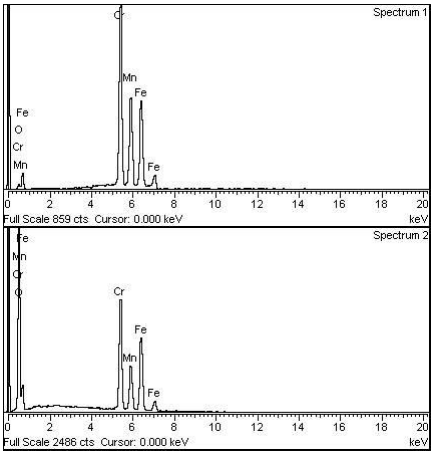

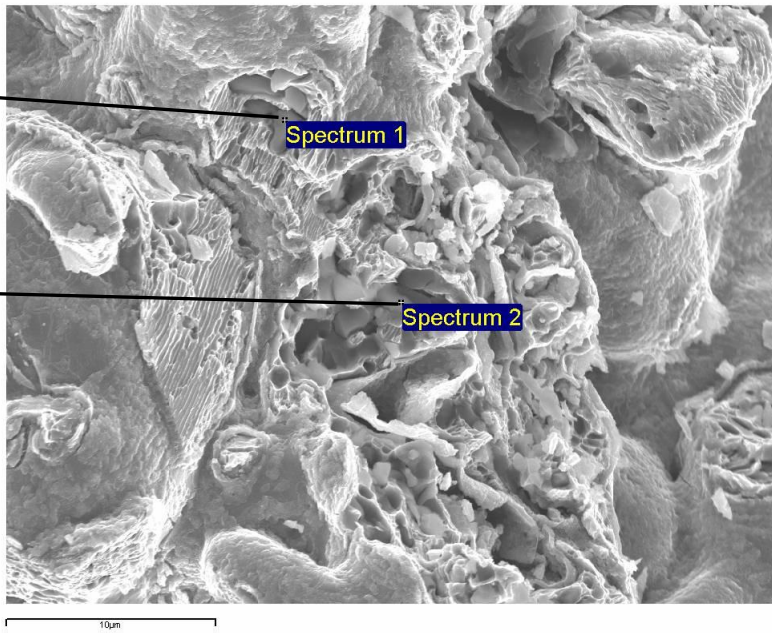

With Oxygen						Without Oxygen				
Spectrum	O	Cr	Mn	Fe	Total	Spectrum	Cr	Mn	Fe	Total
Spectrum 1	2.15	44.02	21.59	32.24	100.00	Spectrum 1	44.98	22.06	32.96	100.00
Spectrum 2	47.23	21.66	8.53	22.59	100.00	Spectrum 2	40.85	16.11	43.04	100.00

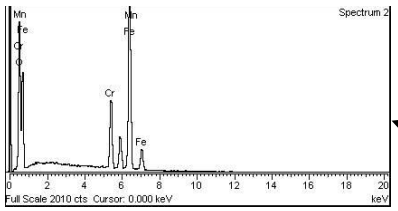

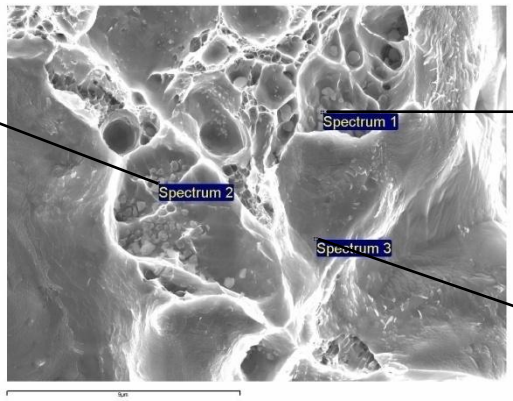

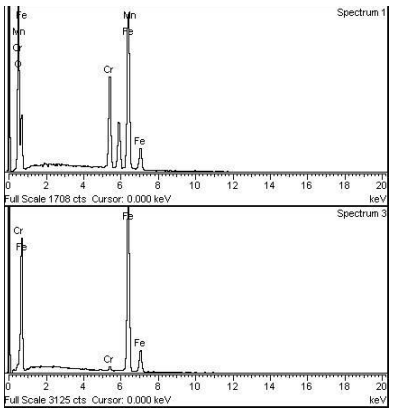

With Oxygen						Without Oxygen				
Spectrum	O	Cr	Mn	Fe	Total	Spectrum	Cr	Mn	Fe	Total
Spectrum 1	38.31	14.44	8.12	39.12	100.00	Spectrum 1	23.30	13.15	63.54	100.00
Spectrum 2	37.87	11.53	5.82	44.77	100.00	Spectrum 2	18.47	9.37	72.17	100.00
Spectrum 3		1.45		98.55	100.00	Spectrum 3	1.45		98.55	100.00

A1120-3

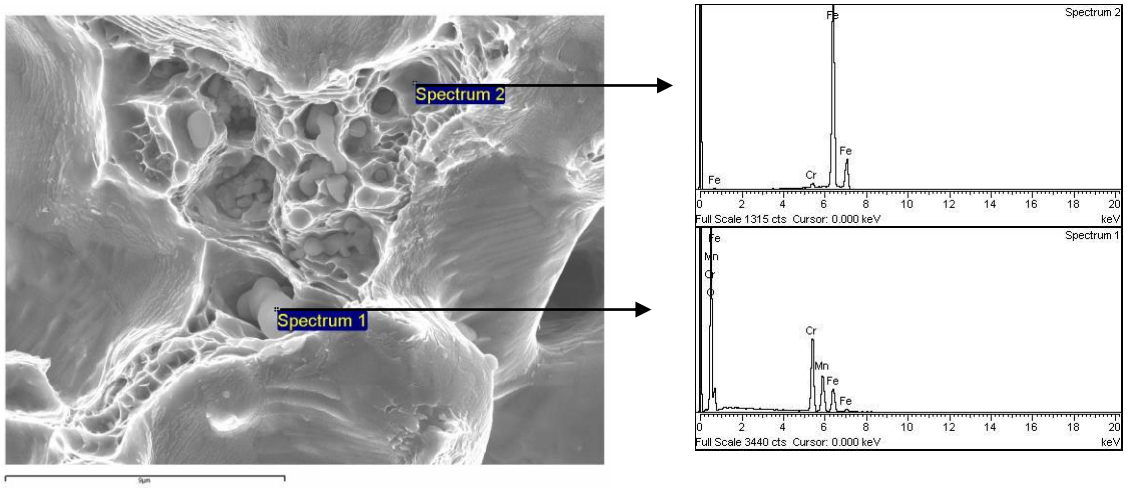

With Oxygen						Without oxygen				
Spectrum	O	Cr	Mn	Fe	Total	Spectrum	Cr	Mn	Fe	Total
Spectrum 1	31.55	33.57	17.65	17.23	100.0	Spectrum 1	48.80	25.66	25.54	100.00
Spectrum 2	0.00	1.12	0.00	98.88	100.0	Spectrum 2	1.11	0.00	98.89	100.00

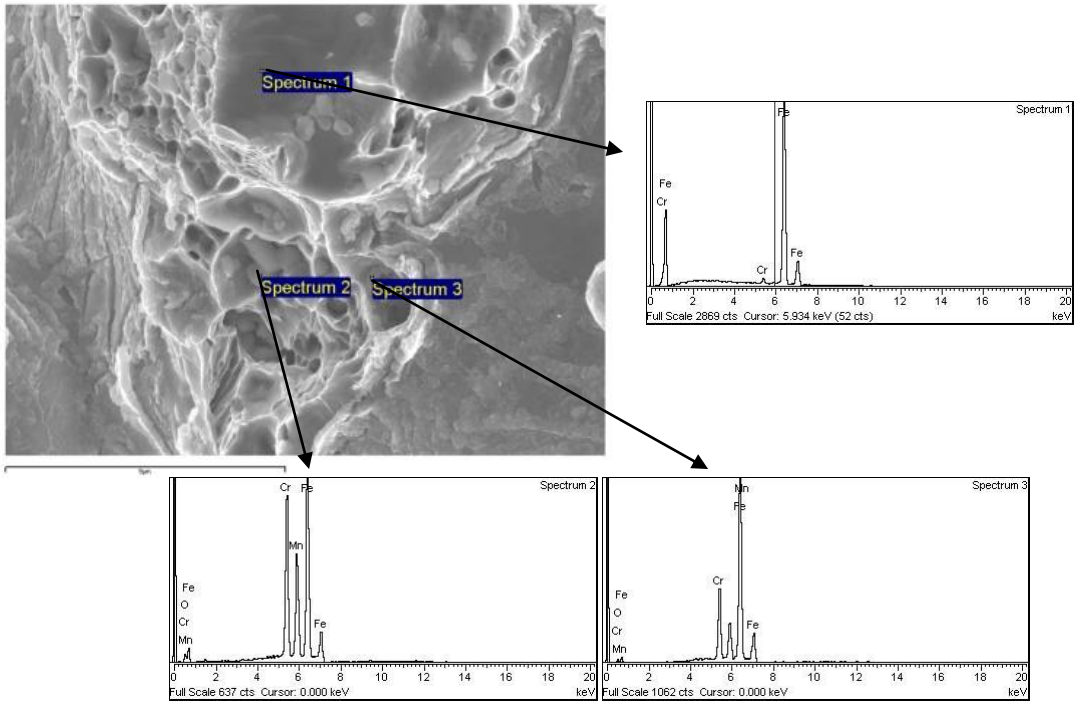

With Oxygen						Without Oxygen				
Spectrum	O	Cr	Mn	Fe	Total	Spectrum	Cr	Mn	Fe	Total
Spectrum 1	1.01	1.40	0.00	97.59	100.00	Spectrum 1	1.42	0.00	98.58	100.00
Spectrum 2	0.70	27.64	19.04	52.63	100.00	Spectrum 2	27.80	19.18	53.02	100.00
Spectrum 3	0.41	15.92	10.09	73.58	100.00	Spectrum 3	16.00	10.12	73.89	100.00

A1120-15

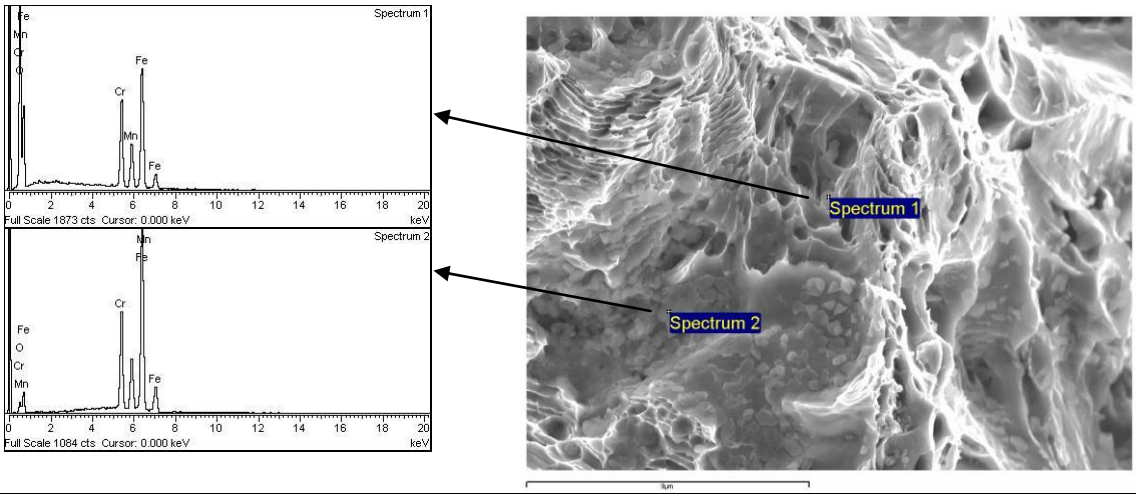

With Oxygen						Without oxygen				
Spectrum	O	Cr	Mn	Fe	Total	Spectrum	Cr	Mn	Fe	Total
Spectrum 1	19.28	20.41	11.94	48.38	100.00	Spectrum 1	25.17	14.74	60.09	100.00
Spectrum 2	1.01	20.28	12.98	65.73	100.00	Spectrum 2	20.48	13.11	66.41	100.00

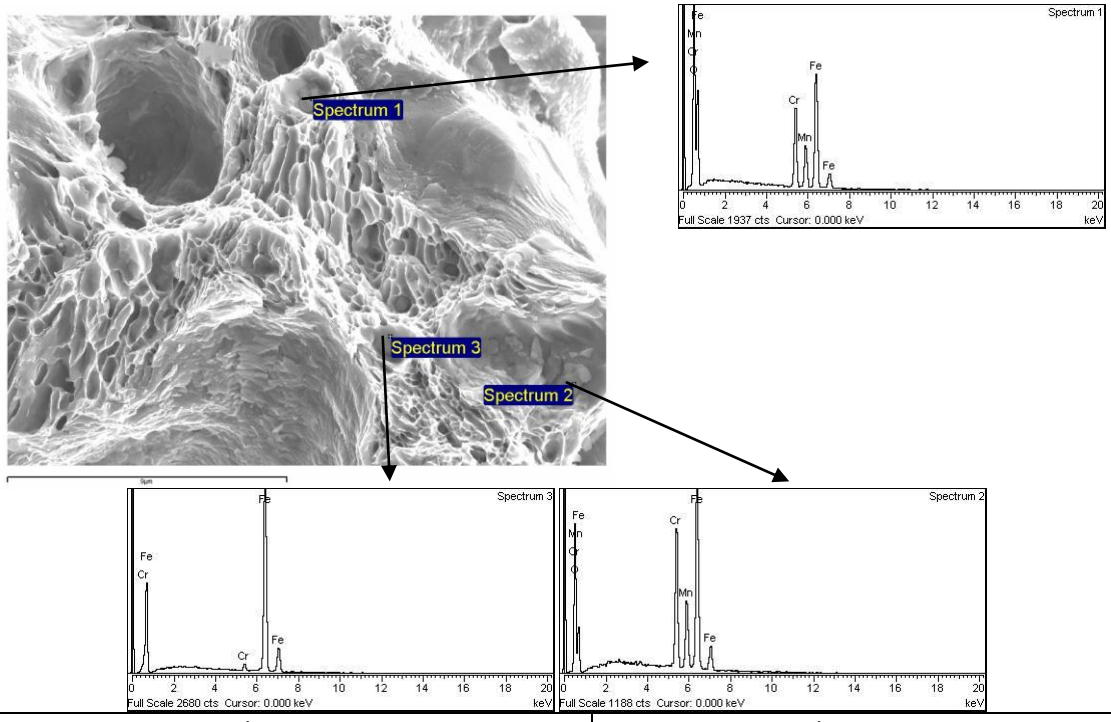

With Oxygen						Without oxygen				
Spectrum	O	Cr	Mn	Fe	Total	Spectrum	Cr	Mn	Fe	Total
Spectrum 1	19.70	19.22	12.26	48.83	100.00	Spectrum 1	23.82	15.22	60.96	100.00
Spectrum 2	11.85	23.03	13.12	52.01	100.00	Spectrum 2	26.07	14.84	59.09	100.00
Spectrum 3	0.78	1.80	0.00	97.42	100.00	Spectrum 3	1.82	0.00	98.18	100.00

A1120-30

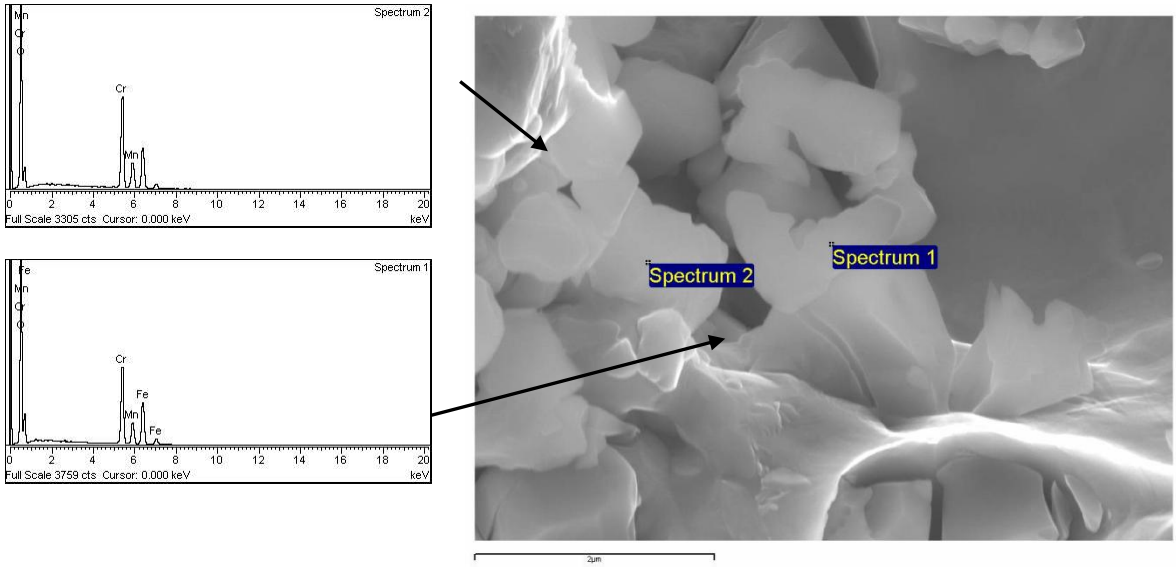

With Oxygen						Without oxygen				
Spectrum	O	Cr	Mn	Fe	Total	Spectrum	Cr	Mn	Fe	Total
Spectrum 1	30.01	32.10	7.88	30.01	100.00	Spectrum 1	45.52	11.20	43.28	100.00
Spectrum 2	28.22	36.38	8.92	26.48	100.00	Spectrum 2	50.36	12.36	37.28	100.00

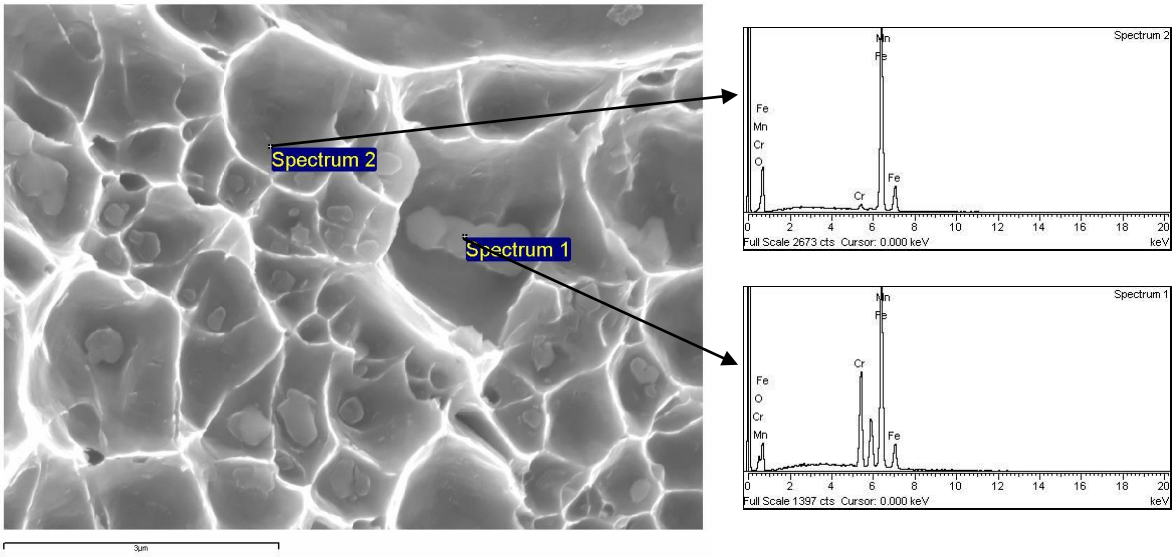

With oxygen						Without oxygen				
Spectrum	O	Cr	Mn	Fe	Total	Spectrum	Cr	Mn	Fe	Total
Spectrum 1	1.80	19.78	12.06	66.35	100.00	Spectrum 1	20.13	12.28	67.59	100.00
Spectrum 2	0.93	1.45	0.00	97.62	100.00	Spectrum 2	1.46	0.00	98.54	100.00